

Modelling the Phototransduction Cascade in different light regimes: From Single Photon Responses to Light Adaptation

Von der Fakultät für Mathematik und Naturwissenschaften der Carl von Ossietzky
Universität Oldenburg zur Erlangung des Grades und Titels einer

Doktorin der Naturwissenschaften (Dr. rer. nat.)

angenommene Dissertation

von Frau Charlotte Johanna Beelen, M. Sc.

geboren am 20.04.1993 in Oldenburg.

Gutachter: **Prof. Dr. Karl-Wilhelm Koch**
Carl von Ossietzky Universität Oldenburg

Weitere Gutachter: **Prof. Dr. Michael Winklhofer**
Carl von Ossietzky Universität Oldenburg

Tag der Disputation: 16.11.2020

Danksagungen

Ich möchte mich gerne bei allen Menschen bedanken, die mich während meiner Promotion unterstützt und begleitet haben.

Zunächst gilt mein Dank meinem Betreuer Karl-Wilhelm Koch - vielen Dank für die Aufnahme in deine Arbeitsgruppe und die Diskussionen, die mein biochemisches Wissen ungemein bereichert haben.

A big thank you also goes to Daniele Dell’Orco - mille grazie - for agreeing to supervise my PhD and for hosting my research stay in Verona. Thank you for introducing me to phototransduction modelling and laying the foundation for all the work presented here, and all the productive ideas and discussions.

Thank you to my collaborators Sabrina Asteriti and Lorenzo Cangiano in Pisa for the fantastic electrophysiological recordings. I am grateful that you made the time to explain the setup and measurements to me, and gave me a lunch break city tour of Pisa.

Danke außerdem an Michael Winklhofer für die Übernahme des Zweitgutachtens.

Furthermore I would like to thank my dear colleagues: everyone, but especially Seher, Lena, Nicole, Sarah, Katharina, Chad, Manisha, Dana, and Hanna, of the AG Biochemie in Oldenburg. Also Giuditta, Anna, Valerio, Davide, Matteo, and Rosario of the Biochemistry and Molecular Biophysics Group in Verona, as well as Alda from Verona. And all my colleagues in the (theoretical) Physics department in Oldenburg, most notably Pascal, Timo, Hauke, Christoph N., Hendrik, Marcel, Sebastian, Christoph K., Mattes, Stefan, Sören, Connie, Christine and Age. I have tremendously enjoyed spending time with you and discussing work and life over breakfasts, lunches and coffee breaks.

Ich war sehr glücklich, meine Promotion innerhalb des Graduiertenkollegs ”Molecular Basis of Sensory Biology” der DFG durchführen zu können. Der DFG möchte ich für die Förderung danken. Außerdem bedanke ich mich bei den Koordinatorinnen des Graduiertenkollegs, Petra und Kristin, für die fantastische Organisation und Unterstützung.

Für die Förderung zu Studienzeiten möchte ich der Studienstiftung des Deutschen Volkes danken. Außerdem danke ich dem DAAD für die finanzielle Förderung während meines Forschungsaufenthaltes in Verona.

Danke auch an alle aktuellen und ehemaligen Mitarbeiterinnen im Team der Gleichstellung in der Physik - Janet, Evelyn, Doro, Margret, Steffi, Daniela, Mareike, Sarah, Noa, Xuscha und Chris. Es war mir eine Ehre, mit euch zusammen für mehr Gleichberechtigung und Sichtbarkeit im Institut zu kämpfen. Danke für euer Engagement und die gute Zusammenarbeit.

Ich möchte allen meinen Freund*innen danken, für eure Unterstützung und dass ihr mich während aller Höhen und Tiefen der Promotion begleitet und zum Lachen gebracht haben. Danke an meine Studienfreund*innen Benedikt, Daniela, Malte und Linda für tiefgreifende Gespräche und lustige Spieleabende. Besonders Benedikt danke ich für dein immer offenes Ohr für meine Sorgen und für Diskussionen über alle erdenklichen Themen von Antirassismus bis Zerstörung des Patriarchats. Danke an die Pfadfinder*innen Lena, Sören, Gesa, Paige, Tine, Philipp, Thorsten, Thomas, Moritz, und Janna für viele lustige Gruppenstunden und Lager. Danke an Alexander in Münster für viele Skypegespräche und deine Geduld mit meiner Verplantheit. Danke an Jantje in Osnabrück für deine stets ermutigenden Worte und den selbstgenähten Pullover. Danke an Anka für leckere Kekse und gemeinsame Kaffeepausen. Danke an Gesa für die tolle Zeit in Italien und Deutschland mit viel leckerem Eis. Danke an Janet für gemeinsame Mensa-Essen, für's Zuhören und Ratschläge geben.

Ein ganz großer Dank gilt meiner Familie. Danke für die emotionale, logistische und finanzielle Unterstützung während meines gesamten Studiums und während der Promotion. Insbesondere bedanke ich mich für euren Rückhalt in schwierigen Zeiten und in der Endphase des Schreibens. Danke an Mama für leckeres Essen und witzige Katzenbilder, danke an Papa für leckere Getränke und witzige Gartenprojekte, und danke an Emma und Ruben für unvergessliche Besuche in Berlin.

Schließlich bedanke ich mich bei meinem Mann Jannik. Danke für deine Ermutigung und Unterstützung und dein lösungsorientiertes Denken. Und danke, dass du tapfer ertragen hast, wenn die Antwort auf die Frage "Wann kommst du heute nach Hause?" mal wieder "Nach der Uni." war.

Zusammenfassung

In den Photorezeptorzellen in der Netzhaut, den Zapfen und Stäbchen, findet der erste Schritt im Sehprozess statt. Eine biochemische Signalkaskade detektiert und verstärkt das Lichtsignal. Das Signal wird daraufhin durch Neuronen in der Netzhaut und im optischen Nerv an das Gehirn weitergeleitet.

Die biochemische Signalkaskade nennt sich *Phototransduktionskaskade*. Da die ihr zugrunde liegenden Wechselwirkungen gut untersucht sind, eignet sie sich besonders gut für mathematische Modellierung. Ich habe, aufbauend auf Modellen der Phototransduktionskaskade in Amphibien und Mäusen, aktualisierte Modelle entwickelt und diese zur Simulation von Lichtantworten unter verschiedenen Bedingungen verwendet.

In dieser Arbeit gebe ich zunächst eine Einführung in das Thema. Dann erläutere ich die methodischen Grundlagen der Modellierung und präsentiere schließlich die Ergebnisse der Modellentwicklung und der Simulationen, aufgeteilt in deterministische und stochastische Modellierung.

Um sicherzustellen, dass das aktualisierte Model Lichtantworten richtig wiedergibt, habe ich die Antworten unter verschiedenen Lichtbedingungen überprüft und die Vorhersagen des Modells mit neuen elektrophysiologischen Messungen verglichen. Außerdem habe ich Lichtantworten unter verschiedenen Bedingungen untersucht. Zum Beispiel konnte ich zeigen, dass ein Feedback-Mechanismus von Kalzium via Recoverin und der Rhodopsinkinase essentiell für die Adaption an einen konstanten Lichthintergrund ist.

Ich habe des Weiteren Lichtantworten in verschiedenen Modellen simuliert, die den Effekt von zwei Krankheiten nachbilden, die die Phototransduktionskaskade betreffen: Retinitis Pigmentosa und Kongenitale Stationäre Nachtblindheit.

Außerdem habe ich eine Hypothese überprüft, nach der ein zusätzlicher Feedback-Mechanismus von Kalzium auf den Effektor der Kaskade notwendig sei, zum Beispiel durch Recoverin oder die Rhodopsinkinase. Meine Untersuchung zeigt, dass der zusätzliche Mechanismus im Modell nicht notwendig ist, um die experimentellen Beobachtungen zu reproduzieren.

Stäbchen haben reproduzierbare Lichtantworten auf einzelne Photonen, und arbeiten damit an der Grenze des physikalisch Messbaren. Antworten auf einzelne

Photonen wurden seit ihrer Entdeckung mit viel Interesse untersucht.

Um Antworten auf einzelne Photonen und ihre Eigenschaften zu untersuchen, habe ich stochastische Modelle der Phototransduktionskaskade entwickelt. Ich habe ein neues reduziertes stochastisches Modell erstellt, welches neue Ergebnisse bezüglich des Effektors berücksichtigt.

Indem ich Antworten auf einzelne Photonen in modifizierten Modellen simuliert habe, konnte ich die Relevanz der Phosphorylierungen von Rhodopsin sowie die Auswirkungen von genetischen Knockouts untersuchen.

Außerdem habe ich die Ergebnisse des Modells mit neuen elektrophysiologischen Messungen verglichen, nachdem ich die Messergebnisse in Antworten auf einzelne und mehrere Photonen sowie nicht absorbierte Photonen aufgeteilt habe. Ich konnte zeigen, dass diese Aufteilung zu einer Unterschätzung der Variabilität der Antworten auf einzelne Photonen führt, indem ich Simulationen mit zufälligen Anfangsbedingungen durchgeführt habe.

Schließlich habe ich die Auswirkungen einer dynamischen Bindung von Rhodopsin und Transduzin im Dunkeln untersucht und festgestellt, dass dieser Effekt zu einer reduzierten Variabilität der Antworten auf einzelne Photonen führen kann.

Abstract

The first step in vision takes place in the photoreceptor cells in the retina, the rods and cones. Within the photoreceptor cells, a biochemical signalling cascade detects and amplifies the light signal, which is then transferred to the brain via neurons in the retina and the optic nerve.

This biochemical signalling cascade is called the *phototransduction cascade*. The interactions that constitute the phototransduction cascade in rods are extremely well-studied, which makes the system suited for computational modelling. Building on the modelling of phototransduction in amphibians and mice, I updated the models to new insights on the phototransduction cascade and used them to simulate light responses in different conditions.

In this thesis, I first give an introduction into the topic. I subsequently explain the methodological basis of the modelling and finally present the results of the model development and the simulations, separated into deterministic and stochastic modelling.

To make sure that the updated model reproduces light responses correctly, I verified responses in different light conditions and compared the model's predictions to novel electrophysiological recordings.

I further studied light responses in different conditions. For example, I showed the relevance of the calcium feedback mechanism via recoverin and the rhodopsin kinase for light adaptation.

I also simulated light responses in models approximating the effect of mutations that cause retinitis pigmentosa or congenital stationary night blindness, two related phototransduction diseases.

Furthermore, I examined a hypothesis about a potential missing mechanism in the cascade: an additional calcium feedback, possibly via recoverin or the rhodopsin kinase, on the effector. My investigation showed that this mechanism is not required to explain the experimental results.

Rod cells exhibit reproducible responses to stimuli consisting of single photons, and thus operate at the physical measurement limit. Single photon responses in rods have been the subject of intense study for a few decades since their discovery. In order to investigate single photon responses and their different characteristics,

I developed stochastic models of the phototransduction cascade. I created a new reduced stochastic model, which includes novel insights on the effector.

I examined light responses in different modified models to study the significance of multiple phosphorylation sites of rhodopsin, as well as single photon responses in different genetic knockout conditions.

Furthermore, I compared the model's results to novel experimental dim flash recordings, after having categorized them into single photon responses, multiple photon responses and failures. I showed that this categorization may lead to an underestimation of the variability of single photon responses by performing simulations with random initial conditions.

I further investigated the role of a dynamic preassembly of rhodopsin and transducin in the dark and found that it may decrease the variability of single photon responses.

Abbreviations

ADP	Adenosine diphosphate
Arr	Arrestin
ATP	Adenosine triphosphate
Ca ²⁺	Calcium ion
cGMP	Cyclic guanosine monophosphate
CNGC	Cyclic nucleotide gated channel
CSM	Completely substituted mutant of rhodopsin (no phosphorylation sites)
CSNB	Congenital stationary night blindness
CV	Coefficient of variation
E	Effector of the phototransduction cascade (activated PDE)
EF hand	Calcium binding site consisting of α -helices E and F
G _{α}	α -subunit of the G-protein
G _{$\beta\gamma$}	β - and γ -subunits of the G-protein
GC	Guanylyl cyclase
GCAP	Guanylyl cyclase activating protein
GDP	Guanosine diphosphate
GMP	Guanosine monophosphate
GPCR	G-protein coupled receptor
Gt	G-protein / transducin
GTP	Guanosine triphosphate
MPR	Multiple photon response
Ops	Opsin
PDE	Phosphodiesterase 6
R	Rhodopsin
Rec	Recoverin
RGS	Regulator of G-protein signalling
RK	Rhodopsin kinase
RP	Retinitis pigmentosa
SPR	Single photon response
WT	Wild type
ΔJ	Photocurrent
ΔU	Photovoltage

Table of Contents

1	Introduction	1
1.1	The phototransduction cascade	2
1.1.1	The retina	2
1.1.2	The activation of the cascade	5
1.1.3	The shut-off of rhodopsin	7
1.1.4	The recovery of the dark state	8
1.1.5	Supramolecular organization and the dynamic scaffolding mechanism	9
1.1.6	The single photon response	10
1.2	Modelling phototransduction	12
2	Methods	15
2.1	Modelling framework	15
2.1.1	Biochemical reaction networks	16
2.1.2	Reaction rate constants and affinities	20
2.1.3	Steady state and dynamics	21
2.2	Simulations	21
2.2.1	Euler method	22
2.2.2	4 th order Runge-Kutta	23
2.2.3	Generalized and implicit Runge-Kutta	24
2.2.4	The Gillespie algorithm	25
2.3	Basis of the modelling	28
2.3.1	The Dell’Orco 2009 model	28
2.3.2	The Invergo 2014 model	35
2.4	Implementation in IQMtools	37
3	Deterministic modelling	41

TABLE OF CONTENTS

3.1	Rhodopsin-effector coupling	41
3.1.1	Fewer activated effector molecules	42
3.1.2	Dimeric activation of the effector	48
3.2	Light adaptation	51
3.3	Comparison to novel electrophysiological data	56
3.4	Calcium feedback on the effector	61
3.5	Disease modelling	65
4	Stochastic modelling	75
4.1	Stochastic amphibian model	75
4.1.1	Multiple phosphorylation sites	79
4.2	Stochastic mouse model	82
4.2.1	Multiple phosphorylation sites	84
4.2.2	Different knockout models	85
4.3	Small stochastic model	88
4.3.1	Single photon responses in the new model	93
4.3.2	Different knockout models	95
4.4	Comparison to novel electrophysiological data	96
4.4.1	Categorization of the dim flash responses	96
4.4.2	Conversion of photovoltage to photocurrent	101
4.4.3	Results and comparison to simulations	102
4.5	Precoupling	106
4.6	Random initial conditions	112
5	Discussion	119
5.1	Deterministic modelling	120
5.1.1	Bright light stimuli: Comparison to experiment	120
5.1.2	Light adaptation	121
5.1.3	Hypothesized calcium feedback on the effector	122
5.1.4	Disease modelling	123
5.2	Stochastic modelling with the old mouse and amphibian model . . .	124
5.2.1	The role of the phosphorylation sites	125

TABLE OF CONTENTS

5.3	Update of the models and creation of the small model	126
5.4	Results in the small stochastic model	128
5.4.1	Comparison to electrophysiologically recorded single photon responses	128
5.4.2	Knockout models	131
5.4.3	Precoupling	132
5.5	Conclusion	133
Appendix A Models		135
A.1	Stochastic amphibian model	135
A.2	Stochastic mouse model	138
A.3	Updated deterministic mouse model	142
A.4	Small stochastic model	142
Bibliography		147

TABLE OF CONTENTS

List of Figures

1.1	The location of the retina in the eye and its structure, from (Dreamstime)	2
1.2	Cell types in the retina, from (Cepko, 2014).	3
1.3	The phototransduction cascade in rods, from (Chen and Sampath, 2013)	5
1.4	The dynamic scaffolding mechanism, from (Koch and Dell’Orco, 2015)	10
2.1	An example of a chemical reaction network	17
2.2	An example of a small reaction network	20
2.3	Schematic of the Gillespie algorithm	26
2.4	Reaction network schematic of the Dell’Orco 2009 model, from (Dell’Orco et al., 2009)	29
3.1	Reaction network of the activation of the G-protein	43
3.2	The IQMparamestGUI manual tuning interface	44
3.3	The single photon response in the Invergo 2014 model and the new deterministic model.	45
3.4	Responses to flashes of increasing brightness in the Invergo 2014 model and the new deterministic model.	46
3.5	Responses to different light stimuli for WT and GCAPs -/- in the Invergo 2014 model and the new deterministic model.	47
3.6	Single- and double-activated PDE during the single photon response	49
3.7	Light adaptation after a background and saturating flash	51

LIST OF FIGURES

3.8	Network for the calcium-dependent regulation of rhodopsin kinase by recoverin	52
3.9	Network for the calcium-independent regulation of rhodopsin kinase by recoverin	53
3.10	Response to flashes with no background for the normal model and the model without calcium feedback	54
3.11	Missing light adaptation after a background and saturating flash in the model without calcium feedback	54
3.12	Time spent in saturation after different backgrounds and a saturating flash for the normal model and the model without calcium feedback	55
3.13	Electrophysiological recording of the response to a combination of a background stimulus and a series of five flashes	57
3.14	Experimental and simulated responses to the bright light stimulus paradigm	59
3.15	Reduction in T_{half} for the experimental and simulated data	60
3.16	Experimental responses to flashes for the wild type, overexpression of rhodopsin kinase, and recoverin knockout, from (Chen et al., 2012)	61
3.17	Simulated responses to flashes for the wild type, overexpression of rhodopsin kinase, and recoverin knockout.	63
3.18	Pepperberg plot for the wild type, overexpression of rhodopsin kinase, and recoverin knockout.	64
3.19	Photocurrent for the retinitis pigmentosa mutant models	69
3.20	Effector for the retinitis pigmentosa mutant models	71
3.21	Calcium level for the retinitis pigmentosa mutant models	72
4.1	Stochastic frontend and backend of the amphibian model	77
4.2	Stochastic and deterministic traces for the effector and ΔJ in the stochastic amphibian model	79

4.3	Single photon responses with different numbers of available phosphorylation sites in the amphibian model	81
4.4	Stochastic and deterministic traces for the effector and ΔJ in the stochastic mouse model	83
4.5	Single photon responses with different numbers of available phosphorylation sites in the mouse model	84
4.6	Single photon responses with different knockouts in the mouse model	86
4.7	Rhodopsin in the different phosphorylation states during the single photon response	89
4.8	Reaction networks for the new, small stochastic model	92
4.9	Single photon responses in the new small model.	93
4.10	Single- and double-activated PDE during single photon responses in the new small model	94
4.11	Single photon responses with different knockouts in the small model	95
4.12	Examples of the electrophysiologically recorded dim light responses	96
4.13	Examples of dim flash responses and their mean	97
4.14	Mean response scaled to three individual responses	98
4.15	Histogram of the scaling factors	99
4.16	Histogram of the scaling factors with fitted sum of Gaussians	100
4.17	Categorized failures, single and multiple photon responses	103
4.18	Average single photon responses from electrophysiological recordings and stochastic simulations	104
4.19	Scaled species numbers for the steps towards activated PDE	105
4.20	Deterministic simulation of the single photon response with and without precoupling	107
4.21	Deterministic simulation of $G_{\alpha GTP}$ during the single photon response with and without precoupling	108

LIST OF FIGURES

4.22	Deterministic simulation of $R_0 \cdot Gt$ during the single photon response with and without precoupling	109
4.23	Stochastic simulation of the single photon response with and without precoupling	110
4.24	Histograms of the SPR amplitude and area: precoupled and non-precoupled	111
4.25	The Poisson distribution $P_\lambda(k)$ for $\lambda = 1, 2$ and 4	113
4.26	True single and multiple photon responses resulting from a simulation with random initial conditions	115
4.27	Categorized failures, single and multiple photon responses resulting from a simulation with random initial conditions	116
4.28	Miscategorized single and multiple photon responses resulting from a simulation with random initial conditions	117

List of Tables

3.1	A list of all manually tuned parameters in the activation of the G-protein by rhodopsin.	43
3.2	Categories for rhodopsin mutations causing RP or CSNB.	66
3.3	Mutant models representing kinetic changes for RP or CSNB. . . .	68
A.1	Reaction equations in the stochastic amphibian frontend model. . .	135
A.2	Reaction equations in the stochastic amphibian backend model. . .	136
A.3	Parameters in the stochastic amphibian frontend model.	136
A.4	Parameters and variables in the stochastic amphibian backend model.	137
A.5	Nonzero initial conditions in the stochastic amphibian frontend model.	138
A.6	Nonzero initial conditions in the stochastic amphibian backend model.	138
A.7	Reaction equations in the stochastic mouse frontend model.	138
A.8	Reaction equations in the stochastic mouse backend model.	139
A.9	Parameters in the stochastic mouse frontend model.	140
A.10	Parameters and variables in the stochastic mouse backend model. .	141
A.11	Nonzero initial conditions in the stochastic mouse frontend model. .	141
A.12	Nonzero initial conditions in the stochastic mouse backend model. .	141
A.13	Parameter changes in the updated deterministic mouse model. . . .	142
A.14	Reaction equations in the small stochastic frontend model.	143
A.15	Parameters in the small stochastic frontend model.	144
A.16	Nonzero initial conditions in the small stochastic frontend model. .	145

LIST OF TABLES

1 | Introduction

This thesis is about the first step in vision: the phototransduction cascade. It is an extremely well-studied signalling cascade and a model for G-protein coupled receptor cascades. A specific feature of the phototransduction cascade in rods is the single photon response. These quantal responses are surprisingly reproducible and have been the subject of intense scientific scrutiny for a long time.

In this thesis, I aim to create a model of the phototransduction cascade that is able to reproduce its dynamic behaviour in different light regimes. Specifically, I am interested in light adaptation behaviour and the reproducibility of the single photon response. Furthermore, I use the model to investigate light responses in rods with genetic alterations to reproduce the experimental results from knock-out animals, and to predict the effect of diseases such as retinitis pigmentosa on light responses and the equilibrium in the dark state.

In this chapter, the phototransduction cascade is explained as well as the further signal transduction toward the brain. Furthermore, previous modelling approaches are summarized.

In the Methods chapter [2](#), I explain the necessary mathematical and computational background as well as the details of the two models that form the basis for the model development carried out in this thesis.

The new modelling approaches and their results are shown in chapters [3](#) and [4](#). Chapter [3](#) focusses on deterministic modelling: the model is modified to better reflect new experimental results and the effect of light adaptation is investigated. The results of the model are compared to novel electrophysiological results on light adaptation. Furthermore, the effect of congenital stationary night blindness and retinitis pigmentosa on phototransduction is studied.

Chapter [4](#) shows the new stochastic modelling approach and the results for the modelling of dim flash responses. Stochastic versions of the models investigated earlier are developed and different factors influencing the reproducibility of their single photon responses are investigated. A new stochastic model is created, which reproduces novel experimental results concerning the amount of activated effector molecules and their dimeric nature. This model is then used to simulate single

photon responses in different conditions.

Finally, in chapter 5, the results and their significance for phototransduction research are discussed.

1.1 The phototransduction cascade

Vision is one of the most important senses informing us about our environment. In this thesis, I focus on the biochemical signal transduction cascade called *phototransduction*, which takes place in light sensitive cells in the eye and converts the light stimulus into an electrical signal. This section focuses on the biological and chemical background of the phototransduction cascade and its role in the visual system.

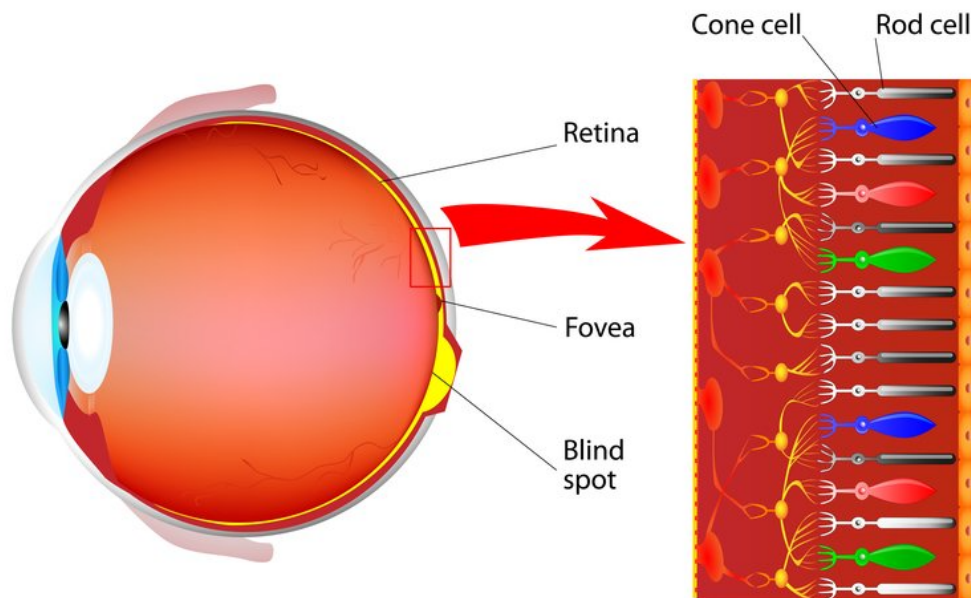


Figure 1.1: The location of the retina in the eye and its structure. Copyright ©2000-2020 Designua, from (Dreamstime).

1.1.1 The retina

The first step in vision takes place in the retina at the back of the eye, which can be seen in figure 1.1. The light first passes through the pupil, which regulates the amount of light to enter the eye, and through the lens, which focuses the light. It then goes through the vitreous body and finally reaches the retina. The retina is built up of different layers of neurons, with the photosensitive cells - the rods and cones - in the very back of the retina.

1.1. THE PHOTOTRANSDUCTION CASCADE

After the photosensitive cells have received a light signal, they transmit it to other neurons of the retina, which process the signal and finally transmit it to the brain via the optic nerve.

Of the two types of photosensitive cells, *cones* mediate vision in bright light conditions and color vision. Humans have three types of cones with different regimes of sensitivity - for red, green, and blue light. Other animals have cones that cover different wavelengths of light, for example the UV spectrum.

The other type of photosensitive cells, the *rods*, mediate vision in dim light conditions. We only have one type of rods, which is why we cannot distinguish colors in dim light. Rods are exceedingly good at processing dim light stimuli: they show a reproducible response to single photons and thus operate up to the physical measurement limit. The phototransduction cascade in rods is well-studied and is thus well suited to modelling approaches. It is explained in more detail in the next section.

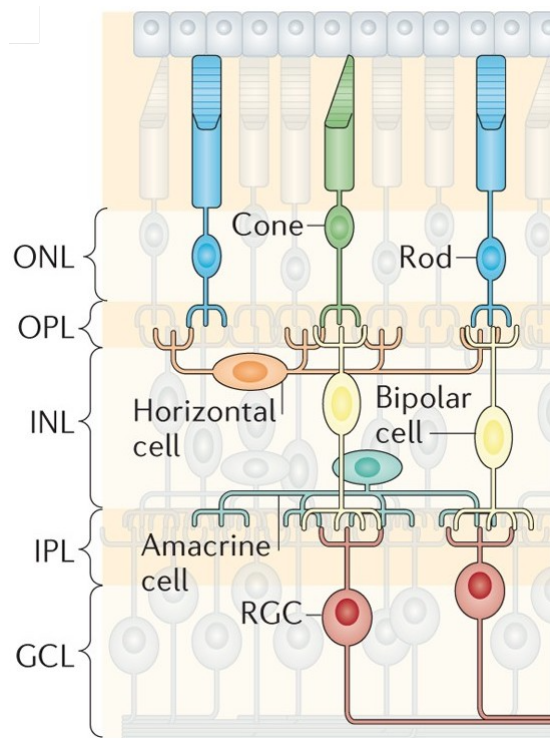


Figure 1.2: Cell types in the retina. Reprinted by permission from Springer Nature, from (Cepko, 2014).

Rods and cones in the retina form a mosaic: they are intermingled with one another to enable us to see all colours throughout our field of vision. However, they are not completely equally distributed: in the *fovea*, which is where the incoming

CHAPTER 1. INTRODUCTION

light from directly ahead is focused, there are only cones. These cones are especially slim to allow for an exceptionally high resolution, and they become bigger towards the edges of the retina, where less light ends up. Due to the fact that only cones are located in the fovea, this becomes a blind spot in dim light conditions, which can be noticed when looking at stars in a dark night.

After the rods and cones have translated the light stimulus into a neurotransmitter signal, this signal is picked up by downstream neurons within the retina. These neurons are the first step in processing the raw stimulus before the signal even arrives at the brain. In figure 1.2, an overview of the different cell types can be seen.

The retinal neurons are bipolar cells, horizontal cells, amacrine cells, and retinal ganglion cells. Their joint task is the compression and combination of the signals of all separate rods and cones - they encode e.g. motion or contrast (Wässle, 2004). After the signal has been processed by these neurons, it is passed on to the brain through the optic nerve. The spot where the optic nerve originates in the eye contains no photoreceptors and is therefore known as the *blind spot* - it can be found in the visual field when covering one eye and focusing on one point.

In the following, we are focusing on the precise mechanism of vision in the photosensitive cells, specifically the rods. This is the phototransduction cascade: the process that translates a light stimulus into an electrical signal.

In figure 1.3, a cross-section of the rod is shown on the left. The upper part of the rod is called the outer segment. This is where the phototransduction cascade takes place. The disc-shaped objects in the outer segment are the so-called *disc membranes*: they are discs of membrane within the cell. Many of the phototransduction proteins interact with these disc membranes. The different stages of the phototransduction cascade in rods are illustrated on the right in figure 1.3 and described in the following sections. For the basic mechanisms of the phototransduction cascade, please refer to (Pugh Jr and Lamb, 2000).

1.1. THE PHOTOTRANSDUCTION CASCADE

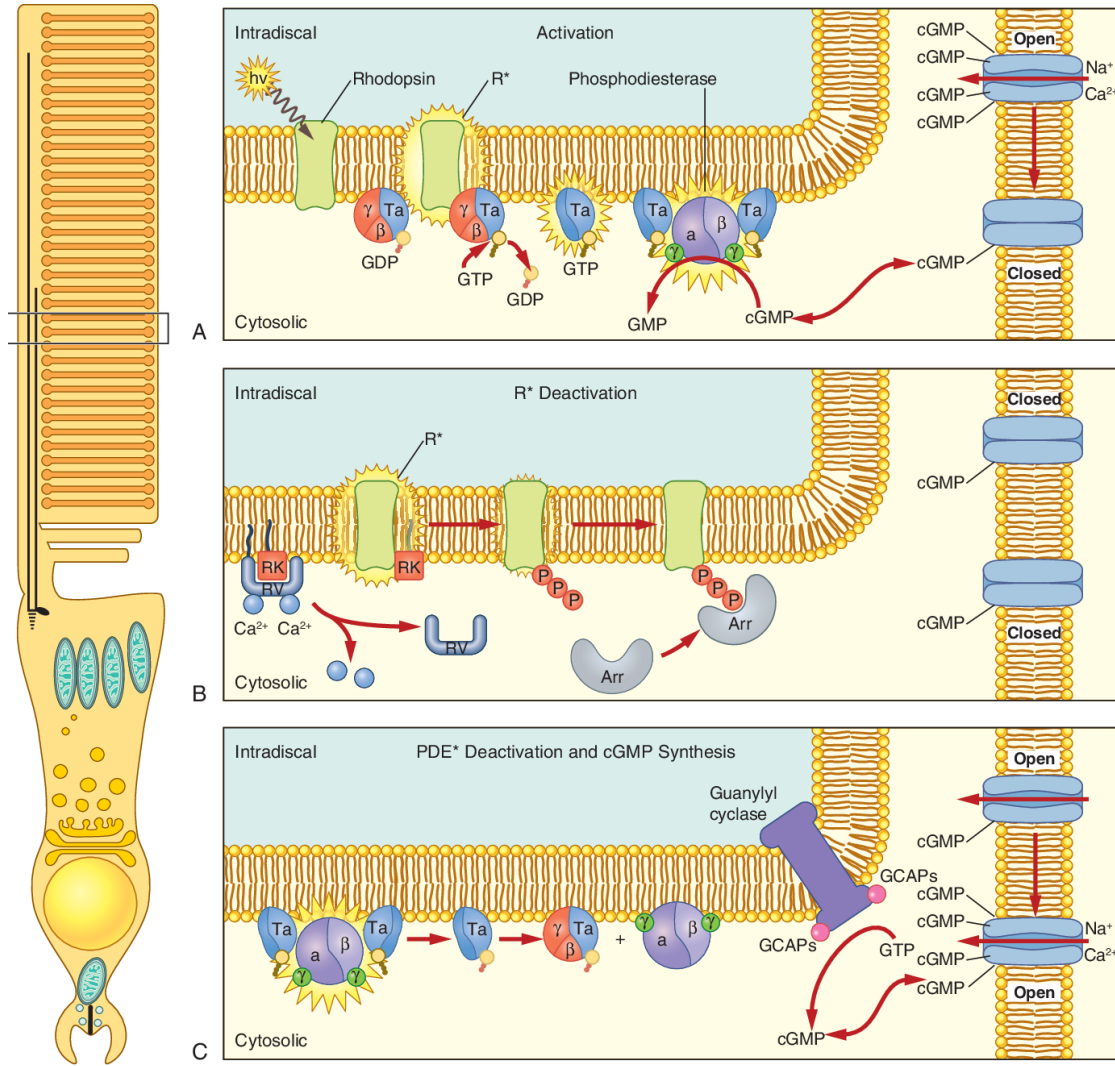


Figure 1.3: The phototransduction cascade in rods. On the left, a cross-section of a rod cell is shown. The phototransduction cascade takes place in the outer segment, which is the upper part of the rod cell containing the disc membranes, shown in a darker color. In the insets on the right, the different stages of the phototransduction cascade are illustrated. Inset A shows the activation, while B illustrates the deactivation of the activated rhodopsin (R*). Inset C shows the recovery of the dark state via PDE* deactivation and cGMP synthesis. Reprinted by permission from Elsevier, from (Chen and Sampath, 2013).

1.1.2 The activation of the cascade

The first step in the phototransduction cascade is the activation of the receptor molecule *rhodopsin*. Rhodopsin belongs to the family of *G-protein coupled receptors* (GPCRs). This type of receptors plays a role in many signal transduction cascades in cells across different species, e.g. in olfaction and taste. After their activation, they transmit the signal using a G-protein. In the case of the photo-

CHAPTER 1. INTRODUCTION

transduction cascade, this is the G-protein *transducin*. We will in the following use the names transducin and G-protein interchangeably for this protein.

In the dark state, rhodopsin is covalently bound to 11-cis-retinal, which keeps it in the inactive state. Upon activation by light, the 11-cis-retinal is transformed to all-trans-retinal, which triggers a conformational change of rhodopsin to metarhodopsin II - the active state.

As can be seen in figure 1.3A, rhodopsin is a transmembrane protein: it is located in the disc membrane and has regions both inside and outside the membrane on both sides. Transducin has a membrane anchor and can diffuse towards rhodopsin along the disc membrane. Rhodopsin in the active state can then activate the transducin. After some intermediate steps, in which the guanosine diphosphate (GDP) bound to the G-protein is exchanged for guanosine triphosphate (GTP), the activated G-protein separates into its α and the β - and γ -subunits. The α -subunit is the active form of the G-protein and transmits the signal further downstream. The α -subunit of the G-protein (G_α) binds to the enzyme phosphodiesterase 6 (PDE), thereby activating it. The PDE has two inhibitory subunits with one binding sites for G_α each. The precise consequences when one or two G_α bind to the inhibitory subunits of PDE are currently a matter of debate (Lamb et al., 2018), (Qureshi et al., 2018). The gain of the activation of the G-protein and the PDE molecules is equally disputed (Yue et al., 2019), (Heck et al., 2019), (Yau et al., 2019). This is further elaborated in section 3.1. The activated PDE is also referred to as the *effector* of the phototransduction cascade.

In the dark state, there is a constant flux of ions through the cell, constituting the *circulating current*. It is carried by sodium ions (90 %) and calcium ions (10 %). The ions flow in through so-called cyclic nucleotide gated channels: channels in the cell membrane that are kept open by a constant concentration of the cyclic nucleotide cGMP (cyclic guanosine monophosphate) in the cell. The channels are schematically shown on the right in figure 1.3A. At the same time, calcium is extruded from the cell by ion exchangers in the cell membrane. When there is no light stimulus, there is an equal influx and efflux of calcium, resulting in a balanced constant calcium concentration. The sodium concentration is also constant due to a balanced influx and efflux.

As soon as the PDE is activated as a consequence of the activation of rhodopsin, it hydrolyzes cGMP, turning it into GMP (guanosine monophosphate). This decreases the overall level of cGMP in the cell. This decrease leads to the closing of the cyclic nucleotide gated channels, as the cGMP dissociates from them.

The closure of the channels interrupts the influx of ions into the cell. Since ions are still leaving the cell, the sodium and calcium ion concentrations decrease. The decrease in calcium concentration has important physiological consequences, as we shall see in the next sections. The overall decrease in ion concentration results in a change of the circulating current in the cell. The membrane hyperpolarizes, which triggers a change in the release of neurotransmitters at the synaptic terminal of the photoreceptor. This signal is then picked up by downstream neurons and transmitted further. Please note that, while the rod is a neuron, it does not spike as an output signal. Instead, it has a continuous, analog output signal. In this dissertation, we quantify the light response of the cell in terms of change of circulating current ΔJ and change in membrane potential ΔU .

1.1.3 The shut-off of rhodopsin

After the phototransduction cascade has been activated by light, it needs to be deactivated. Only this can make the cell capable of sensing new stimuli. In order to shut off the response, first the source of the signal has to be turned off, which is the activated rhodopsin. This is done by three different proteins: recoverin, rhodopsin kinase, and arrestin.

Recoverin is a calcium-binding protein with four EF-hands. It undergoes a conformational change, more precisely a myristoyl switch, upon calcium binding: when calcium ions are bound, a covalently bound myristoyl group is extruded from its binding pocket within the protein. This allows recoverin to anchor to the disc membrane in the rod cell, as shown in figure 1.3B on the left. (Ames et al., 1997) In the dark, recoverin is bound to calcium ions and interacts with the disc membrane and another phototransduction protein: the *rhodopsin kinase* (RK). The rhodopsin kinase is able to phosphorylate activated rhodopsin, but in the dark state, a large fraction of the rhodopsin kinase is kept inactive by the recoverin, since it prevents the interaction between rhodopsin and the rhodopsin kinase.

After the light stimulus, the calcium level decreases due to the closure of cyclic nucleotide gated channels. This in turn triggers recoverin's conformational change, leading to the retraction of the myristoyl group into its pocket within the molecule. Due to this, the recoverin detaches from the disc membrane and releases the rhodopsin kinase (shown in figure 1.3B on the left). The rhodopsin kinase is now free to diffuse along the disc membrane to the activated rhodopsin molecules and phosphorylate them. One rhodopsin molecule can be phosphorylated up to at

least six times. (Chen et al., 1995), (Klenchin et al., 1995)

The phosphorylation of rhodopsin leads to a gradual shut-off. First of all, the affinity for transducin decreases as a function of the number of phosphorylations - therefore phosphorylated rhodopsin is less active. At the same time, the affinity for another phototransduction protein called *arrestin* increases (Gibson et al., 2000). Arrestin can bind to rhodopsin after it has been phosphorylated at least once and it terminates rhodopsin's activity immediately. Thus, both the rhodopsin kinase and arrestin are necessary for a normal shut-off of the cascade: the phosphorylation by the rhodopsin kinase is necessary to enable the binding of arrestin, which is in turn required for a complete shut-off.

After rhodopsin has bound to arrestin, it cannot activate any further G-proteins. The rhodopsin then loses the retinal and is turned into opsin. In a recycling process, the retinal is restored to the rhodopsin, enabling it to be photoactivated again.

1.1.4 The recovery of the dark state

To recover the dark state of the cell, the cell needs to return to its dark levels of cGMP and calcium. The active complex of the active α subunit of the G-protein $G_{\alpha GTP}$ and the PDE is deactivated by the intrinsic GTPase activity of the G_{α} -subunit. GTP is thus turned into GDP and the active complex separates into PDE and $G_{\alpha GDP}$. The rate of the deactivation is higher when the complex binds to a protein called RGS (regulator of G-protein signalling). The $G_{\alpha GDP}$ is no longer active and recombines with its β - and γ -subunits. After this, it can again be activated by rhodopsin. The PDE also returns to its inactive state without the transducin. This step of the deactivation is shown in figure 1.3C on the left.

The cGMP-concentration is restored by the GC-GCAP system, as shown in figure 1.3C on the right. The enzyme GC (guanylate cyclase) is activated by the GCAPs (guanylate cyclase activating proteins) in a calcium-dependant manner (Koch and Stryer, 1988), (Olshevskaya et al., 1997), (Palczewski et al., 1994).

When the calcium concentration is high in the dark, the GC is suppressed. When the calcium level drops as a consequence of illumination, the GCAPs activate the GC and it synthesizes cGMP to restore its concentration. As a consequence of this, the cyclic nucleotide gated channels are re-opened and the calcium concentration is restored as well.

In the dark state, there is a dynamic equilibrium for the cGMP concentration. The PDE has a small spontaneous activity in the dark, which consumes small amounts of cGMP. This is compensated by the basal activity of the GC, which produces a small amount of cGMP without activation by the GCAPs. The consumption and production of cGMP are in equilibrium, leading to a constant, slightly fluctuating concentration.

1.1.5 Supramolecular organization and the dynamic scaffolding mechanism

In recent years, more and more evidence has accumulated which shows that rhodopsin is not homogeneously distributed in the disc membranes. Instead, several studies have shown that rhodopsin appears to organize itself in larger supramolecular complexes: since 2000, several studies using methods such as atomic force microscopy have shown that rhodopsin arranges in ordered rows of dimers (Fotiadis et al., 2003), (Liang et al., 2003), (Fotiadis et al., 2004). In 2015, a study using cryoelectron microscopy showed that rhodopsin is arranged in dimers, which arrange as rows, which then join to form tracks of two pairs of dimer rows (Gunkel et al., 2015).

The results of the studies were a topic of intense discussions, including previous assumptions of heterogeneous rhodopsin distribution. This also led to a controversial debate about the implications of the supramolecular organization on the kinetics of the phototransduction cascade and especially the interaction with - and activation of - the G-protein (Dell’Orco and Schmidt, 2008), (Chabre et al., 2003), (Chabre and le Maire, 2005).

In 2011 Daniele Dell’Orco and Karl-Wilhelm Koch suggested that rhodopsin and transducin could dynamically and rapidly associate and dissociate in the dark in the so-called *dynamic scaffolding mechanism* (Dell’Orco and Koch, 2011), illustrated in figure 1.4.

In this model, the G-proteins rapidly hop from one rhodopsin molecule (red) to the next. As soon as they associate with an activated rhodopsin molecule (yellow), they are in turn activated. A proportion of 10-30% of all G-protein molecules are dynamically associated with rhodopsin at any time, but they are not statically bound to the rhodopsin. Their rapid association and dissociation from the

rhodopsin molecules enables an effective start of the signalling cascade.

This is possible because the dissociation rate of transducin from dark-adapted rhodopsin is about 300-fold faster than from light-activated rhodopsin, enabling the transducin to quickly hop to the next rhodopsin molecule if it meets an inactive rhodopsin (1 in figure 1.4), but to get activated when it meets a light-activated rhodopsin (2 in the figure) (Koch and Dell’Orco, 2015).

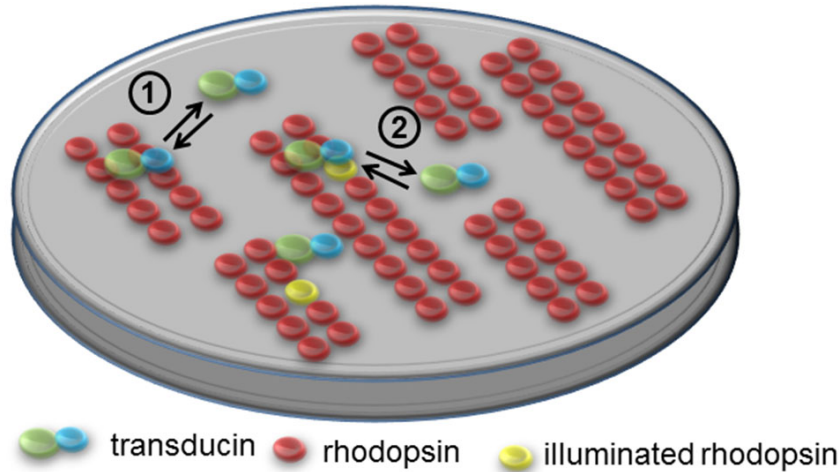


Figure 1.4: The dynamic scaffolding mechanism illustrated on a disc membrane surface. Rhodopsin dimers (red) form tracks, with which transducin (blue-green) can rapidly associate and dissociate. As soon as transducin associates with an activated rhodopsin molecule (yellow) it will be activated. Copyright ©2015 Koch and Dell’Orco, from (Koch and Dell’Orco, 2015).

The dynamic scaffolding mechanism has been studied computationally (Dell’Orco, 2013), (Schöneberg et al., 2014) and may in part explain the observed ratio between failures to respond to light and single photon responses (Cangiano and Dell’Orco, 2012). The hypothesis of dynamic scaffolding is supported by recent experimental results using single-molecule tracking of rhodopsin (Hayashi et al., 2019).

1.1.6 The single photon response

The phototransduction cascade in rods is functional in different light regimes and uses different mechanisms to escape saturation and remain functional and reactive. In conditions of a steady background illumination, *light adaptation* plays a significant role in decreasing the change in circulating current ΔJ and in increasing the speed at which the system can recover from additional stimuli. We will later discuss a mechanism of light adaptation in section 3.2.

An effect that is arguably even more interesting is the dim light dynamics of the

1.1. THE PHOTOTRANSDUCTION CASCADE

phototransduction cascade in rods. It is so sensitive to dim stimuli that it has a reproducible response to single photons - that is, to one single photon and thus one photoisomerization of rhodopsin per outer segment (Baylor et al., 1979). This could be determined from the relative frequencies of failures to respond to single photon responses and multiple photon responses, which are given according to the Poisson distribution.

There is experimental evidence that already few photons are detected by the human retina (Hecht et al., 1942), (Sakitt, 1972). However, the reliable detection and transmission of single photon signals is a challenge to the whole visual system: There is a convergence of about 1000 rods to one ganglion cell, which are the last neuronal cell type before the optic nerve. If only a few of those 1000 rods detect a photon, there needs to be a selection mechanism for those responses in the retina, to prevent the responses from getting lost in the noise.

Specifically, the signal from about 20 rods converges to one single rod bipolar cell. These cells do not simply average over the signals - this would lead to single photon responses from few rods being drowned in the dark noise from the remaining rods that did not produce a signal. Instead, there seems to be an amplitude thresholding that is applied to the signals, which filters out the responses of rods that actually received a photon (Field and Rieke, 2002). This enables the rod bipolar cells to increase the signal to noise ratio even when receiving few single photon responses.

Further downstream, the signal from rods is transmitted through amacrine cells to the cone bipolar cells, piggybacking on the cone signal transduction pathway. At the synapse between the cone bipolar cells and the ganglion cells, there is again a nonlinear transmission mechanism to reject noise and to selectively transmit the signals arising from single photon detection upstream (Ala-Laurila and Rieke, 2014).

Thus, it is obviously important for the visual sense that single photon responses have a low variability: they need to be reliably selected for a signal detection downstream. This is in fact the case: single photon responses are less variable than other signalling events arising from single molecule activations (Rieke and Baylor, 1998). There is a need for a reproducible activation of the cascade and a reproducible shut-off. For the activation, this means that the G-protein has to reliably and quickly associate to rhodopsin in order to start the cascade. For the shut-off, it is required that the variability of the lifetime of the activated rhodopsin

is low, and that the other activated molecular species are quickly deactivated. Since the variability of the single photon response is lower than one would expect for a single-step shut-off process, there must be a multi-step shut-off process (Hamer et al., 2003). Thus, not only arrestin is responsible for the shut-off. As explained before, the phosphorylation of rhodopsin by the rhodopsin kinase plays a significant role in the shut-off as well.

How can the single photon response have such a low variability? This question can be approached using computational modelling: in a computational model, we are able to modify every component of the signalling cascade and investigate the resulting changes on e.g. the single photon response. Furthermore, since the phototransduction cascade is an exceptionally well-studied system, it lends itself well to quantitative modelling since many of the necessary parameters are known or can be estimated from experiments. In the next section, we will explain the basis of this type of modelling and previous work done in the field.

1.2 Modelling phototransduction

Phototransduction modelling has a long history, with models becoming more and more detailed and refined as more information and computational power has become available.

The first models of phototransduction were developed in the 1990s and only described the activation steps of the cascade up to the G-protein or the effector (Kahlert and Hofmann, 1991), (Lamb and Pugh Jr, 1992). Those models are based on mass-action kinetics in the well-stirred approximation and the resulting differential equations (cf. chapter 2). Since they only involve few reactions, it is possible to treat them analytically as well as numerically. The models describe phototransduction in amphibian species, since most data were available for amphibian rods - this has now changed and the best studied model organism is the mouse.

Not much later, the first stochastic modelling approaches, again of the activation of the cascade, were carried out. Two main alternatives for the stochastic simulations were explored: firstly, the simulation of the chemical master equation, which is based on the same equations as the differential equations, but deals with integer numbers of the involved molecular species instead of continuous concentrations as before (cf. chapter 2). Secondly, space-resolved simulations were performed, where the involved molecules can diffuse in space, constrained to a lattice geometry. Of-

ten, the dimensionality of the rod is reduced to two dimensions (for the reactions occurring on, or close to, the disc membranes) or one dimension (for the species diffusing through the entire cytosol in the outer segment). (Lamb, 1994), (Felber et al., 1996)

The models were constantly expanded, most notably to also include species downstream of the effector and shut-off reactions (e.g. (Hamer et al., 2003) and (Dell’Orco et al., 2009)). This also allowed for very detailed studies of the dynamics and the variability of the different activation and deactivation steps, e.g. focussing on the PDE (Reingruber and Holcman, 2008) or the diffusion of the second messengers (Bisegna et al., 2008).

Increasingly, models were also adapted to fit to the much faster kinetics in mammalian species, due to an increase of experimental data for these species (e.g. (Invergo et al., 2014) and (Reingruber et al., 2013)). Furthermore, they became more and more complex to account for light responses in all intensity regimes, from the single photon response up to the bright light regime, as e.g. (Dell’Orco et al., 2009), (Hamer et al., 2005), (Invergo et al., 2014) and (Tikidji-Hamburyan et al., 2017).

Most recently, models have been improved to include novel experimental results on the dimeric activation of the PDE (Lamb et al., 2018), and include more detailed space-resolved modelling for the activation steps of the cascade (Lamb and Kraft, 2020).

The guiding principle of the phototransduction modelling presented in this thesis is the following: The reactions of the phototransduction cascade are represented as accurately as possible in the model. Of the necessary parameters, such as reaction rates, as many as possible are acquired from literature. The aim is to produce a comprehensive model of the phototransduction cascade, which includes all the necessary species with mass-action kinetics wherever possible.

This model can then be used - without retuning any of the parameters - to simulate light responses in different light conditions. This fulfills three purposes. First, to *verify* that the model reproduces well-known experimental results. Second, to make *predictions* of the phototransduction cascade in settings that have not yet been experimentally verified or that would be difficult or impossible to check experimentally. This also means that we can explore the consequences of point mutations in proteins, for which experimental *in vitro* data are available, on the photoresponse. And third, to *find gaps in our current knowledge* about the pho-

CHAPTER 1. INTRODUCTION

phototransduction cascade, by identifying phenomena that cannot be explained with the model yet.

Compared to other work, we want to create a model that is *comprehensive*, thus, it should include all the necessary mechanisms to account for light responses in different light conditions *explicitly*. While space-resolved modelling has the advantage of accurately resolving diffusion on the two-dimensional disc membrane and its specific effects on the cascade, it also involves many parameters that need to be estimated, and is very intensive concerning the computational effort. Thus, our model is based on the *well-stirred assumption* and is not space-resolved, which allows for much faster simulations.

Furthermore, our model should account for the dynamic behaviour of the entire phototransduction cascade in *all* light regimes. We want to stochastically simulate single photon responses and deterministically simulate bright light responses, ideally with the same model.

The models I have implemented are based on two previous models: the amphibian model implemented by Dell’Orco *et al.* (Dell’Orco *et al.*, 2009) and the mouse model by Invergo *et al.* (Invergo *et al.*, 2014), which is based on the amphibian model. Both models build on a previous study by Hamer *et al.* (Hamer *et al.*, 2003) and refine and expand the model.

The amphibian model describes phototransduction in amphibian rods and is valid for a broad range of light regimes and genetic knockouts. The mouse model’s parameters are adapted to the faster kinetics in mammalian species and a few mechanisms were refined compared to the previous model. The mouse model also reproduces the salient features of rod phototransduction in dim to bright light regimes and in animals with genetic modifications. The two models are described in more detail in section 2.3.

I have created stochastic versions of these models and adapted them to include novel experimental results, as well as simulated bright light responses in different conditions. Furthermore, I have created a novel stochastic model based on the mouse model. This is described in chapters 3 and 4.

2 | Methods

The aim of the research in this thesis is to model the phototransduction cascade in rods, both improving the pre-existing deterministic models and creating stochastic models. In this chapter, the basics for the modelling are explained. First, the modelling framework will be established, and it will be explained how to create a mathematical model of a biochemical signalling cascade. Then, it will be shown how to use this model to predict the system's behaviour in given conditions by performing deterministic and stochastic simulations.

2.1 Modelling framework

Mathematical modelling is a powerful tool to describe any sort of systems and predict their behaviour in different settings. A mathematical model of a given system describes the state and interactions of this system in a mathematical language. Therefore, it is an abstraction of the real system and usually contains simplifications.

Typically, we can define the spatial and temporal scale of a model and ignore the effect of much smaller scale interactions. For example, when we want to model the motion of planets in a solar system, we can ignore the effect of the motion of, e.g., tectonic plates or animals on the single planets - the dynamics on that scale are too small to affect the planetary motion.

Similarly, we can ignore effects that can be considered to be constant on the temporal and spatial scale of the model. For example, when describing the motion of an electron in the Earth's magnetic field for a few minutes, we can ignore the slow change of the magnetic poles on the Earth (which occurs on the scale of hundreds of years) as well as the change of the magnetic field inclination with the position - we can assume the field to be constant.

Mathematical models can describe any kind of system, from subatomic particles to the entire universe. They can describe physical and astronomical systems, like in the examples given above, chemical interactions such as the time-dependent

amount of reactants when synthesizing a product, or biological phenomena like population dynamics in a predator-prey system. They are also applied to social sciences, for instance in economy when describing the stock exchange, or political sciences when modelling voter behaviour in an election.

The most promising fields for modelling approaches at this moment are arguably the biological and medical fields. We are at a point in time where large amounts of data become readily available, such as large scale genome analyses or gene expression data. This type of data is of such size and complexity that humans are incapable of easily interpreting them: we are in need of algorithms to make sense of the data, to detect correlations and to create underlying models.

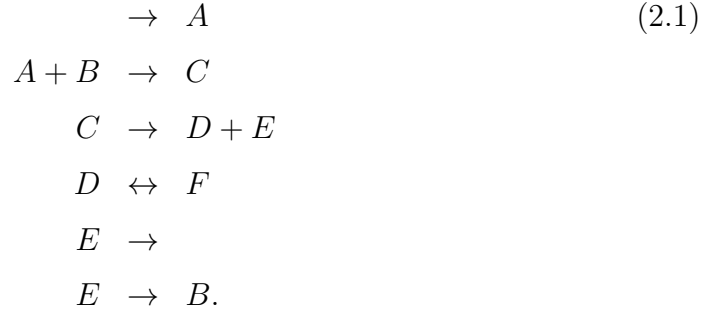
Signalling cascades are good examples of these complex systems. Organisms use them to integrate information from inside or outside their own cells to adapt their behaviour. For example, bacteria may use a signalling cascade which detects available nutrients around them to adapt their metabolism by changing the gene expression. These signalling cascades are typically quite complex due to the large number of interacting species and due to feedback mechanisms. Therefore, models are needed to understand the interactions and to make quantitative predictions of the system in question.

Another example of a signalling cascade is the phototransduction cascade: it relays the information from a visual stimulus to downstream neurons. Though it is quite complex, it is well-studied and thus well suited to modelling approaches. The appropriate modelling framework for such signalling cascades are biochemical reaction networks, which will be explained in the following section.

2.1.1 Biochemical reaction networks

Biochemical reaction networks describe the interaction of chemical species in a biological setting, for example different proteins or ions in a cell. The ingredients for the modelling are the molecular species and their interactions. Furthermore, if an external stimulus such as light stimulation plays a role, we need to define it and its interaction with the species of the model. For further reading on the basics explaining in this section, please refer to (Ingalls, 2012).

We describe the time-dependent concentration of each molecular species as a variable and their interaction by reaction equations, which can be formulated as differential equations. This is best understood using an example, so let us consider the following reactions:



The reaction network described by these reactions is shown in figure 2.1. It consists of six species labelled A to F , which can interact with each other. The possible reactions are characterized by their interaction partners, reactants which react to produce products, as well as the reaction rate constants k_0 to k_5 .

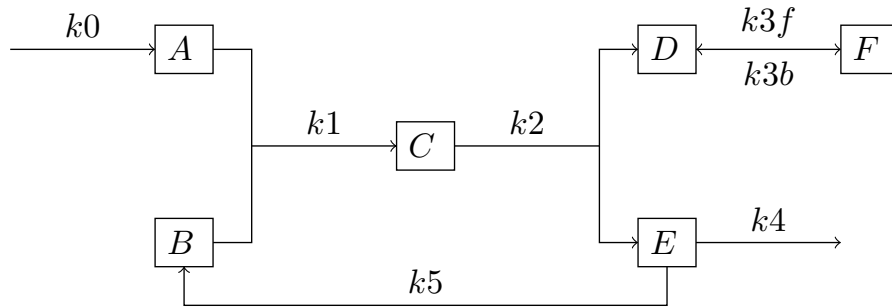


Figure 2.1: An exemplary chemical reaction network. The letters A , B , C , D , E and F stand for the interacting species, while k_1 to k_5 are the reaction rate constants.

Let us investigate some of the possible reactions in this scheme. The reaction characterized by the rate k_0 produces A , seemingly out of thin air. This is the case when a species of the model is produced by some process whose exact details are outside the scope of the model. The result will be an influx of species A .

Next, let us look at the reaction characterized by k_1 . It consumes A and B in equal parts and produces C . The reaction rate constant is k_1 , but the reaction rate v_f itself is proportional to the amounts of A and B , since they have to be available for the reaction to occur:

$$v_f = k_1 \cdot A \cdot B. \tag{2.2}$$

This is called the law of *mass action*: the reaction rate is proportional to the reaction rate constant and the amount of the reactant species.

CHAPTER 2. METHODS

Species C can then go on to produce D and E with the rate constant k_2 . The rate of this reaction is proportional to the concentration of C . D can react to F with the rate constant k_3 , and F can react back to D with the rate constant k_4 . This is a reversible reaction: it can occur in both directions.

E can react to nothing with the rate constant k_5 . For the purpose of our model, it is destroyed. More realistically, it would react to some reactant that is not included in the model, and can therefore be ignored.

Finally, the reaction with the rate constant k_6 converts E to B . This introduces a *feedback* into our model. Without this reaction, a clear up- and downstream could be defined: The species go from A and B through C to D , E and F . Now, we have introduced a cycle in our model.

Without the reactions characterized by k_0 and k_4 , our model would be considered *closed*: there would be no reactants or products outside the network. The consequence of this is that we could define *conservation laws* for the species involved. The steady state of a closed reaction network is the *thermal equilibrium*, where all reaction rates have gone to zero.

However, since we have included these reactions, the reaction network is *open*. In this type of reaction networks, we can also achieve a steady state, the *dynamic equilibrium*: in this state, all reaction rates are constant but not necessarily zero, resulting in a steady state for the species and a constant flux through the network.

In this reaction network, there is no reaction that requires more than two reactants. This is typically the case, and it is due to the fact that the reactant species need to meet at the same time and same place and at the correct spatial configuration in order for the reaction to occur. If three or more reactants were involved in a reaction, this would be prohibitively improbable. If a reaction requires three species to occur, typically two of the species would form a precomplex, which would then react with the third species.

We can also write down the differential equations describing the above chemical reaction network. We will use the assumption of *mass-action kinetics*: that the reaction rate is proportional to the reaction rate constant and the amount of the reactant species. Furthermore, we will assume that the reaction volume is *well-stirred*, meaning that there is no spatial dependency of the species' concentrations and that changes in the concentrations are instantaneous. The differential equa-

tions for the time-dependent species' concentrations then read:

$$\begin{aligned}
 \frac{d}{dt}A &= -k_1 \cdot A \cdot B + k_0 \\
 \frac{d}{dt}B &= -k_1 \cdot A \cdot B + k_5 \cdot E \\
 \frac{d}{dt}C &= k_1 \cdot A \cdot B - k_2 \cdot C \\
 \frac{d}{dt}D &= k_2 \cdot C - k_3f \cdot D + k_3b \cdot F \\
 \frac{d}{dt}E &= -k_4 \cdot E - k_5 \cdot E \\
 \frac{d}{dt}F &= k_3f \cdot D - k_3b \cdot F.
 \end{aligned} \tag{2.3}$$

The equations directly follow from the reaction equations in equation (2.1) combined with mass-action kinetics, as we can see e.g. in the example of the third reaction in equation (2.3): The change of the concentration C , $\frac{d}{dt}C$, is characterized by an influx and an outflux. The influx comes from the reaction $A + B \rightarrow C$ and is proportional to the reaction rate k_1 as well as the reactant concentrations A and B . The outflux comes from the reaction $C \rightarrow D + E$. It is negative because it consumes C , and it is proportional to the reaction rate k_2 as well as the reactant concentration C . Please note that, in mass-action kinetics, the concentration of the product itself does not influence the reaction rate, unless the product is a reactant at the same time.

The other differential equations are constructed in the same manner. We now have a *system of differential equations*, which are *coupled*: the change of one species depends on the other species. These equations contain all the information we have about the model and are equivalent to figure 2.1.

If we are interested in determining how the system would evolve in a given situation, we need to further specify the *initial conditions* for all species, $A(0)$ to $F(0)$. When we then solve the differential equations with the given initial conditions, we arrive at the time series $A(t)$ to $F(t)$ for all the species. In principle, we now know everything there is to know about the model with the given initial conditions. We can input any desired time point into the time series $A(t)$ to $F(t)$ and determine the individual species concentrations in that moment, or look at the entire time series. In subsection 2.1.3, we will discuss how to solve the differential equations.

2.1.2 Reaction rate constants and affinities

The reaction rates are an important ingredient for the modelling. In this section I will give more background on their biochemical significance and how to determine them.

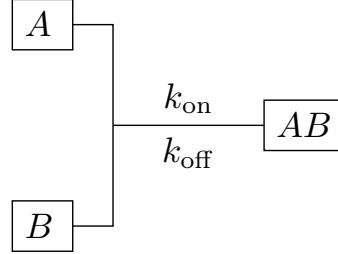


Figure 2.2: An example of a small reaction network. A and B can associate with the rate constant k_{on} to form AB , which can in turn dissociate to A and B with the rate constant k_{off} .

Let us consider a very simple reaction network, as shown in figure 2.2. It consists of three molecular species: A , B and the complex AB which is formed when A and B associate. The association occurs with the rate constant k_{on} , while the dissociation occurs with k_{off} . According to mass-action kinetics, the on- and off-rates v_f and v_r are then:

$$\begin{aligned} v_f &= k_{\text{on}} \cdot A \cdot B \\ v_r &= k_{\text{off}} \cdot AB. \end{aligned} \tag{2.4}$$

In equilibrium, the rates balance, leading to constant concentrations:

$$k_{\text{on}} \cdot A_{\text{eq}} \cdot B_{\text{eq}} = k_{\text{off}} \cdot AB_{\text{eq}}. \tag{2.5}$$

We can then define the *association constant* K_a as

$$K_a = \frac{k_{\text{on}}}{k_{\text{off}}} = \frac{AB_{\text{eq}}}{A_{\text{eq}}B_{\text{eq}}} \tag{2.6}$$

and the *dissociation constant* K_d as

$$K_d = \frac{k_{\text{off}}}{k_{\text{on}}} = \frac{A_{\text{eq}}B_{\text{eq}}}{AB_{\text{eq}}}. \tag{2.7}$$

When measuring the concentrations A_{eq} , B_{eq} and AB_{eq} in an experiment, we can determine the association and dissociation constants and thus the ratio of the

on- and off-rate constants k_{on} and k_{off} . Measuring the rate constants directly is much more involved and requires more intricate biophysical methods like surface plasmon resonance, where one of the interacting partners is immobilized close to a metal layer and the other interacting partner flows over the surface. By a change of the refractive index in the vicinity of the surface resulting from association and dissociation of the interacting biomolecules, the reaction rate constants can be determined.

2.1.3 Steady state and dynamics

Having constructed our model from the species and their interactions, we now want to use it to extract some information on the system and its (dynamic) behaviour. The first point of interest may be the *steady state* of the system. It is reached when the concentrations of the species are no longer changing, and thus all derivatives $\frac{d}{dt}x(t)$ for the states $x(t)$ become zero. We can therefore set $\frac{d}{dt}x(t) = 0$ in the system of coupled differential equations and solve it to get the steady state.

Finding the general solution for the system's dynamic behaviour is a little bit more involved. There are procedures for solving coupled differential equations, and in the case of chemical reaction networks one would typically choose an *Ansatz*, insert it into the differential equations, and solve them.

However, for larger systems, this quickly becomes very difficult or impossible. Identifying conserved quantities and steady states and making simplifying assumptions can help, but at some point it becomes impossible to find analytical solutions. At this point we turn to computers for help.

2.2 Simulations

When it becomes impossible to find an analytical solution to the model, we can use computers. We can solve the differential equations by performing a *simulation* of the model: we basically proceed in small steps, starting at the initial conditions, and calculate how our variables $x(t)$ have changed in each step. This is only an approximation of the true solution, and it will only give us the variable values at discrete time points. But if we choose sufficiently small time steps, it will be a very good approximation. In the following subsections, I will present the basic theory underlying this type of simulations. For further reading and example code, please refer to (Press et al., 2007).

2.2.1 Euler method

The most basic method to numerically solve a system of coupled ordinary differential equations with initial conditions is the *Euler method*. We start out with a number of variables $x_i(t)$ that we can group into a vector $\vec{x}(t)$, the initial conditions $\vec{x}(0)$, and the system of differential equations in the form

$$\frac{d}{dt}\vec{x}(t) = \vec{H}(\vec{x}(t), t). \quad (2.8)$$

In our example in equation (2.3), the vectors $\vec{x}(t)$ and $\vec{H}(\vec{x}(t), t)$ would look like this:

$$\vec{x}(t) = \begin{pmatrix} A(t) \\ B(t) \\ C(t) \\ D(t) \\ E(t) \\ F(t) \end{pmatrix} \quad \vec{H}(t) = \begin{pmatrix} k1 \cdot A \cdot B + k0 \\ -k1 \cdot A \cdot B + k5 \cdot E \\ k1 \cdot A \cdot B - k2 \cdot C \\ k2 \cdot C - k3f \cdot D + k3b \cdot F \\ -k4 \cdot E - k5 \cdot E \\ k3f \cdot D - k3b \cdot F \end{pmatrix}. \quad (2.9)$$

The vector $\vec{H}(\vec{x}(t), t)$ contains the derivatives of the variables $x_i(t)$. If we insert the variables at a time point t , we get the local slope of each of the variables. So if we know all variable values at a given time point t , we can insert them into $\vec{H}(\vec{x}(t), t)$ and approximate the variables at a time point $t + \tau$:

$$\vec{x}(t + \tau) = \vec{x}(t) + \tau \cdot \vec{H}(\vec{x}(t), t) + O(\tau^2). \quad (2.10)$$

This is called an *Euler step*. It is a direct consequence from the fact that $\vec{H}(\vec{x}(t), t) = \frac{d}{dt}\vec{x}(t)$ and the approximation of the derivative:

$$\frac{\vec{x}(t + \tau) - \vec{x}(t)}{\tau} + O(\tau) = \frac{d}{dt}\vec{x}(t). \quad (2.11)$$

$O(\tau)$ is an error which does not grow significantly faster than τ . When we divide by τ to arrive at equation (2.10), we get an error of order $O(\tau^2)$, which does not grow significantly faster than τ^2 . For a small step size τ , this is a stricter bound. Thus, the smaller we choose the step size τ , the smaller (quadratically!) the estimation error.

Coming back to our problem of determining a concrete solution for the variables

$\vec{x}(t)$, we do know the variables at a given time point, namely from the initial conditions $\vec{x}(0)$. Thus, we can start at $t = 0$ and determine the slopes $\vec{x}(t)$ at $t = 0$ by inserting the initial conditions $\vec{x}(0)$ into $\vec{H}(\vec{x}(t), t)$. This will give us the variables at time point τ .

We can iterate the procedure to get from $\vec{x}(\tau)$ to $\vec{x}(2\tau)$, so that we finally arrive at a time series of n values $\vec{x}(n \cdot \tau)$. This procedure is called the *Euler method*. From this basic Euler method, many more complex procedures have been established to decrease the size of the error and to overcome instabilities which would only allow good solutions for very small time steps.

2.2.2 4th order Runge-Kutta

This method is an extension of the Euler method, and decreases the size of the error to $O(\tau^4)$ (which is why it is called 4th order). It is usually simply referred to the *Runge-Kutta method*, since it is the standard Runge-Kutta method to solve a system of coupled differential equations. (Runge, 1895), (Kutta, 1901)

The basic idea of the method is to perform three Euler steps, two with step size $\tau/2$ and one with step size τ . We consecutively calculate the slopes:

$$\begin{aligned}\vec{H}_1 &= \vec{H}(\vec{x}(t), t) \\ \vec{H}_2 &= \vec{H}(\vec{x}(t) + 1/2 \cdot \tau \cdot \vec{H}_1, t + 1/2\tau) \\ \vec{H}_3 &= \vec{H}(\vec{x}(t) + 1/2 \cdot \tau \cdot \vec{H}_2, t + 1/2\tau) \\ \vec{H}_4 &= \vec{H}(\vec{x}(t) + \tau \cdot \vec{H}_3, t + \tau).\end{aligned}\tag{2.12}$$

\vec{H}_1 is the slope at the beginning of the interval. \vec{H}_2 is the slope at the midpoint $\tau/2$ of the interval, using variables $\vec{x}(t + \tau/2)$ determined from the slope \vec{H}_1 . \vec{H}_3 is again the slope at the midpoint, but this time using variable values calculated with \vec{H}_2 . \vec{H}_4 is the slope at the endpoint of the interval, calculated with the slope \vec{H}_3 . We can then calculate the variables at time point $t + \tau$ in the following fashion:

$$\vec{x}(t + \tau) = \vec{x}(t) + \tau \cdot (1/6 \cdot \vec{H}_1 + 1/3 \cdot \vec{H}_2 + 1/3 \cdot \vec{H}_3 + 1/6 \cdot \vec{H}_4) + O(\tau^4).\tag{2.13}$$

Note the the error is now $O(\tau^4)$, which is significantly smaller than $O(\tau^2)$ for small τ .

2.2.3 Generalized and implicit Runge-Kutta

While the 4th order Runge-Kutta method is the most commonly used method due to its trade-off between speed and accuracy, it is only one of many possible Runge-Kutta schemes. The general equation is formulated as follows:

$$\vec{x}(t + \tau) = \vec{x}(t) + \tau \sum_{i=1}^s b_i \cdot \vec{k}_i, \quad (2.14)$$

where s is the number of stages, the b_i are coefficients (numbers like $1/3$ and $1/6$ in equation (2.13)) and the k_i can be calculated iteratively as follows:

$$\vec{k}_i = \vec{H} \left(\vec{x}(t) + \tau \cdot \left(\sum_{j=1}^{i-1} a_{ij} \vec{k}_j \right), t + c_i \tau \right). \quad (2.15)$$

The c_i and a_{ij} are again coefficients. The \vec{k}_i are the slopes calculated at different extrapolation points, which are averaged in equation (2.14) to give an estimate of the next time point $\vec{x}(t + \tau)$. Please note that the \vec{k}_i can be calculated iteratively: each \vec{k}_i may depend on the \vec{k}_j before it with smaller index $j < i$, but not those after it.

Unfortunately, these general Runge-Kutta methods, called *explicit Runge-Kutta methods*, are unstable for certain types of differential equations. When they are applied to the simple Kepler problem of a planet orbiting a sun, the solution becomes unstable and spirals outwards instead of forming a stable orbit as it should. The solution's region of stability is highly dependent on the step size in this method.

This problem is improved upon by the *implicit* Runge-Kutta method. It works as follows:

$$\vec{x}(t + \tau) = \vec{x}(t) + \tau \sum_{i=1}^s b_i \cdot \vec{k}_i, \quad (2.16)$$

with

$$\vec{k}_i = \vec{H} \left(\vec{x}(t) + \tau \cdot \left(\sum_{j=1}^s a_{ij} \vec{k}_j \right), t + c_i \tau \right). \quad (2.17)$$

The main difference to the explicit Runge-Kutta method is the range of the sum in equation (2.17): it now extends to the full number of stages s for each sum. This means that we cannot calculate the \vec{k}_i iteratively anymore. Instead, equation (2.17) will produce a system of linear equations for the \vec{k}_i that has to be solved

algebraically. This increases the numerical cost, but leads to a greater stability of the solutions.

Typically, this procedure is combined with an *adaptive* Runge-Kutta method: this is a combination of two Runge-Kutta algorithms running in parallel, one of order n and one of order $n-1$. The two algorithms' results can be compared at intermediate steps and can be used to calculate an error. The step size of the two methods can then be adjusted according to the error, so that the error stays beneath a user-defined threshold. This saves computational cost: the algorithm allows for larger steps when the error is low, but uses small steps as required to keep the error small.

2.2.4 The Gillespie algorithm

So far, we have investigated how to solve the differential equations describing the model while treating the molecular species' concentrations as continuous numbers. But what if the number of the molecular species we are describing cannot be treated as a continuous number? This is the case when we are considering small numbers of molecules, say below 100. This brings with it two different issues.

Firstly, the number of molecules is so small that it becomes coarse-grained and we cannot approximate it well using a continuous number. Doing calculations which involve 0.1 molecules makes no sense: either there are 0 or 1 molecules.

Secondly, *randomness* starts to play a role. If the deterministic simulation gives us a result of 0.1 molecules for a given time step, this means that there would be 0.1 molecules *on average*. In reality, this could be 0, or 1, or 2, or ... molecules. It is intuitively clear that this would make a big difference to the outcome of the simulations. With deterministic simulations, we can still make statements for the *average* behaviour of the model system, but in reality, each realization of the system would yield a different results simply due to pure chance. If we are interested in the statistical characteristics of those realizations, such as the variability, we have to perform *stochastic simulations*.

A very current example of this is the statistics of cases of an infectious disease: deterministic simulations can inform us about the average behaviour, but to correctly reflect the highly stochastic and localized nature of disease outbreaks, we need stochastic simulations.

To perform stochastic simulations, we use the same reaction equations from equa-

tion (2.1), however we need to treat them differently. We cannot translate the reaction equations to the differential equations from equation (2.3) anymore, since this assumes that the species are continuous quantities. Instead of treating the different molecular species as continuous quantities and the reactions as continuous fluxes, we now treat the species as integer numbers and the reactions as separate events. To perform simulations, we consider the separate reactions one by one. This is called the *Gillespie Algorithm* (Gillespie, 1977).

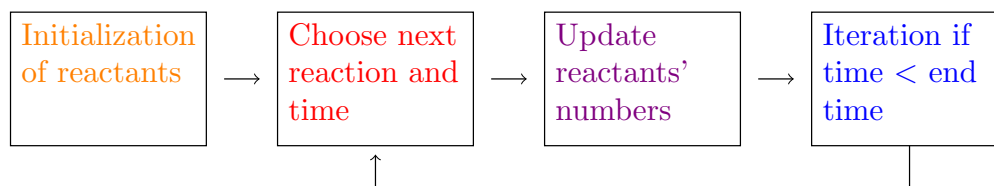


Figure 2.3: Schematic of the Gillespie algorithm.

The basic mechanism of the algorithm is schematically shown in figure 2.3. First, the initial conditions are used to initialize all reactant numbers. Then, we need to pick a reaction as well as the waiting time until it occurs randomly. How this is done will be explained in detail below. When a reaction has been chosen, the next step is to carry out the changes of this reaction on the reactant concentrations: they are updated to reflect the decrease in reactant species and the increase in product species. The simulation time is advanced by the wait time.

In the next step, it is checked whether the total time exceeds the specified simulation time - if this is not the case, the simulation continues, and the main simulation step is iterated: the next reaction will be chosen and carried out.

In the reaction step, we need to ensure that the reactions occur with the correct statistics. We want to pick reactions at random, but each of them should happen with the correct relative frequency and with correct statistics of the waiting time in between reactions. The Gillespie algorithm has an elegant solution to ensure this.

Imagine a reaction with reactants A and B and product C , occurring with a rate constant k_1 . Then the total rate of the reaction will equal to $r_1 = A \cdot B \cdot k_1$. This is the instantaneous rate, its unit is molecules/ s since it denotes the change of C . The mean time between reactions will be $1/r_1$. When we consider all the reactions in a given reaction network, we can define a total rate of all reactions that can

occur:

$$r_{\text{tot}} = \sum_{i=0}^{n-1} r_i, \quad (2.18)$$

where the sum extends over all n rates in the reaction network. The mean time until *any* reaction occurs in this network is $1/r_{\text{tot}}$.

To perform the simulations, we also need to know the probability distribution of times between reactions to choose reaction times that not only give the correct mean reaction time, but also the correct statistics. It can be shown that the times between reactions are exponentially distributed, since the reactions are independent of each other (except for the change of the reactant). Processes with this characteristic are called *Markov processes*, and another example is radioactive decay: the time in between independent decay events is also exponentially distributed.

We can assign a waiting time between reactions by drawing exponentially distributed random numbers, which is typically done by computing

$$\tau = \frac{1}{r_{\text{tot}} \log \left(\frac{1}{U_1} \right)}, \quad (2.19)$$

where U_1 is a random number drawn from a uniform distribution between 0 and 1. Consequently, $\log(1/U_1)$ is an exponentially distributed number between 0 and ∞ . This ensures that we will on average wait a time of $1/r_{\text{tot}}$ between reactions, and that the waiting times are exponentially distributed.

Next, it needs to be decided *which* reaction occurs at the newly determined time point. For each of the reactions, the probability to occur is r_i/r_{tot} . We can therefore create a new random number U_2 , uniformly distributed between 0 and 1, and find the smallest k for which

$$\sum_{i=0}^k r_i > r_{\text{tot}} \cdot U_2. \quad (2.20)$$

Using this procedure, each reaction is chosen proportionally to the width of the interval that they contribute to the sum representing r_{tot} , and thus proportionally to r_i/r_{tot} .

After the reaction and its waiting time have been determined, the reaction is carried out, which means that the total simulation time is advanced by the waiting time and the molecule numbers are updated according to the reaction that has occurred. Then, if the total simulation time has not been exceeded, another step can be carried out: first, the reaction rates have to be updated according to the

new reactant numbers. Then, the random procedure is again used to pick the next reaction and waiting time.

Using the Gillespie algorithm, a stochastic simulation of a system of reaction equations can be carried out. We now have all the tools needed to build a model and to carry out both stochastic and deterministic simulations.

2.3 Basis of the modelling

The models I present in the results chapters 3 and 4 are based on two previously published modelling approaches: the amphibian model by Dell’Orco *et al.* (Dell’Orco *et al.*, 2009) and the mouse model by Invergo *et al.* (Invergo *et al.*, 2014). More information on how to build a model and use it for simulations can also be found in (Dell’Orco, 2015). The models have also been used to investigate different phenomena in slightly modified versions (Invergo *et al.*, 2014), (Dell’Orco and Koch, 2010). In this section, I will describe the two models by describing their structure and the interactions of their species.

2.3.1 The Dell’Orco 2009 model

The Dell’Orco 2009 model was developed to comprehensively model the phototransduction cascade in amphibians in different light regimes. Figure 2.4 shows the biochemical network structure of the model. The Invergo 2014 model mainly shares the same structure. The model consists of the reactions occurring in the phototransduction cascade as described in section 1.1. The outer box represents the outer segment, where the reactions take place. The coloured boxes represent the different molecular species. Connections represent reactions, with arrows indicating irreversible reactions and their direction. The colors of the boxes indicate active species in yellow and other species involved in signalling and shut-off in shades of grey and blue.

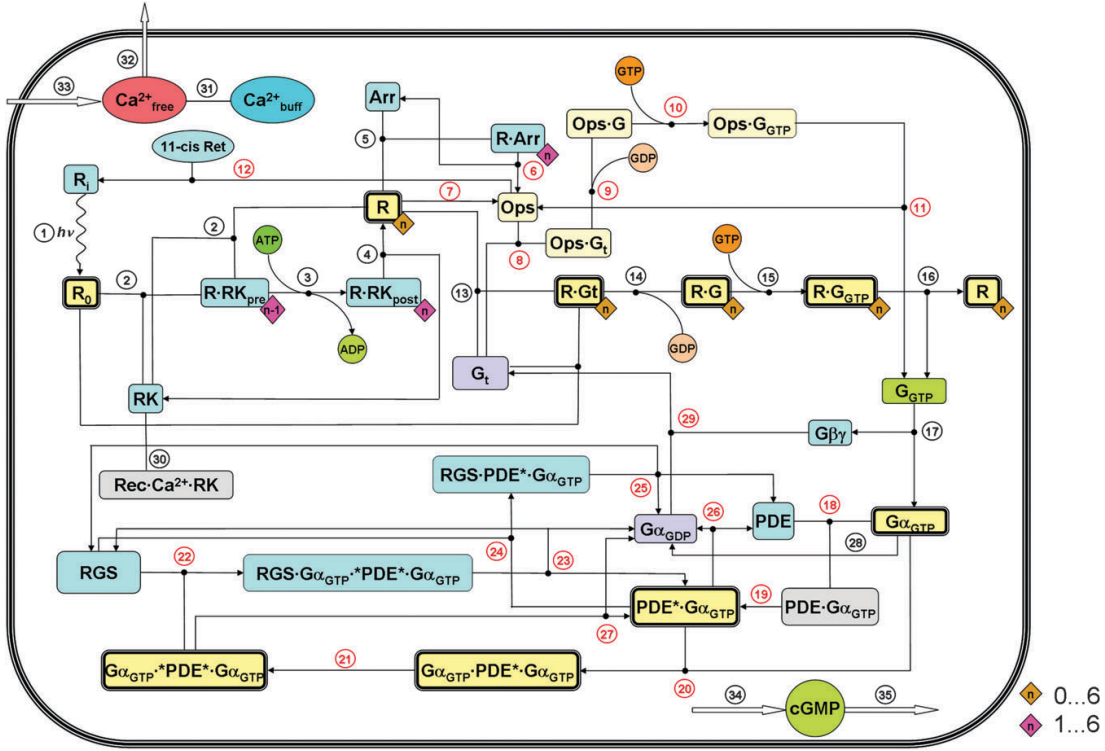


Figure 2.4: The complete biochemical network of the Dell'Orco 2009 model. The large box represents the outer segment. The boxes represent the different interacting molecular species, with active species in yellow, and other species involved in the signalling or shut-off in shades of grey and blue. The species involved in the amplification of the response have a bold box. Diamonds at the bottom indicate the phosphorylation state of rhodopsin species, ranging from 0 to 6 (orange) and 1 to 6 (pink). Connecting lines represent reactions, with arrows indicating irreversible reactions. The reactions are numbered and can be found in the supplementary information of (Dell'Orco et al., 2009) as reaction equations. Reprinted by permission from the Royal Society of Chemistry, from (Dell'Orco et al., 2009).

Let us follow the path of the signal through the model scheme. Please note that we will follow the reaction numbers, which are not necessarily in the order in which the reactions will occur. In the cases where the rates are not given by mass-action kinetics, they are given as formulas. The complete list of reaction equations and parameters can be found in the appendix.

The first step in phototransduction is the activation of rhodopsin. This is reaction 1 in the scheme. Rhodopsin in the inactive state R (R_i in the figure) is converted to R_0 , active rhodopsin that is phosphorylated 0 times. This is an active signalling molecule and thus marked yellow in the scheme. The rate of the reaction is proportional to the light stimulus S and to the fraction R of the total rhodopsin R_{tot} that is free to be activated:

$$v_f = S \cdot \frac{R}{R_{\text{tot}}}. \quad (2.21)$$

CHAPTER 2. METHODS

The stimulus S is expressed as follows:

$$\begin{aligned}
 S &= \text{background} + \text{preflash} + \text{testflash} + \text{otherstimulus} & (2.22) \\
 \text{background} &= \text{flashBG} \\
 \text{preflash} &= \begin{cases} \text{flash0Mag}/\text{flash0Dur} & \text{if } t \leq \text{flash0Dur} \\ 0 & \text{else} \end{cases} \\
 \text{testflash} &= \begin{cases} \text{flashmag}/\text{flashDur} & \text{if } \text{flashDel} \leq t \leq \text{flashDel} + \text{flashDur} \\ 0 & \text{else.} \end{cases}
 \end{aligned}$$

The total stimulus is defined as a sum of four different stimuli: a background, a preflash, a test flash and an extra stimulus (otherstimulus). The background is defined as a constant illumination of the intensity flashBG, which is given as a parameter in photons/ $\mu\text{m}^2\text{s}$. The preflash starts at time $t = 0$ and lasts for the duration flash0Dur. Its intensity is defined as flash0Mag/flash0Dur, with flash0Mag given as a parameter in photons/ μm^2 . The test flash starts at time $t = \text{flashDel}$ and lasts for flashDur. Its intensity is given as flashMag/flashDur, with flashMag again in photons/ μm^2 . The extra stimulus is a free parameter and can be defined as required.

The reactions **2** to **4** describe the phosphorylation of rhodopsin by the rhodopsin kinase (RK). It can bind to rhodopsin, forming the complex $\text{R} \cdot \text{RK}_{\text{pre}}$ with phosphorylation state $n - 1$ indicated in the small pink diamond in figure 2.4. In the pink diamonds, the phosphorylation state n goes from 1 to 6 (and thus $n - 1$ is between 0 and 5), while it goes from 0 to 6 in the orange diamonds. The phosphorylation reaction 3 consumes one ATP molecule and produces one ADP molecule, which is integrated in the reaction rate of this step. The result is the complex $\text{R} \cdot \text{RK}_{\text{post}}$ with phosphorylation state n increased by one (thus between 1 and 6). The complex can next dissociate to rhodopsin R_n and rhodopsin kinase.

The affinity of rhodopsin for the rhodopsin kinase depends on the phosphorylation state n of rhodopsin in this model. The rate constant $k_{\text{RK1},n}$ decreases exponentially with n :

$$k_{\text{RK1},n} = \begin{cases} k_{\text{RK1},0} \cdot e^{-\omega \cdot n} & n < 6 \\ 0 & n = 6, \end{cases} \quad (2.23)$$

with the parameters $k_{\text{RK1},0}$ describing the rate constant for $n = 0$ and ω describing the exponential increase of the rate constant with the phosphorylation state.

2.3. BASIS OF THE MODELLING

The affinity becomes zero for rhodopsin that has already been phosphorylated six times, since this is the maximum number of phosphorylations in the model.

Reactions **5** and **6** describe the shut-off of rhodopsin by arrestin. Rhodopsin and arrestin (Arr) can bind to create the complex $R \cdot \text{Arr}$, which can then dissociate to arrestin and opsin (Ops), the inactivated form of rhodopsin. Activated rhodopsin can also spontaneously shut off by decaying directly to opsin (reaction **7**).

The affinity of rhodopsin for arrestin also depends on the phosphorylation state of rhodopsin in the model. Specifically, the rate constant $k_{A1,n}$ of the binding reaction exponentially increases with the phosphorylation state n as follows:

$$k_{A1,n} = k_{\text{Arr}} \cdot e^{\omega_{\text{Arr}} \cdot n}, \quad (2.24)$$

with parameters k_{Arr} and ω_{Arr} . This reaction is only defined for $n \geq 1$, because it can only occur when rhodopsin has been phosphorylated at least once.

Reactions **8** to **11** describe the activation of the G-protein by opsin. Opsin has a very low activity, leading to some spontaneous activation events in the dark after the creation of opsin by, e.g., a bleach. This is equivalent to the activation of the G-protein by rhodopsin, which will be described in the next paragraph.

Reaction **12** is the recycling of opsin to rhodopsin. This reaction requires a fresh 11-cis-retinal, which is included implicitly in the reaction rate.

The next signalling step involving the active rhodopsin is the activation of the G-protein (Gt) in reactions **13** to **16**. In the first step, rhodopsin and transducin bind to form $R \cdot \text{Gt}$. Next, GDP is exchanged for GTP in two steps, leading to $R_n \cdot \text{G}$ and $R_n \cdot \text{G}_{\text{GTP}}$. The GDP and GTP are implicitly included in the reaction rates, respectively. Finally, the rhodopsin and G-protein dissociate to R_n and G_{GTP} . For the case of the G-protein being activated by opsin, the steps are the same, but with opsin instead of rhodopsin.

The affinity of rhodopsin for transducin decreases exponentially with the phosphorylation state n of rhodopsin in the model. The rate constant $k_{G1,n}$ depends on n as follows:

$$k_{G1,n} = k_{G1,0} \cdot e^{-\omega \cdot n}, \quad (2.25)$$

with the parameters $k_{G1,0}$, which is the rate constant for unphosphorylated rhodopsin, and ω , which is also used to describe the change in affinity for the rhodopsin

CHAPTER 2. METHODS

kinase.

Next, the G-protein dissociates into its α -subunit and β - and γ -subunits in reaction **17**. The products are $G_{\alpha\text{GTP}}$, the active α -subunit of the G-protein, and $G_{\beta\gamma}$.

Reactions **18** to **21** constitute the activation of the phosphodiesterase PDE by the G-protein. The first step is the binding of PDE and the G-protein to form $\text{PDE} \cdot G_{\alpha\text{GTP}}$ in reaction **18**. This complex is not yet active, since a conformational change needs to occur first. This is the next step in reaction **19**, yielding $\text{PDE}^* \cdot G_{\alpha\text{GTP}}$. This active form of PDE contributes to the effector (as defined in equation (2.31)) with half the full activity, since the PDE has two subunits that can both be activated by the G-protein. This is exactly what happens in reactions **20** and **21**: another G-protein is bound to form $G_{\alpha\text{GTP}} \cdot \text{PDE}^* \cdot G_{\alpha\text{GTP}}$, which then reacts to $G_{\alpha\text{GTP}} \cdot {}^*\text{PDE}^* \cdot G_{\alpha\text{GTP}}$, the fully active form.

The deactivation of the PDE mediated by the regulator of G-protein signalling (RGS) is described in reactions **22** to **25**. First, the PDE-G-complex binds RGS to form $\text{RGS} \cdot \text{PDE}^* \cdot G_{\alpha\text{GTP}}$ or $\text{RGS} \cdot G_{\alpha\text{GTP}} \cdot {}^*\text{PDE}^* \cdot G_{\alpha\text{GTP}}$, respectively, in reactions **22** and **24**. The first form dissociates to RGS, $G_{\alpha\text{GDP}}$ and PDE in reaction **25**, while the second form dissociates to RGS, $G_{\alpha\text{GDP}}$ and $\text{PDE}^* \cdot G_{\alpha\text{GTP}}$ in reaction **23**, still retaining half the full activity. Please note that the G-protein now is not active anymore, since it is bound to GDP instead of GTP.

The active PDE-G complex can be shut off by the intrinsic GTPase activity of the G-protein without binding to RGS. This is described by reactions **26** and **27**: $\text{PDE}^* \cdot G_{\alpha\text{GTP}}$ and $G_{\alpha\text{GTP}} \cdot {}^*\text{PDE}^* \cdot G_{\alpha\text{GTP}}$ decay to $G_{\alpha\text{GDP}}$ as well as PDE or $\text{PDE}^* \cdot G_{\alpha\text{GTP}}$, respectively.

The active α -subunit $G_{\alpha\text{GTP}}$ of the G-protein can also be shut off by the intrinsic GTPase activity: in reaction **28**, it decays to $G_{\alpha\text{GDP}}$. The inactive $G_{\alpha\text{GDP}}$ can recombine with the β - and γ -subunits $G_{\beta\gamma}$ in reaction **29** to produce transducin, which can then be activated by rhodopsin again.

Reaction **30** implements the recoverin-rhodopsin kinase regulation. The rhodopsin kinase can associate and dissociate with the recoverin (Rec) to form $\text{Rec} \cdot \text{Ca}^{2+} \cdot \text{RK}$. In the recoverin-bound state, it cannot phosphorylate the rhodopsin. In the model, the calcium-bound recoverin $\text{Rec} \cdot \text{Ca}^{2+}$ is not explicitly treated as a molecular species, but included in the reaction rate as a variable. It is calculated using Hill kinetics (Hill, 1910) from the total recoverin concentration Rec_{tot} and the free

2.3. BASIS OF THE MODELLING

Calcium concentration as follows:

$$\text{Rec} \cdot \text{Ca}^{2+} = \frac{\text{Rec}_{\text{tot}} - \text{Rec} \cdot \text{Ca}^{2+} * n_{\text{CF}}}{1 + \left(\frac{K_{\text{P}}}{\text{Ca}_{\text{free}}^{2+}} \right)^w}, \quad (2.26)$$

with the following parameters: n_{CF} , the conversion factor from molecule numbers to concentrations, K_{P} , the Ca^{2+} concentration causing half-maximal inhibition of recoverin, and w , the Hill coefficient for the action of Ca^{2+} on recoverin.

Reactions **31** to **33** describe the calcium dynamics in the model. In reaction **31**, the exchange of calcium between the free form $\text{Ca}_{\text{free}}^{2+}$ and the intracellular buffers $\text{Ca}_{\text{buff}}^{2+}$ is described with the following forward and backward rates v_{f} and v_{r} :

$$\begin{aligned} v_{\text{f}} &= k_1 \cdot (e_{\text{T}} - \text{Ca}_{\text{buff}}^{2+}) \cdot \text{Ca}_{\text{free}}^{2+} \\ v_{\text{r}} &= k_2 \cdot \text{Ca}_{\text{buff}}^{2+}, \end{aligned} \quad (2.27)$$

with rate constants k_1 and k_2 and the total buffer capacity e_{T} . This deviation from mass-action kinetics reflects the finite capacity of the buffers.

Reaction **32** represents the efflux of calcium via the ion exchangers. It is implemented with the rate:

$$v_{\text{f}} = \gamma_{\text{Ca}} \cdot (\text{Ca}_{\text{free}}^{2+} - \text{Ca}_0^{2+}), \quad (2.28)$$

with the rate constant γ_{Ca} and the minimum intracellular calcium concentration Ca_0^{2+} . Using this formula for the rate, $\text{Ca}_{\text{free}}^{2+}$ cannot become lower than Ca_0^{2+} .

The influx of calcium via cyclic nucleotide gated channels is described in reaction **33**. The reaction rate is

$$v_{\text{f}} = \frac{10^6 \cdot f_{\text{Ca}} \cdot J_{\text{dark}}}{(2 + f_{\text{Ca}}) \cdot F \cdot V_{\text{cyto}}} \cdot \left(\frac{\text{cGMP}}{\text{cGMP}_{\text{dark}}} \right)^{n_{\text{CG}}}, \quad (2.29)$$

with the following parameters: the fraction f_{Ca} of the circulating current carried by calcium, the dark current J_{dark} , the Faraday constant F , the cytoplasmic volume V_{cyto} , the dark cGMP concentration $\text{cGMP}_{\text{dark}}$ and the Hill coefficient n_{CG} for the opening of the cyclic nucleotide-gated channels. The reaction rate models the influence of the cGMP concentration on the influx of calcium ions into the cell.

Reactions **34** and **35** describe the synthesis and hydrolysis of cGMP, respectively. Reaction **34** implicitly contains the effect of the guanylate cyclase and its calcium-

CHAPTER 2. METHODS

dependent regulation by the guanylate cyclase activating proteins. Its rate is:

$$v_f = \frac{\alpha_{\max}}{1 + \left(\frac{\text{Ca}_{\text{free}}^{2+}}{K_C}\right)^m}, \quad (2.30)$$

where α_{\max} is the maximal rate of cGMP synthesis by the GCs, K_C is the calcium concentration at which cGMP synthesis is half-maximal and m is the Hill coefficient for the action of calcium on the cGMP synthesis rate.

cGMP is hydrolysed by activated PDE. The different light-activated forms of PDE are summarized in the effector E :

$$E = \text{PDE}^* \cdot \text{G}_{\alpha\text{GTP}} + \text{G}_{\alpha\text{GTP}} \cdot \text{PDE}^* \cdot \text{G}_{\alpha\text{GTP}} + 2 \cdot \text{G}_{\alpha\text{GTP}} \cdot {}^*\text{PDE}^* \cdot \text{G}_{\alpha\text{GTP}}. \quad (2.31)$$

The last term in the equation is multiplied by two because the PDE is active in both subunits and thus has the double activity. Then, the rate of cGMP hydrolysis is:

$$v_f = (\beta_{\text{dark}} + \beta_{\text{sub}} \cdot E) \cdot \text{cGMP}, \quad (2.32)$$

where β_{dark} is the dark rate of cGMP hydrolysis by spontaneously activated PDE and β_{sub} is the rate constant for cGMP hydrolysis by the effector, which represents the light-activated PDE.

The dark rate of cGMP hydrolysis and synthesis are connected, since they ensure that the cGMP concentration is in equilibrium in the dark. This is expressed by the formulation of the maximal cGMP hydrolysis rate:

$$\alpha_{\max} = \beta_{\text{dark}} \cdot \text{cGMP}_{\text{dark}} \cdot \left(1 + \left(\frac{\text{Ca}_{\text{dark}}^{2+}}{K_C}\right)^m\right). \quad (2.33)$$

When inserting this into the cGMP synthesis rate in equation (2.30) and setting $\text{Ca}_{\text{free}}^{2+}$ to $\text{Ca}_{\text{dark}}^{2+}$, as would be the case in the dark state, we arrive at $v_{f,\text{dark}} = \beta_{\text{dark}} \cdot \text{cGMP}_{\text{dark}}$, which is equal to the dark rate of cGMP hydrolysis. This is necessary for a stable equilibrium in the dark.

Finally, the output variable of the model is ΔJ , the change in circulating current J with respect to the dark current J_{dark} . It is computed as follows:

$$\begin{aligned} J &= \frac{2}{2 + f_{\text{Ca}}} \cdot \left(\frac{\text{cGMP}}{\text{cGMP}_{\text{dark}}}\right)^{n_{\text{CG}}} \cdot J_{\text{dark}} + \frac{f_{\text{Ca}}}{f_{\text{Ca}} + 2} \cdot \frac{\text{Ca}_{\text{free}}^{2+} - \text{Ca}_0^{2+}}{\text{Ca}_{\text{dark}}^{2+} - \text{Ca}_0^{2+}} \cdot J_{\text{dark}} \\ \Delta J &= J_{\text{dark}} - J. \end{aligned} \quad (2.34)$$

In the equation for J , it can be recognized that the change in circulating current is due to two factors. The first term describes the change in cGMP concentration, closing the cyclic nucleotide gated channels. The second term describes the change in calcium concentration in the cell.

2.3.2 The Invergo 2014 model

The Invergo 2014 model (Invergo et al., 2014) is an update of the Dell’Orco 2009 model, transforming it from an amphibian to a mouse model. This is beneficial, because most of the new experimental results are available for mice and other mammalian species. The kinetic parameters of the model have been adapted to account for the faster kinetics in mammals compared to amphibians. The model mainly follows the structure of the Dell’Orco 2009 model, but a few reactions have been added or modified. These will be listed in the following. A full list of the parameters and reaction equations of the model can be found in the supplementary information of (Invergo et al., 2014).

First of all, the dependence of rhodopsin’s affinity for the rhodopsin kinase, arrestin and the G-protein is changed. For the G-protein and the rhodopsin kinase, the affinity still decreases exponentially with the number of phosphorylations, but with different coefficients ω and ω_G :

$$k_{\text{RK1},n} = \begin{cases} k_{\text{RK1},0} \cdot e^{-\omega \cdot n} & n < 6 \\ 0 & n = 6 \end{cases} \quad (2.35)$$

$$k_{\text{G1},n} = k_{\text{G1},0} \cdot e^{-\omega_G \cdot n}. \quad (2.36)$$

For the arrestin, a different dependence has proven to yield a better fit to experimental data in this model:

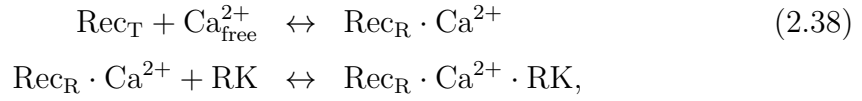
$$k_{\text{A1},n} = \begin{cases} k_{\text{Arr}} + (n - 1) \cdot m_{\text{Arr}} & n \leq 4 \\ k_{\text{Arr}} + 3 \cdot m_{\text{Arr}} & n > 4, \end{cases} \quad (2.37)$$

with parameters k_{Arr} and m_{Arr} . Rhodopsin’s affinity for arrestin now increases linearly until four phosphorylations, after which it stays constant.

The treatment of recoverin is different in the Invergo 2014 model: it is treated explicitly as a molecular species and one reaction has been added to account for

CHAPTER 2. METHODS

a more detailed description of the equilibrium between free and bound recoverin and the rhodopsin kinase.



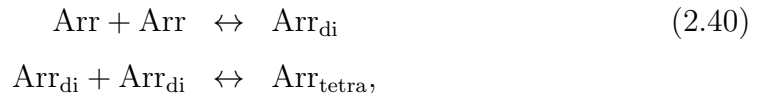
with the calcium-bound and calcium-free forms of recoverin, $\text{Rec}_R \cdot \text{Ca}^{2+}$ and Rec_T . Only the calcium-bound form of recoverin can bind the rhodopsin kinase. With these reactions, the equilibrium between free and bound rhodopsin kinase is calcium-dependent.

The formulation of the action of the GC-GCAP-system is also different. The rate for the production of cGMP is now split into the contributions from the two GCAPs influencing the GC. The two GCAPs have different effects on the GC and are active during slightly different calcium concentrations. This is resolved better using the following reaction rate:

$$v_f = \frac{\alpha_{\max}}{1 + \left(\frac{\text{Ca}_{\text{free}}^{2+}}{K_{C1}}\right)^{m_1}} + \frac{\alpha_{\max}}{1 + \left(\frac{\text{Ca}_{\text{free}}^{2+}}{K_{C2}}\right)^{m_2}}, \quad (2.39)$$

where α_{\max} is again the maximal rate of cGMP synthesis by the GCs achieved by the two GCAPs, K_{C1} and K_{C2} are the calcium concentrations at which cGMP synthesis is half-maximal resulting from the activation by the two GCAPs, and m_1 and m_2 are the Hill coefficient for the action of calcium on the cGMP synthesis rate.

There are two new effects included in the model: the formation of arrestin tetramers and precoupling. The formation of arrestin dimers and tetramers has a buffer-like function for arrestin. In the dark, some of the arrestin is bound in dimers and tetramers. As soon as the arrestin is required to shut off the response, the free arrestin gets bound to rhodopsin and more arrestin is released from the dimers and tetramers. This equilibrium is described using two new reactions:



with the arrestin dimer Arr_{di} and tetramer $\text{Arr}_{\text{tetra}}$.

The precoupling or dynamic scaffolding mechanism is described in section 1.1.5. It is included in the Invergo model with the following reactions:



The first reaction describes the precoupling of rhodopsin and transducin in the dark. In the dark, there is an equilibrium of association and dissociation resulting in 18% of the transducin being precoupled to rhodopsin. The second reaction describes the activation of the precoupled form of rhodopsin by a light stimulus with the rate

$$v_f = S \cdot \frac{R \cdot Gt}{R_{\text{tot}}}, \tag{2.42}$$

analogous to the activation of the non-precoupled rhodopsin.

2.4 Implementation in IQMtools

The modelling framework I used for the phototransduction modelling is a toolbox called *IQMtools* in MATLAB ([IQMtoolbox Website](#)). MATLAB stands for Matrix Laboratory and is a programme that can be used for various kinds of numerical calculations and data analysis. For the analyses in this thesis, I used MATLAB version R2017b unless otherwise specified. Simulations were run on a desktop computer or on the CARL high performance computing cluster¹ of the university of Oldenburg.

IQMtools is a toolbox specifically developed for modelling of biochemical and biomedical systems, which offers a vast treasure of methods ready for use. I used IQMtools version 1.2.2.2 for the analyses presented in the following.

The original Dell’Orco 2009 and Invergo 2014 models were implemented in the predecessor of IQMtools called SBTOOLBOX2 ([Schmidt and Jirstrand, 2005](#)). I converted these models as well as the simulation scripts to reproduce the figures from ([Dell’Orco et al., 2009](#)) and ([Invergo et al., 2014](#)) to the newer IQMtools syntax.

I then used the IQMmodel structure to develop the different models presented in this thesis. In the IQMmodel structure, a model is defined using either differen-

¹See <https://uol.de/en/school5/sc/high-performance-computing/hpc-facilities/carl> for the cluster’s specifications.

CHAPTER 2. METHODS

tial equations or reaction equations. The initial conditions, parameter values and additional variables are also stored in the model. Models of this structure can be combined with IQM experiments, where parameter or state values can be altered at defined points in time.

This is an excerpt from the Dell'Orco 2009 model in the IQMtools syntax:

```
***** MODEL STATE INFORMATION
R(0) = 3.6e9
PDE(0) = 1.335e7
Gt(0) = 3.6e8
...
***** MODEL PARAMETERS
Rtot = 3.6e9
PDEtot = 1.335e7
Gtot = 3.6e8
...
***** MODEL VARIABLES
E = PDE_a_Ga_GTP + 2 * Ga_GTP_a_PDE_a_Ga_GTP
J = 2/(2 + fCa)*power((cGMP/cGMPdark),ncg)*Jdark + fCa/(fCa + 2)*...
    (Ca2_free-Ca2_0)/(Ca2dark-Ca2_0)*Jdark
deltaJ = Jdark - J
...
***** MODEL REACTIONS
R => R0 : v_r1
    vf = stimulus * R/Rtot
R0 + RK <=> R0_RKpre : v_r2_0
    vf = kRK1_0 * RK * R0
    vr = kRK2 * R0_RKpre
R1 + RK <=> R1_RKpre : v_r2_1
    vf = kRK1_1 * RK * R1
    vr = kRK2 * R1_RKpre
```

First, the initial conditions for all states (i.e. explicitly simulated molecular species) are defined under **Model State Information**. The initial conditions only need to be explicitly written down when they are not zero - otherwise, zero is the default. Next, parameters are declared in **Model Parameters**. Those can be, for example, total molecule numbers for given species or the reaction rate constants. In **Model Variables**, the variables of the model are given as formulas - here for example the effector and the circulating current, or the reaction rate constants that

2.4. IMPLEMENTATION IN IQMTOOLS

depend on the phosphorylation state of rhodopsin. Finally, in **Model Reactions**, the reactions are defined in terms of their reactants and products as well as the forward and backward rates. All the parameters and variables that play into the rates need to be defined in the appropriate sections above.

After defining the model, simulations can be performed. The necessary functions for this are also supplied by the IQMtools package.

For the deterministic simulations, I used **IQMsimulate** and **IQMPsimulate**, which carry out a simulation of the given model for a specified time vector. They are based on MATLAB's own differential equation solver **ode23s**, which uses an implicit Runge-Kutta approach with adaptive step sizes. For an explanation of this method, please refer to section 2.2.3.

The difference between the two functions lies in the speed: while **IQMsimulate** carries out the simulation within MATLAB, **IQMPsimulate** first automatically converts the simulation to C, which executes more rapidly, and then translates the result back into the MATLAB environment.

For stochastic simulations, I used **IQMstochsim**, which uses a similar approach to the Gillespie algorithm as explained in section 2.2.4 by simulating the chemical Master equation.

The models can be combined with experiments to simulate specific conditions, for example stimulus paradigms or genetic modification. Below is one example for an experiment:

```
***** EXPERIMENT INITIAL PARAMETER AND STATE SETTINGS
flashBG = 100
flashMag = 900
flashDur = 0.01
flashDel = 10
```

This experiment defines a stimulus. It consists of a background of 100 (**flashBG**), which translates to 233 photons/ $\mu\text{m}^2\text{s}$ using the collecting area of $0.43\ \mu\text{m}^2$, as well as a flash. The flash starts at $t = 10\text{ s}$ (**flashDel**), lasts for 0.01 s, and has a magnitude of 2093 photons/ μm^2 (again dividing by the collecting area).

This is another possible experiment:

```
***** EXPERIMENT INITIAL PARAMETER AND STATE SETTINGS
```

CHAPTER 2. METHODS

```
RK(0) = 2e5
RecR_Ca_RK(0) = 0
RecR_Ca(0) = 0
RecT(0) = 0
***** EXPERIMENT PARAMETER CHANGES
***** EXPERIMENT STATE CHANGES
```

This experiment implements a knockout of recoverin. In a genetic knockout, the corresponding species is not produced by the animal and therefore also needs to be removed completely in the model to imitate the condition. Thus, all possible species containing recoverin are set to zero as an initial condition: the two different recoverin states with and without calcium Rec_T and $\text{Rec}_R \cdot \text{Ca}^{2+}$ as well as the calcium-bound form that also binds the rhodopsin kinase $\text{Rec}_R \cdot \text{Ca}^{2+} \cdot \text{RK}$. Since this removes some of the rhodopsin kinase from the model, the initial condition for the rhodopsin kinase has to be adapted accordingly.

Please note that it is possible to define different initial settings for parameters, variables and states using the experiment, but also parameter or state changes that occur during the simulation time, as can be seen in the lower example.

After defining the experiment, model and experiment can be combined for simulation using the command

```
model_exp = IQMmergemodexp(model, experiment);
```

An alternative way to define changed initial conditions is by using the function `IQMinitialconditions` or indeed by directly changing the initial conditions within the model, with the following alternative syntaxes:

```
model = IQMinitialconditions(model, 'R0', 1);
model.states(stateindexIQM(model, 'R0')).initialCondition = 1;
```

In both cases, `model` is modified so that the initial condition for R_0 - unphosphorylated activated rhodopsin - is one molecule. This is one option to set the initial conditions for the single photon response.

Using the models as specified earlier and the tools described here, we have all the necessary tools to perform deterministic and stochastic simulations of the photo-transduction cascade in different conditions.

3 | Deterministic modelling

In this chapter, I am explaining the new developments of the deterministic models that I carried out during my PhD. I show results from the new modelling, which are compared to current and novel experimental data.

The main deterministic model builds up on the mammalian phototransduction model from Invergo *et al.* (Invergo et al., 2014), which in turn builds on the amphibian phototransduction model developed by Dell’Orco *et al.* (Dell’Orco et al., 2009).

3.1 Rhodopsin-effector coupling

While early studies assumed that the activation of one rhodopsin molecule leads to the activation of about 100 effector molecules downstream, this has in recent years been revised to much lower effector numbers, as low as 12-14 (Yue et al., 2019).

Furthermore, the effector PDE consists of two active subunits which can each be activated by one activated α -subunit of transducin. Earlier, it was assumed that both subunits are activated independently and can each contribute half of the full activation, leading to the following formulation of the effector E :

$$E = \frac{1}{2} \text{PDE}^* + {}^*\text{PDE}^*, \quad (3.1)$$

where PDE^* is the single-activated and ${}^*\text{PDE}^*$ the double-activated PDE. This is also how the effector was implemented in the Invergo 2014 model. However, new results have demonstrated that the two subunits may have a different contribution to the effector (Qureshi et al., 2018), (Lamb et al., 2018). The new results point toward a much smaller contribution of the single-activated PDE^* : it has less than 2.5% of the catalytic activity of the double-activated ${}^*\text{PDE}^*$. We thus arrive at a new formulation of the effector:

$$E = 0.025 \cdot \text{PDE}^* + {}^*\text{PDE}^*. \quad (3.2)$$

There are two possible models that could explain this difference in catalytic activity. The first assumes that the two subunits of the PDE are identical, but not in fact independent: the first transducin that binds to the PDE can only unlock a fraction of the catalytic activity, while the second transducin can fully activate it. The second model assumes that the two binding sites for transducin are independent, but not identical. They have different catalytic activities and different affinities for transducin. The first binding site in this model has a high affinity for transducin and would typically associate to it first, but only a low catalytic activity. The second binding site has a lower affinity for transducin and would therefore usually bind to transducin later, but has a much higher catalytic activity. These two models would produce equivalent results on the level of photocurrent and could only be distinguished with a more detailed biochemical or biophysical analysis. For the purpose of our modelling, we can follow the first model.

3.1.1 Fewer activated effector molecules

First of all, I wanted to modify the model to arrive at a lower number of activated PDE molecules. My plan was to retune the parameters of the model which had been determined by parameter adaptation. In the next step, I also wanted to incorporate the new insight that the double-activated *PDE* carries most of the activity.

In the interest of keeping the model as close to experimental results as possible, my modifications to the model should obey two criteria. First, they should leave the output of the model as close to the original model as possible, in different light regimes (dim and bright flash responses, responses to prolonged stimuli and background plus flashes). Second, they should leave all parameters untouched that are sourced from experimental results. Therefore, I wanted to modify only parameters that had previously been manually tuned.

The parameters of interest are those governing the activation of the G-protein by rhodopsin and the activation of the PDE by the G-protein. In the Invergo 2014 model, all parameters describing the interaction of the G-protein and PDE were known from experimental results. However, there are a few parameter governing the activation of the G-protein by rhodopsin that had been determined by parameter tuning. These parameters are listed in table 3.1. The underlying reaction network is illustrated in figure 3.1 with all the reaction rate constants.

3.1. RHODOPSIN-EFFECTOR COUPLING

Please note that the reaction rate constant $k_{G1,n}$ for $n = 0$ to 6 phosphorylation states is calculated from the reaction rate constant $k_{G1,0}$ as follows:

$$k_{G1,n} = k_{G1,0} \cdot e^{-\omega_G \cdot n}, \quad (3.3)$$

with $\omega_G = 0.6$ from (Gibson et al., 2000). Thus, when we change $k_{G1,0}$, all other $k_{G1,n}$ are changed as well.

Table 3.1: A list of all manually tuned parameters in the activation of the G-protein by rhodopsin.

Parameter	Significance	Value
$k_{G1,0}$	Rate constant of binding of R_0 and Gt	$1 \cdot 10^{-3}/s$
k_{G2}	Rate constant of the dissociation of $R_0 \cdot Gt$ (without activation)	2200/s
k_{G3}	Rate constant of the dissociation of GDP from $R_0 \cdot Gt$	8500/s
$k_{G4,GDP}$	Rate constant of the association of GDP to $R_0 \cdot Gt$	400/s
$k_{G5,GTP}$	Rate constant of the association of GTP to $R_0 \cdot Gt$	3500/s
k_{G6}	Rate constant of the dissociation of $R_0 \cdot G_{GTP}$	8500/s

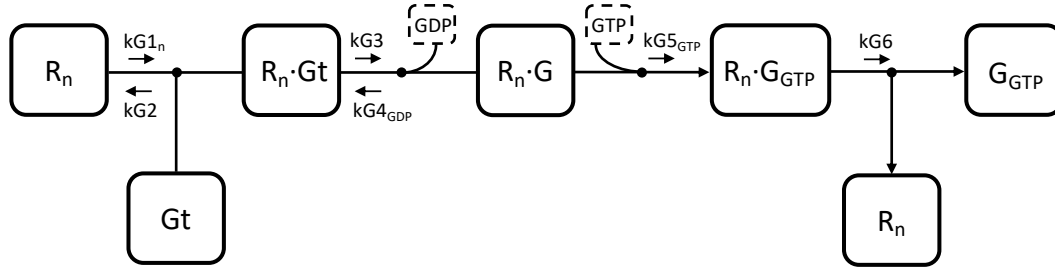


Figure 3.1: Reaction network illustrating the activation of the G-protein by rhodopsin and the reaction rate constants.

I used the parameter tuning interface of the IQM toolbox `IQMparamestGUI`, and investigated the influence of changing these parameters. The interface for manual tuning is shown in figure 3.2. In the interface, one can choose between different models to compare to experimental data. The experimental data I used for comparison was simply a simulation of the Invergo 2014 model, since this was the benchmark that I did not want to deviate from. Parameters can be changed using the sliders at the bottom of the window. The result from the simulation with the new parameters is shown as a solid line, compared with the experimental data as a dotted line.

I initially selected a dim flash response for comparison and was looking for parameter changes that would decrease the overall amount of activated G-protein, and

thus PDE, without changing the kinetics of the response in term of the change in circulating current, the *photocurrent* ΔJ , which is the output variable of the model.

I found that in k_{G3} : this parameter is the rate constant of the dissociation of GDP from $R_0 \cdot Gt$ and thus a crucial step in the phototransduction cascade. When decreasing k_{G3} , the amount of activated G-protein and PDE (and thus also ΔJ) was decreased, but the kinetics were unchanged. When scaling the responses of the modified and old model to the same amplitude, they overlapped. The same held for different types of light stimuli.

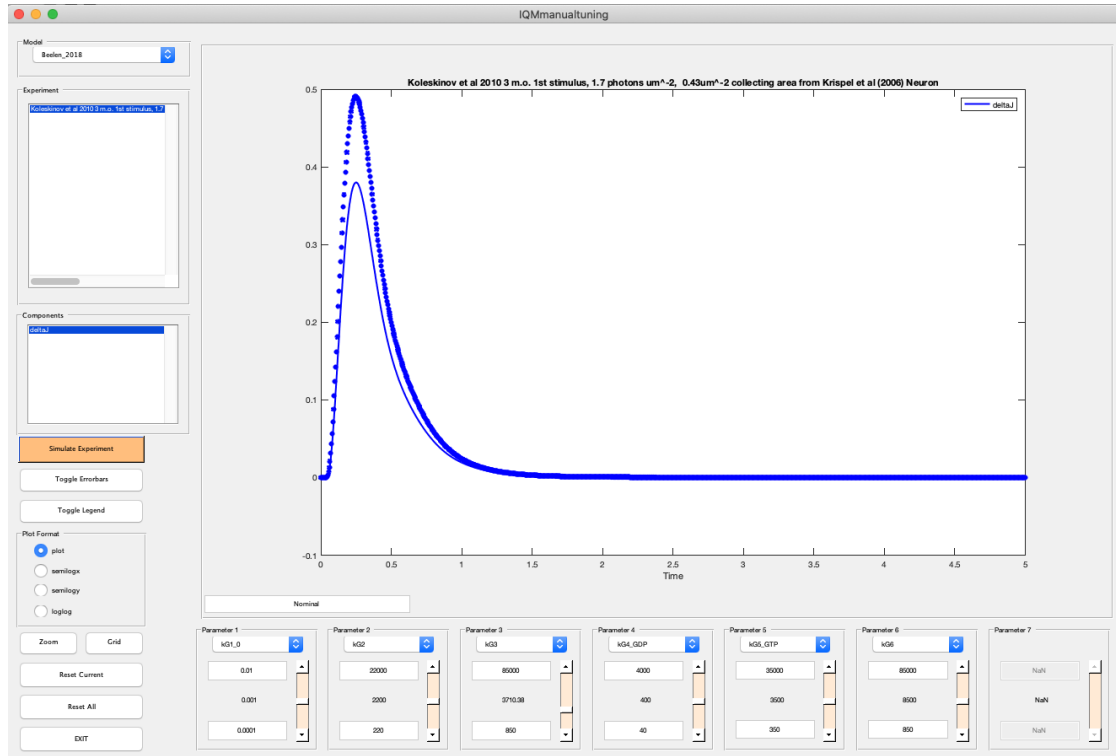


Figure 3.2: The `IQMparamestGUI` manual tuning interface. After loading a project, different models and experimental data can be selected for comparison. Parameters can be changed by moving the sliders in the lower part of the interface. After the parameters have been changed, a new simulation of the model is performed and plotted as a line along with the experimental data as a dotted line. In this case, a dim flash response is compared after the parameter k_{G3} has been changed.

When scaling k_{G3} from its original value of 8500/s down to 250/s, the peak effector during the single photon response was reduced to 13 instead of 110, as can be seen in figure 3.3 on the left: the effector resulting from a deterministic simulation of the single photon response of the Invergo 2014 (black line) and the new, modified model (red dashed line) are compared. The effector was still calculated according to the old definition here, where the total number of activated subunits are counted

regardless of whether the PDE is single- or double-activated. The new number of activated PDE subunits is now in agreement with (Yue et al., 2019).

Next, I had to make sure that enough cGMP gets hydrolyzed by this smaller amount of activated PDE, to arrive at a comparable light response in term of ΔJ . For this, I increased the catalytic activity of the effector. This is the parameter β_{sub} in the model. Increasing it from its previous value of $2.183 \cdot 10^{-3}/\text{s}$ to $0.019/\text{s}$ resulted in the normal decrease in cGMP due to the hydrolytic activity of the PDE and thus in the previous amplitude of ΔJ . This did not change the kinetics of the response.

In figure 3.3 on the right, the ΔJ resulting from deterministic simulations of the single photon response of the Invergo 2014 model (black solid line) and the new modified model (red dashed line) are compared. While the effector (left in the figure) is now at a much smaller level, the overall light response in terms of ΔJ is hardly altered.

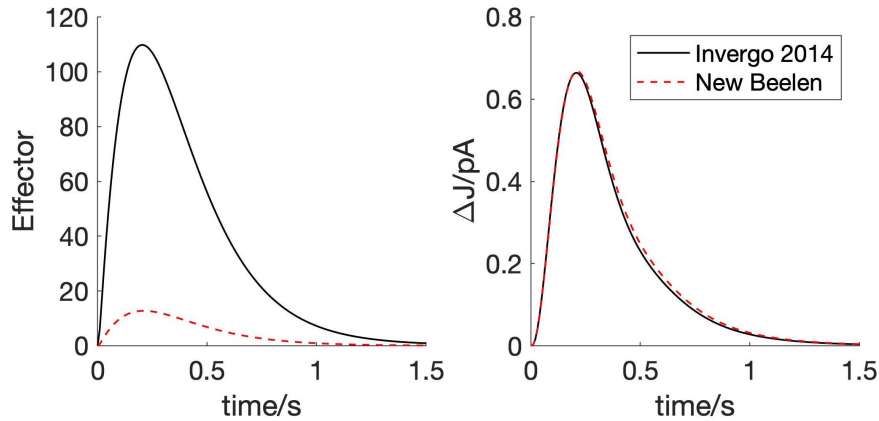


Figure 3.3: Comparison of the single photon response in the Invergo 2014 model (black solid lines) and the new deterministic model (red dashed lines). On the left, the effector is shown, and on the right, the photocurrent ΔJ is compared. The effector is calculated according to the old definition as the total number of activated subunits of the PDE.

To work with this new deterministic model, I obviously had to check that it also works well in other light regimes. To make sure of that, I compared the light responses of the Invergo 2014 model (black lines) to those of the new modified model (red lines) in figures 3.4 and 3.5. The figures shows the light responses to different stimulus paradigms: flashes of different brightness and combinations of flashes and prolonged background stimuli, for a wild type (WT) model and a simulated knockout of the GCAPs. This tests the new model's ability to produce

varied features of the light responses. The different paradigms follow (Invergo et al., 2014).

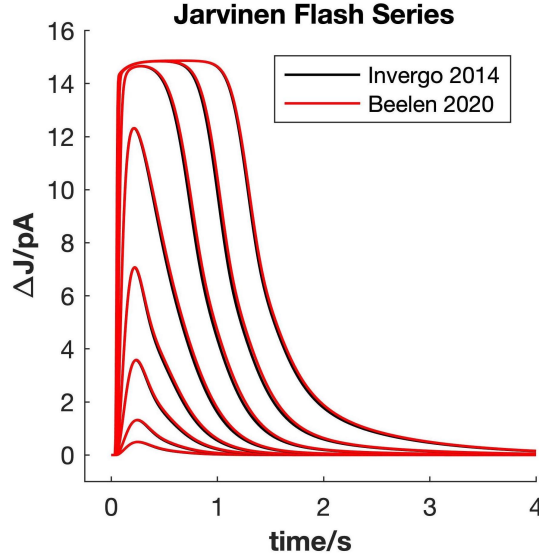


Figure 3.4: Responses of a dark adapted rod to flashes of increasing brightness compared between the Invergo 2014 model (black) and the new deterministic model (red). The flashes lasted for 0.02 s and the intensities were 1.7, 4.8, 15.2, 39.4, 125, 444, 1406 and 4630 photons/ μm^2 .

In figure 3.4, responses in terms of photocurrent ΔJ to brief flashes with increasing brightness are shown, without any background stimulus. The flashes lasted for 0.02 s and the intensities were 1.7, 4.8, 15.2, 39.4, 125, 444, 1406 and 4630 photons/ μm^2 , respectively. The new model reproduces the kinetics of the light response in this stimulus paradigm well, as the curves almost overlap.

In the three brightest flashes, we can see the phenomenon of *saturation*: the flashes are so bright that the circulating current is maximally suppressed. The higher the intensity of the flash, the longer the rod stays in this state of saturation. This is accurately reproduced in the new model.

Figure 3.5 contains the light responses in terms of ΔJ for three different stimulus paradigms, combined in one figure. The first stimulus consisted of a constant dim background stimulus (dot-dashed line). The second stimulus combined the constant background with a bright flash at $t = 100$ s (dashed line). Finally, the third stimulus just consisted of a bright flash at $t = 100$ s (solid line). The intensity of the background was 81 photons/ μm^2 s and the intensity of the flash was 1590 photons/ μm^2 .

In the left figure, we can see that the background leads to a higher ΔJ in the wild

3.1. RHODOPSIN-EFFECTOR COUPLING

type. The response to the flash is saturating, so its amplitude is not influenced by the presence of the background. The shut-off of the response to the flash is impacted, though. We can see that the modified model reproduces these effects well, despite a very slightly increased response to the background and a slightly slower recovery.

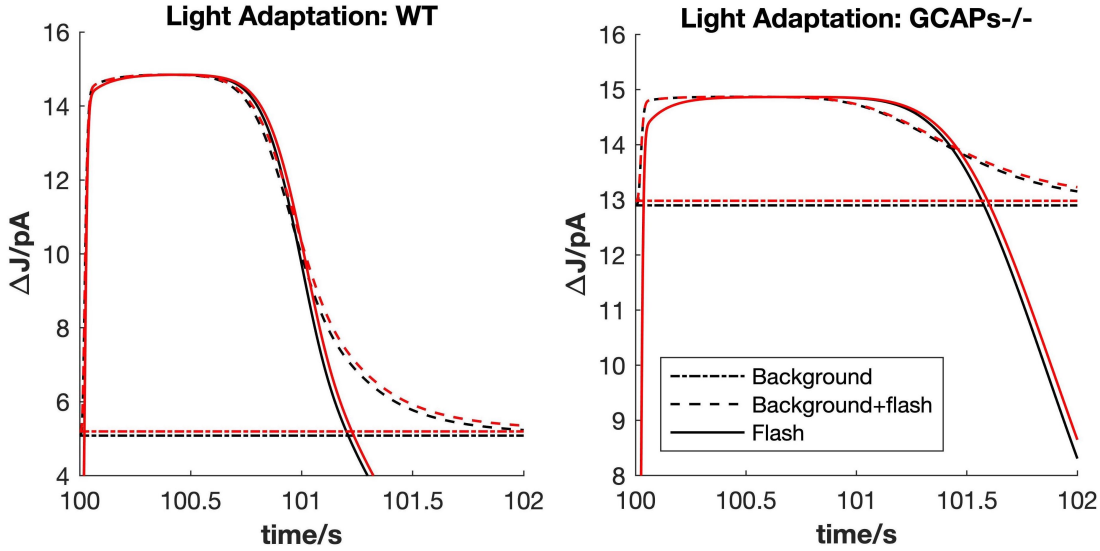


Figure 3.5: Responses to different light stimuli in a wild type model and a GCAPs knockout model, compared between the Invergo 2014 model (black) and the new deterministic model (red). In the left and right plot, the responses to three different combinations of stimuli are combined in one plot, respectively. These were: 1. a constant dim background stimulus (dot-dashed line), 2. a constant dim background stimulus and a saturating flash at $t = 100$ s (dashed line), 3. no background and a saturating flash at $t = 100$ s (solid line). In the left plot, these stimuli were applied to the wild type (WT) model, while they were applied to a GCAPs knockout model on the right.

The knockout of the GCAPs for the right plot of figure 3.5 was implemented using an experiment and modifying the synthesis rate of cGMP, which normally reads:

$$v_f = \frac{\alpha_{\max}}{1 + \left(\frac{C_{a_{\text{free}}}^{2+}}{K_{C1}}\right)^{m_1}} + \frac{\alpha_{\max}}{1 + \left(\frac{C_{a_{\text{free}}}^{2+}}{K_{C2}}\right)^{m_2}}, \quad (3.4)$$

with the following parameters: the maximal activity of the GC $\alpha_{\max} = 60 \mu\text{M/s}$ from (Koch and Stryer, 1988), the EC_{50} values $K_{C1} = 171 \text{ nM}$ and $K_{C2} = 59 \text{ nM}$, which specify the calcium concentration at which the GCAPs activate the GC to half-maximum, and the Hill coefficients $m_1 = 3$ and $m_2 = 1.5$.

When the GCAPs are knocked out, there is no calcium-dependent regulation of the GC anymore. However, this does not mean that the GC does not produce

any cGMP whatsoever - it is still producing cGMP at its basal rate. This can be determined by inserting the dark calcium concentration $\text{Ca}_{\text{dark}}^{2+} = 0.25 \mu\text{M}$ into equation (3.4), which results in a dark activity of $\alpha_{\text{dark}} = 20.72 \mu\text{M/s}$.

In the simulation, we changed the following parameters using the `IQMexperiment` syntax: set α_{max} to $\alpha_{\text{dark}} = 20.72 \mu\text{M/s}$, and set $m_1 = m_2 = 0$ to prevent any change of the activity with changing free calcium concentration.

Going back to figure 3.5, we can see that the knockout of the GCAPs has a significant impact on the different light responses. The saturating response still has the same amplitude of ΔJ , but the response to the background is a much larger change in ΔJ . Furthermore, the shut-off of the bright flash response is slower both with and without the background. These changes are due to the fact that the synthesis of cGMP to return to the dark state is not regulated in a calcium-dependent manner anymore, since the GCAPs are missing. Thus, it takes a longer time to recover from a bright flash, which has reduced the cGMP concentration. Furthermore, the adaptation to a background stimulus, which reduces the ΔJ in a prolonged stimulus, is not working anymore due to the missing calcium feedback. These effects triggered by a knockout of the GCAPs are also well reproduced in the new model.

These results demonstrate that the modified model combines the new result of a smaller number of activated effector molecules while still producing reliable and robust results in a number of different light stimulus conditions and even a knockout of the GCAPs. We can thus use it for simulations of different light conditions and different genetic modifications, as long as the specific dimeric nature of the effector does not have to be taken into account.

3.1.2 Dimeric activation of the effector

Next, I tried to include the result that the main effector is not the single-activated, but the double-activated PDE. According to (Qureshi et al., 2018), the single-activated PDE only has 2.5% of the hydrolytic activity compared to the double-activated PDE. Before, it was assumed to have 50% of the activity in the Invergo 2014 model. We thus change the formulation of the effector from

$$E = \frac{1}{2}\text{PDE}^* + {}^*\text{PDE}^* \quad (3.5)$$

3.1. RHODOPSIN-EFFECTOR COUPLING

to

$$E = 0.025 \cdot \text{PDE}^* + {}^*\text{PDE}^*. \quad (3.6)$$

In the model, this means that we change from

$$E = \text{PDE}^* \cdot G_{\alpha\text{GTP}} + G_{\alpha\text{GTP}} \cdot \text{PDE}^* \cdot G_{\alpha\text{GTP}} + 2 \cdot G_{\alpha\text{GTP}} \cdot {}^*\text{PDE}^* \cdot G_{\alpha\text{GTP}} \quad (3.7)$$

to

$$E = 0.025 \cdot \text{PDE}^* \cdot G_{\alpha\text{GTP}} + 0.025 \cdot G_{\alpha\text{GTP}} \cdot \text{PDE}^* \cdot G_{\alpha\text{GTP}} + G_{\alpha\text{GTP}} \cdot {}^*\text{PDE}^* \cdot G_{\alpha\text{GTP}}. \quad (3.8)$$

First of all, I checked how much double-activated PDE was produced in the model in general. Since we want to combine both the result that 12-14 effector-transducin complexes are activated during the single photon response and the result that the main effector is the double-activated PDE, our aim is to have a number of 12-14 activated ${}^*\text{PDE}^*$ during the single photon response.

In figure 3.6, the number of single- and double-activated PDE molecules during the single photon response is shown for the Invergo 2014 model and the new modified model. Obviously, the effector in these models is basically entirely made up of single-activated PDE molecules instead of double-activated PDE molecules. In the new model, the maximum number of ${}^*\text{PDE}^*$ lies at $1.6 \cdot 10^{-12}$ molecules, and in the Invergo model, it is at $1.2 \cdot 10^{-10}$ molecules.

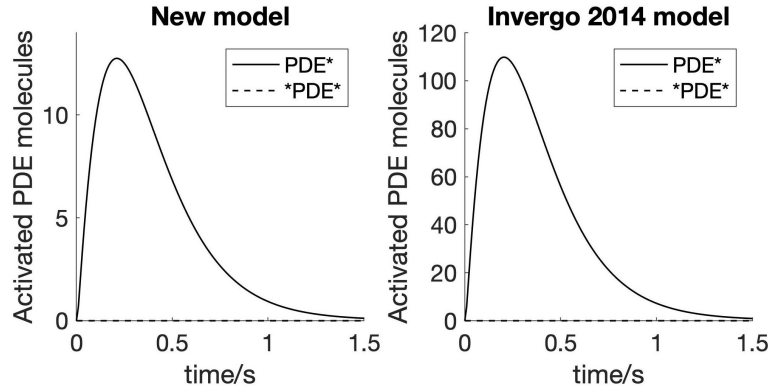


Figure 3.6: Comparison of the amount of single-activated PDE^* (solid lines) and double activated ${}^*\text{PDE}^*$ (dashed lines) for deterministically simulated single photon responses. On the left, the new modified model was used, and on the right, the Invergo 2014 model.

This is a serious problem for the modelling. In the deterministic simulations, we arrive at very low molecule numbers for the double-activated PDE - this means that, once we get to the stochastic simulations, we will not see *any* double-activated

CHAPTER 3. DETERMINISTIC MODELLING

PDE in the simulations at all, or only in 1 out of 10^{10} simulations, which is well outside any computational feasibility. To change this, parameters would need to be significantly changed in the model.

Thus, I used the parameter tuning interface and tried to achieve a higher number of double-activated PDE molecules. However, it quickly became apparent that this was impossible in the model framework as it was. Since the model simulates the entire outer segment and uses the well-stirred approximation - that all molecule concentrations are independent of space and are equal in the entire outer segment - the activated molecules are essentially spread out and diluted, leading to a low overall concentration. To get a double-activated PDE, an already activated PDE molecule would have to bind with another activated transducin. But the overall concentration of activated PDE is so low that this reaction has a very low rate, since according to mass-action kinetics, the rate is proportional to the concentration of single-activated PDE and activated transducin.

How to fix this issue? The most obvious answer would be to switch from this well-stirred model to a space-resolved model. However, this would require inputting many additional parameters about spatial diffusion of all the molecules involved in phototransduction. Space-resolved models of phototransduction do exist ([Schöneberg et al., 2014](#)), ([Dell’Orco and Schmidt, 2008](#)), ([Felber et al., 1996](#)), ([Lamb and Kraft, 2020](#)), but they usually only simulate the very first steps or a reduced number of interactions of the phototransduction cascade due to a lack of information about the remaining steps and due to limited computational power. Thus, we decided not to go this route, but to go for a compromise that would allow both the in-detail modelling that we are interested in, as well as a better agreement with the new results about the dimeric activation of the PDE.

My idea was to scale down the model to a smaller volume, that would still contain the number of proteins necessary for the cascade but that would be small enough not to water down the concentration of the activated molecules, making more double-activated PDE possible. However, this would only work for part of the cascade, where the effects of the phototransduction cascade are constrained to, say, one disc membrane - and thus not for the second messengers. Furthermore, the brighter the stimuli, the higher the chance of getting a shortage of molecules resulting from the smaller volume. Therefore, this type of modelling was applied only for dim light stimuli and specifically for the stochastic modelling. More information on the resulting small model can be found in section [4.3](#). As explained

there, I was successful in creating a model for dim light stimuli that reproduces both the result that the main effector is the double-activated PDE, and that 12-14 *PDE* are activated during the single photon response.

The final deterministic model I am working with for bright stimuli is thus the modified model from earlier, where the effector had been scaled to a smaller number, but that does not contain the dimeric activation of the PDE. The effector definition is $E = \text{PDE}^* + 2 \cdot *PDE^*$ and the main contribution comes from the single-activated PDE. The model is also referred to as the Beelen 2020 model in the following. The parameter changes in the model with respect to the Invergo 2014 model can be found in the appendix in table [A.13](#).

3.2 Light adaptation

The phenomenon of light adaptation occurs after a prolonged background stimulus: the light responses become different from those without any background. One of the more prominent effects of light adaptation is that the time spent in saturation after a saturating flash is reduced when the rod has previously been exposed to a background stimulus. This can already be seen in figure [3.5](#). It is more obvious in figure [3.7](#).

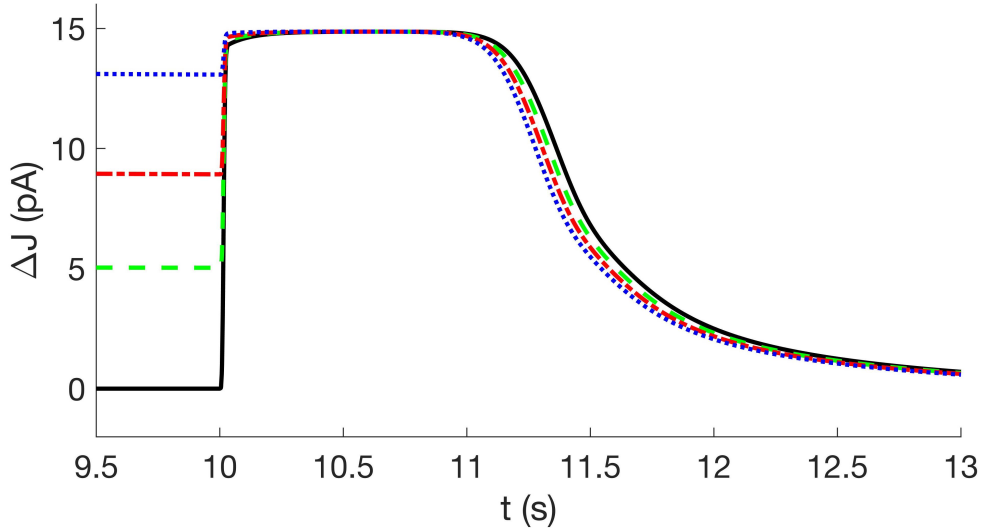


Figure 3.7: Responses to a stimulus consisting of a background lasting for 10s and a saturating flash at $t = 10$ s. The brightness of the backgrounds was: 0 photons/ $\mu\text{m}^2\text{s}$ (solid black line), 698 photons/ $\mu\text{m}^2\text{s}$ (dashed green line), 1860 photons/ $\mu\text{m}^2\text{s}$ (dot-dashed red line), and 4651 photons/ $\mu\text{m}^2\text{s}$ (dotted blue line). The saturating flash had a brightness of 6968 photons/ μm^2 .

In the figure, the light response to a stimulus consisting of a background lasting for 10 s and a saturating flash at $t = 10$ s is shown. The four different background intensities lie between 0 photons/ $\mu\text{m}^2\text{s}$ to 4651 photons/ $\mu\text{m}^2\text{s}$. After the saturating flash, the circulating current returns to the dark level, since the background stimulus has ended. The larger the background intensity was before the saturating flash, the shorter the time spent in saturation after the flash.

An important mechanism for light adaptation, next to the action of the GC-GCAPs system, is the feedback of calcium on recoverin and the rhodopsin kinase, which regulates the shut-off of the cascade. It is illustrated in figure 3.8. This mechanism regulates the availability of the rhodopsin kinase to phosphorylate rhodopsin, which is an essential part of the shut-off of the activated rhodopsin: the phosphorylation leads to a decreased affinity for the G-protein, and allows binding to arrestin, which completely shuts off rhodopsin.

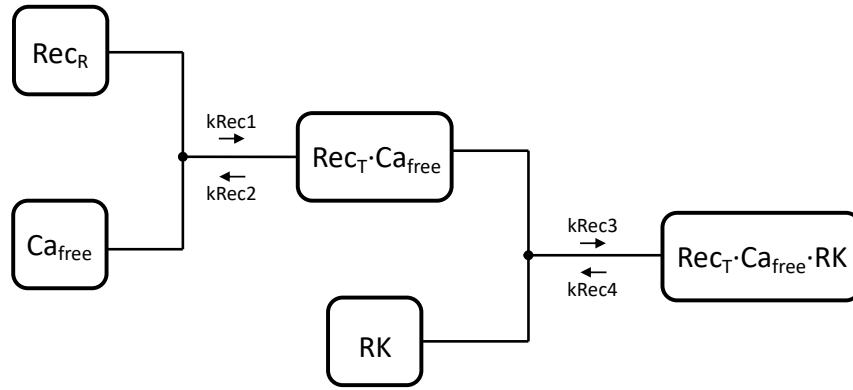


Figure 3.8: The calcium-dependent regulation of the rhodopsin kinase by recoverin. Recoverin can associate and dissociate to free calcium with rate constants k_{Rec1} and k_{Rec2} . The calcium-bound form can then associate and dissociate to the rhodopsin kinase with rate constants k_{Rec3} and k_{Rec4} .

In the dark state, most of the rhodopsin kinase is unable to interact with rhodopsin, because it is bound to the calcium-bound form of recoverin. As a consequence of the light response, the calcium concentration in the cell drops, which leads to the recoverin losing its calcium ions. This triggers a conformational change in the recoverin and releases the rhodopsin kinase, which can then phosphorylate rhodopsin.

The role of the phosphorylation for the shut-off of rhodopsin is undisputed, but the role of the calcium-dependent regulation in light adaptation is unclear. Using the model, we can investigate the relevance of this mechanism for light adaptation

in more detail.

To study the significance of the recoverin-rhodopsin kinase mediated calcium feedback for light adaptation, I removed the feedback from the Beelen 2020 model and looked at light responses in the resulting modified model. The amounts of recoverin in the calcium-bound and calcium-free state were set to fixed values, which led to the reaction scheme in figure 3.9. The rhodopsin kinase could now be consumed and produced with the following rates:

$$\begin{aligned} v_f &= k_{\text{Rec3}} * \text{Rec}_R \cdot \text{Ca}^{2+} * \text{RK} \\ v_r &= k_{\text{Rec4}} * \text{Rec}_R \cdot \text{Ca}^{2+} \cdot \text{RK}, \end{aligned} \quad (3.9)$$

where the molecular species $\text{Rec}_R \cdot \text{Ca}^{2+}$ and $\text{Rec}_R \cdot \text{Ca}^{2+} \cdot \text{RK}$ were fixed to their dark concentrations and are therefore not calcium-dependent anymore. The reaction rates are therefore fixed (v_f , the rate of the production of rhodopsin kinase) or only dependent on the free concentration of rhodopsin kinase (v_r , the rate of the consumption of rhodopsin kinase).

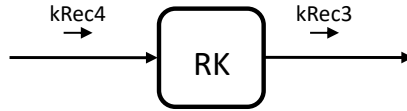


Figure 3.9: The calcium-independent regulation of the rhodopsin kinase. The different forms of recoverin are set to constant values which are part of the reaction rates.

I first checked whether there would be any effect of this change on flashes of different intensities without any background. This comparison is shown in figure 3.10. The responses of the two models overlap exactly - thus, there is no effect of the removal of the calcium feedback on recoverin and the rhodopsin kinase for dim to saturating flashes without any background.

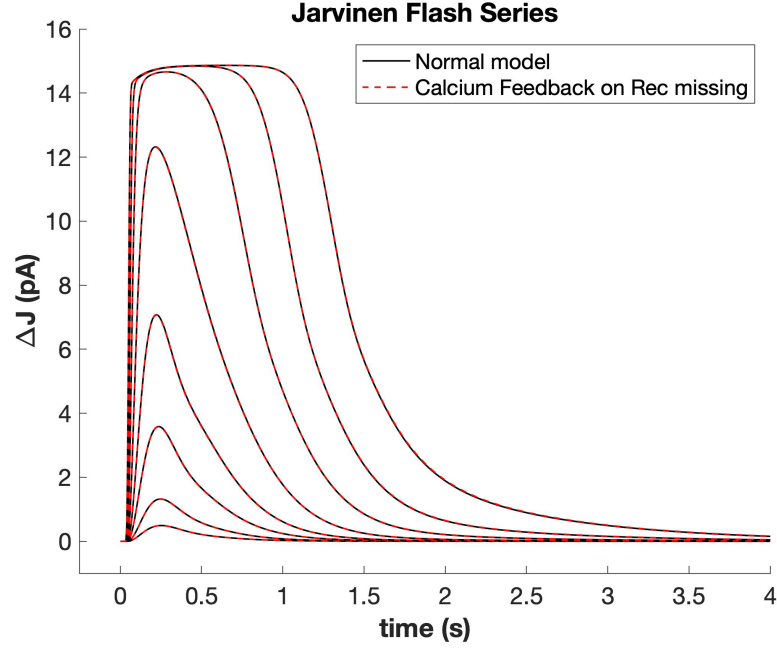


Figure 3.10: Comparison of the normal model (solid black lines) to the model with no calcium feedback on the regulation of the rhodopsin kinase (dashed red lines). The stimulus consisted of flashes of increasing brightness (1.7, 4.8, 15.2, 39.4, 125, 444, 1406 and 4630 photons/ μm^2) without any background.

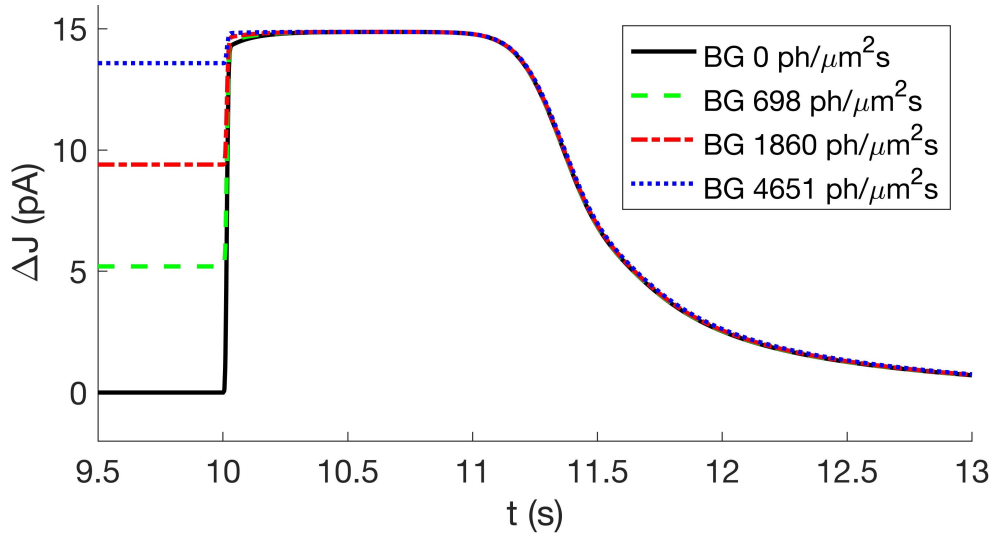


Figure 3.11: Responses in the model without calcium feedback on the rhodopsin kinase to a stimulus consisting of a background lasting for 10 s and a saturating flash at $t = 10$ s. The brightness of the backgrounds was: 0 photons/ $\mu\text{m}^2\text{s}$ (solid black line), 698 photons/ $\mu\text{m}^2\text{s}$ (dashed green line), 1860 photons/ $\mu\text{m}^2\text{s}$ (dot-dashed red line), and 4651 photons/ $\mu\text{m}^2\text{s}$ (dotted blue line). The saturating flash had a brightness of 6968 photons/ μm^2 .

However, when checking the effect on flashes with a background, it became obvious

that there is an effect of the feedback. In figure 3.11, the same stimulus paradigm from figure 3.7 was repeated for the model without calcium feedback. The acceleration of the recovery phase, a typical feature of light adaptation to background illumination, is lost in the absence of a calcium feedback.

I also calculated the saturation time, which is the time spent over 90% of the maximum amplitude, for saturating flashes after adaptation to backgrounds of different intensities. The comparison of the saturation times can be found in figure 3.12. In the model describing the wild type, there is a clear decrease of saturation time with increasing background intensity. When the calcium feedback is removed, the time spent in saturation even increases slightly with increasing background intensity.

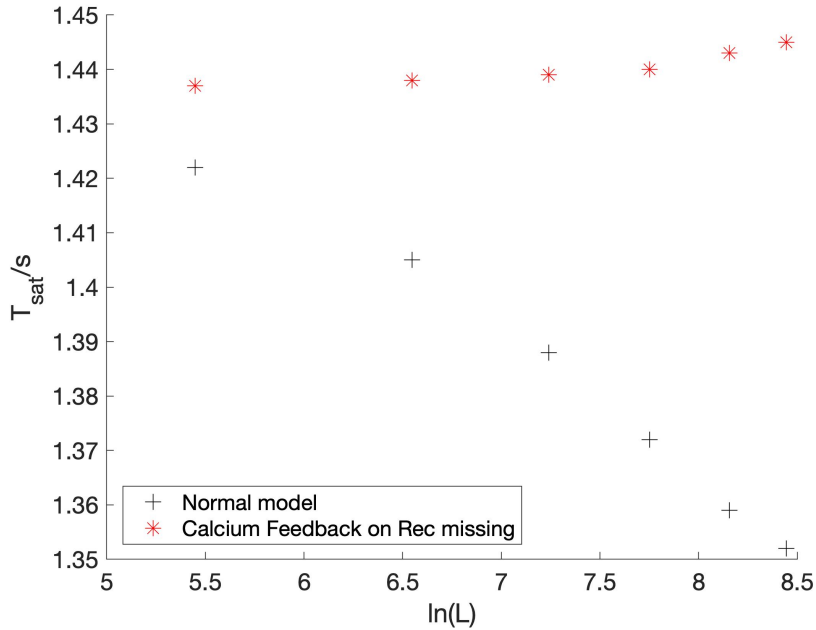


Figure 3.12: The time spent in saturation (over 90% of the maximum ΔJ) after adaptation to backgrounds of different intensities L and a saturating flash, plotted over $\ln(L)$. Black plus signs are for the normal model, while red asterisks are for the model where the calcium feedback on recoverin and the rhodopsin kinase was removed.

To conclude, for the kind of light stimuli presented here, the calcium-mediated feedback on recoverin and the rhodopsin kinase is essential for light adaptation in the model. In the model describing the wild type, the recoverin releases rhodopsin kinase as a response to the decrease in calcium concentration triggered by the background stimulus. This free rhodopsin kinase is then ready to rapidly phos-

phorylate rhodopsin activated by the saturating flash, shutting off the response more quickly than without the background.

In the altered model without the feedback mechanism, production and consumption of the rhodopsin kinase are in equilibrium in the dark. As a response to a stimulus, the free rhodopsin kinase can associate to rhodopsin, decreasing the amount of free rhodopsin kinase. This decreases the rate of consumption of the free rhodopsin kinase in equation (3.9). However, there is no increased production of free rhodopsin kinase due to a change in calcium concentration. Thus, the additional release of rhodopsin kinase by this mechanism is not sufficient for any decrease of the time spent in saturation.

3.3 Comparison to novel electrophysiological data

Together with our collaborators Sabrina Asteriti and Lorenzo Cangiano from the university of Pisa, we came up with some stimulus paradigms to compare to our simulation data as a test of our model. The results for dim light stimuli are shown and evaluated in section 4.4. Here, I am presenting the stimulus paradigm for bright light responses and light adaptation.

Since we wanted to test responses to flashes with and without backgrounds, we combined a series of five flashes of increasing brightness with four different backgrounds intensities, one of which was zero.

The responses were recorded using an electrophysiological method called *loose seal recording*. The responses are measured in terms of the photovoltage ΔU , the change in membrane potential. In the loose seal method, an electrode is approached to a rod cell within a whole retina mount, but it does not pierce the cell wall (this is in contrast to regular electrophysiological recordings).

As a consequence, there is no leakage of ions or electrons into the electrode and recordings are stable for a much longer time than in traditional electrophysiology. However, absolute values of the recorded membrane potential are meaningless, since they depend on the contact made with the cell - only relative values can be evaluated.

The response to the above mentioned stimulus paradigm is plotted in figure 3.13. The recordings have been lowpass-filtered using MATLAB's function `lowpass`¹ with a passband frequency of 40 Hz and averaged with a sliding window of 20 ms

¹Since the function `lowpass` was only introduced in MATLAB R2018a, this step was done in a newer MATLAB version, R2019b. The rest of the evaluation was done in MATLAB R2017b.

3.3. COMPARISON TO NOVEL ELECTROPHYSIOLOGICAL DATA

using the function `movmean` to remove a 50 Hz oscillation.

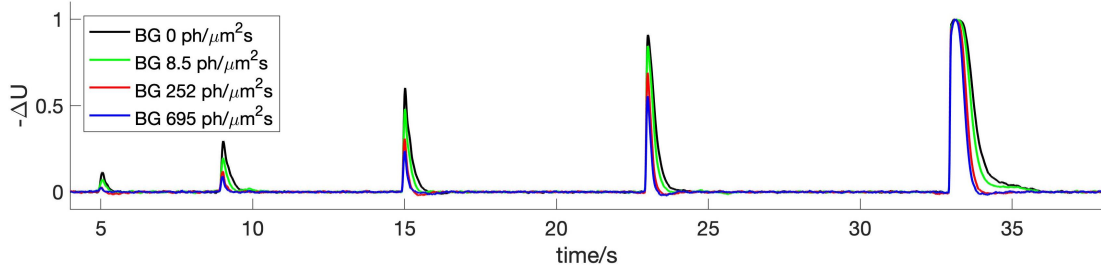
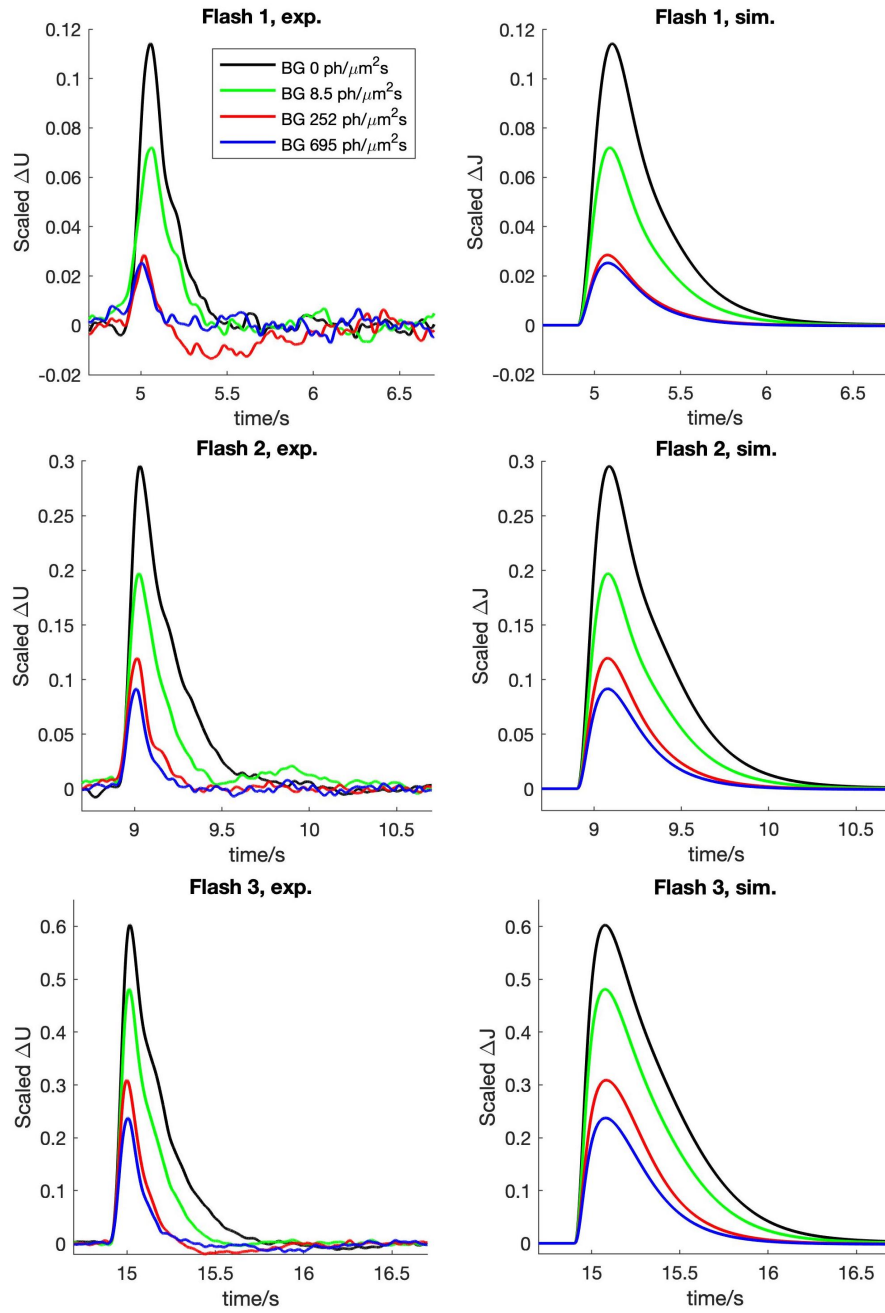


Figure 3.13: Electrophysiological recordings of the new stimulus paradigm consisting of a fixed background and five flashes of increasing intensity. The intensity of the backgrounds was 0 photons/ $\mu\text{m}^2\text{s}$ (black), 8.5 photons/ $\mu\text{m}^2\text{s}$ (green), 252 photons/ $\mu\text{m}^2\text{s}$ (red), and 695 photons/ $\mu\text{m}^2\text{s}$ (blue). The intensities of the flashes was 9.5 photons/ μm^2 , 32.1 photons/ μm^2 , 96.4 photons/ μm^2 , 299 photons/ μm^2 , and 5104 photons/ μm^2 . The responses were shifted to the same resting membrane potential of zero and normalized to the saturating response.

To compare this electrophysiological recording to simulated light responses, we first had to adapt the model to the respective backgrounds. To do this, I applied a steady background illumination by modifying `flashBG` using an experiment. After simulating for 100 seconds, the model had reached a steady state. I saved the current values for all molecular species as initial conditions for a new model, `modeladapt`, by modifying `modeladapt.initialCondition`. This model represents the normal Beelen 2020 model which has been adapted to the given background illumination. I did this for each of the 4 background intensities.

Next, I applied the different flashes to the adapted models by modifying `flashMag` and `flashDur` according to the stimulus paradigm. I simulated the responses to the flashes one by one, for each combination of background and flash intensity. When setting the intensity for the experiments in the simulations, we had to scale the intensities with respect to the intensities given in the experiment: in the experiment, there is a distance between the light source and the retina and there is some retinal tissue the light has to traverse to reach the rods. By comparing the light responses (especially the fact that the fifth flash is saturating, and the fourth not yet), I arrived at a scaling factor of 0.4 for all intensities given in the experimental description. The dimmest background (intensity 8.5 photons/ $\mu\text{m}^2\text{s}$) was further scaled with a factor of 3. This is due to the fact that the LED used for the experiments has a nonlinear behaviour at low light intensities, possibly outputting larger intensities than desired at low intensities.

We can then compare the result of the simulations with the electrophysiological recordings. The flashes are shown side by side in figure 3.14: on the left, the experimental flashes are shown in ΔU , and on the right, the simulated flashes are shown in ΔJ . The amplitude of the simulated responses was scaled to the amplitudes of the electrophysiological amplitudes, and the resting photocurrent was subtracted to baseline the simulated data like the experimental data.



3.3. COMPARISON TO NOVEL ELECTROPHYSIOLOGICAL DATA

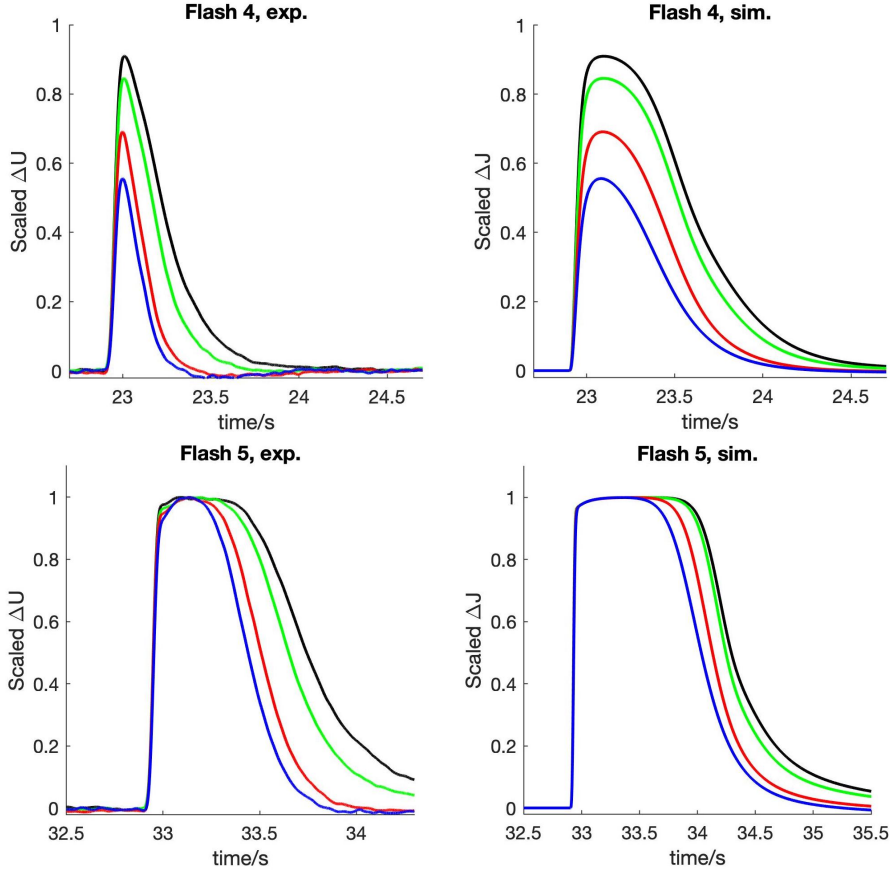


Figure 3.14: Responses to the bright flash + background paradigm separated by flashes. The experimental data in photovoltage ΔU are on the left and the simulated responses in ΔJ are on the right. The simulated responses have been normalized to the same amplitudes as the experimental recordings.

When comparing the responses side by side, it becomes noticeable that the simulated responses are slower in terms of the shut-off - this is especially obvious for the brighter flash responses. The responses are also slightly slower in the excitatory phase. However, the general kinetics are reproduced: the brighter the flashes, the longer the response, and the brighter the background, the faster the shut-off.

To compare the experimental data and the simulated responses more quantitatively, we calculated the time spent over half the maximal amplitude, T_{half} , for the simulated and experimental responses. This measure is more stable than the saturation time, which is the time spent in more than 90% of the maximal amplitude, when we are treating non-saturating flashes. Specifically, we compared the reduction of T_{half} for each background, relative to the response without any background. The comparison is shown in figure 3.15.

In this comparison, we can also see that the simulated flash responses are longer,

and that the reduction resulting from the backgrounds is less than in the experimental data. But the general trend of the reduction in T_{half} by the adaptation to the backgrounds is well reproduced.

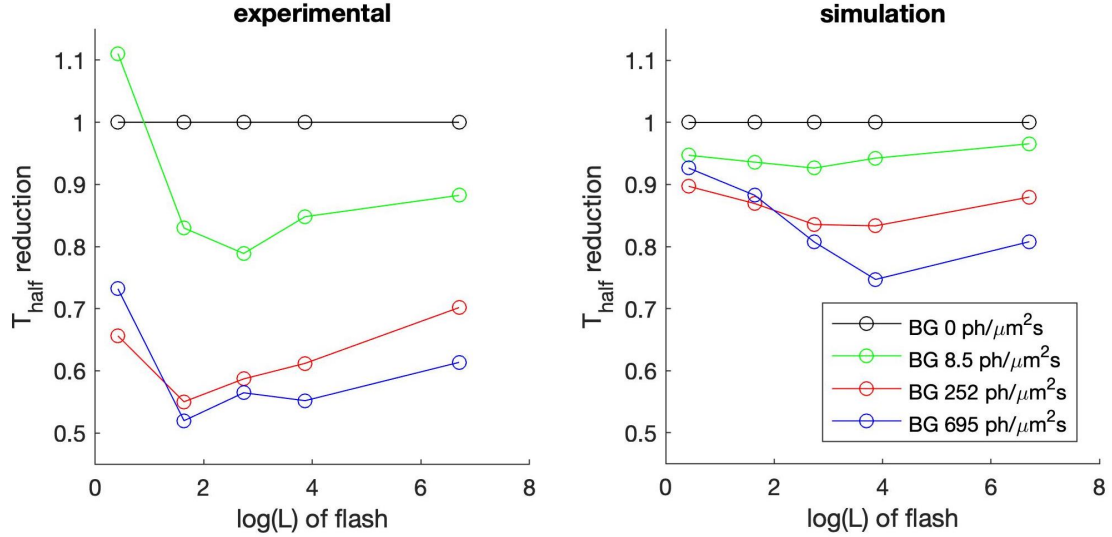


Figure 3.15: Comparison of the reduction in the time spent over half the maximal response amplitude, T_{half} , for each background with respect to zero background, for the experimental data (left) and the simulated data (right). The background intensities were 0 photons/ $\mu\text{m}^2\text{s}$ (black), 8.5 photons/ $\mu\text{m}^2\text{s}$ (green), 252 photons/ $\mu\text{m}^2\text{s}$ (red), and 695 photons/ $\mu\text{m}^2\text{s}$ (blue).

Where do the differences in response kinetics arise from? There are several possibilities for this. They could arise because some shut-off mechanism responsible for light adaptation is missing in the model. Furthermore, the discrepancy could be because we are comparing the photovoltage ΔU to the photocurrent ΔJ . In principle it is possible to back-convert ΔU to ΔJ by measuring and using the complex impedance of the rod. We do this in section 4.4 for the dim light responses. However, this conversion is not as precise for brighter light responses and we therefore decided against using it in this case. The reasons for the observed discrepancies are further discussed in chapter 5.

In summary, the simulated light responses reproduce the general qualitative features of the responses and the light adaptation. However, when comparing them more quantitatively, we noticed that the simulated responses have a slower shut-off.

3.4 Calcium feedback on the effector

In recent years, there have been an number of studies that investigated the shut-off of light responses in rods in different knockout conditions, whose results apparently could not be explained in the current mechanistic understanding of the phototransduction cascade. The central hypothesis is that there must be an additional regulation of the shut-off of the effector.

A major part of the results comes from light responses from rods with an overexpression of the rhodopsin kinase and a knockout of recoverin. It was observed that an overexpression of the rhodopsin kinase leads to similar results to the knockout of recoverin, namely an increase in the phosphorylation of rhodopsin and a subsequent decrease in the time constants τ_{Rec} and τ_{D} . τ_{Rec} is the time constant of recovery, which is determined by fitting an exponential decay function to light responses of a small amplitude - a decrease in τ_{Rec} thus means that the recovery is faster. The corresponding electrophysiological traces can be found in figure 3.16.

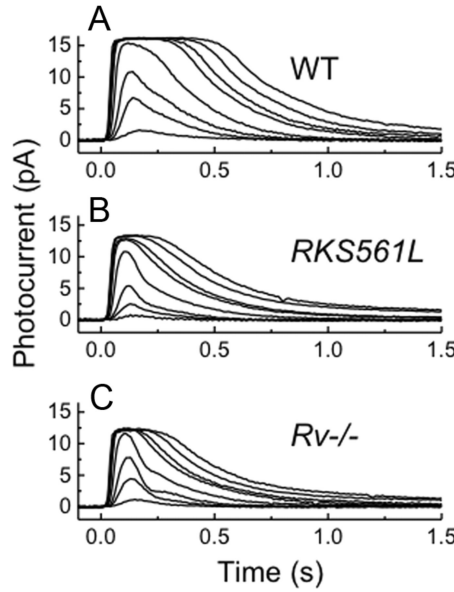


Figure 3.16: Electrophysiological recordings of light responses mouse rods compared between the wild type (WT, panel A), an overexpression of the rhodopsin kinase (RKS561L, panel B), and a knockout of recoverin (Rv-/-, panel C). Reprinted according to guidelines of The Journal of Neuroscience from (Chen et al., 2012).

τ_{D} is the Pepperberg constant, which is determined from the time T_{sat} spent in saturation after a saturating flash. The slope of T_{sat} over the logarithm of the intensity of the flash is τ_{D} . The higher τ_{D} , the larger is the change of the time spent in saturation with increasing flash intensity.

The authors concluded from these results that, since the rate-limiting step in the

CHAPTER 3. DETERMINISTIC MODELLING

decay of the response is the shut-off of PDE, there must be a change in this step resulting from the genetic modifications. Thus, the rhodopsin kinase and recoverin are hypothesized to regulate the shut-off of PDE. This also connects the shut-off of PDE to calcium in a feedback mechanism, since the recoverin regulates the rhodopsin kinase in a calcium-dependent manner. (Chen et al., 2012)

Furthermore, recoverin knockout mice were investigated in light adaptation settings. It was found that light adaptation - in this case the slow decrease of ΔJ with a steady background - is not present in recoverin knockout rods. Again, it was concluded that the PDE must be somehow regulated by recoverin. (Morshedian et al., 2018)

For further studies with similar conclusions, please see (Chen et al., 2015), (Tsang et al., 2007) and (Woodruff et al., 2008).

In summary, there is some indirect evidence pointing towards a regulation of the PDE by the rhodopsin kinase or by recoverin, introducing a calcium feedback on the shut-off of the effector. To check the validity of the conclusions drawn by the authors, I wanted to investigate the results using the model. The model does not include any interaction of the PDE with recoverin or the rhodopsin kinase, or indeed any calcium feedback *directly* on the effector.

However, there is a calcium feedback on rhodopsin, mediated by recoverin on the rhodopsin kinase. In section 3.2, we have already found that this feedback mechanism is responsible for light adaptation phenomena in the model, and that no feedback on the level of the effector is necessary for light adaptation. Thus, the results from (Morshedian et al., 2018) can be explained in our model without any additional feedback on the effector: The knockout of the recoverin means that the calcium feedback on *rhodopsin* is missing, and this explains the lack of light adaptation.

I also investigated the consequences of a 12-fold overexpression of the rhodopsin kinase and a knockout of recoverin as in (Chen et al., 2012). I implemented a knockout of the recoverin and the overexpression of the rhodopsin kinase using the `IQMexperiment` function. The model used for the simulations is the Invergo 2014 model. In figure 3.17, I show the results of simulations of flashes of different intensities on a dark-adapted rod, for the normal model (WT) as well as a 12-fold overexpression of the rhodopsin kinase (analogous to the publication) and a knockout of recoverin.

3.4. CALCIUM FEEDBACK ON THE EFFECTOR

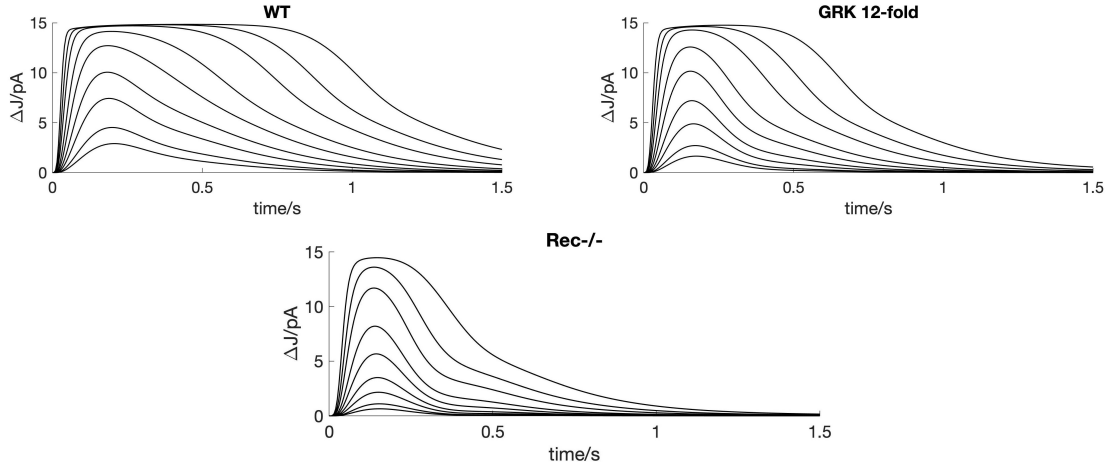


Figure 3.17: Responses to flashes of increasing brightness on a dark-adapted rod, for the wild type model (upper left), a 12-fold overexpression of the rhodopsin kinase (upper right), and a knockout of the recoverin (lower panel).

Comparing the responses to flashes of increasing amplitudes on a dark-adapted rod, we can observe a speed-up of the recovery for the overexpression of the rhodopsin kinase and the knockout of recoverin compared to the wild type model. This is very similar to the observation in figure 3.16. It also means that τ_{Rec} is reduced. However, this is explained entirely by the regulation of rhodopsin by the rhodopsin kinase and the recoverin in the model, since there is no additional feedback mechanism on the PDE present. Thus, we again observe that no additional mechanism is required to explain the observations.

We can also recreate the observations concerning light adaptation by simulating light responses to saturating flashes and measuring T_{sat} , the time spent in saturation. The Pepperberg plot of T_{sat} , calculated here as the time spent over 90% of the maximal amplitude, over the logarithm of the intensity is shown in figure 3.18.

As shown in the figure, the time spent in saturation is lower for both the knockout of recoverin and the overexpression of the rhodopsin kinase. This is due to the fact that, in both cases, more rhodopsin kinase is available to phosphorylate rhodopsin and shut-off the response more quickly: this is the case for the overexpression of the rhodopsin kinase, and for the recoverin knockout as well, as none of the rhodopsin kinase is bound in an inactive state by recoverin. Furthermore, we can observe that τ_{D} is reduced from 0.24 for the wild type to 0.20 for both the recoverin knockout and the rhodopsin kinase overexpression.

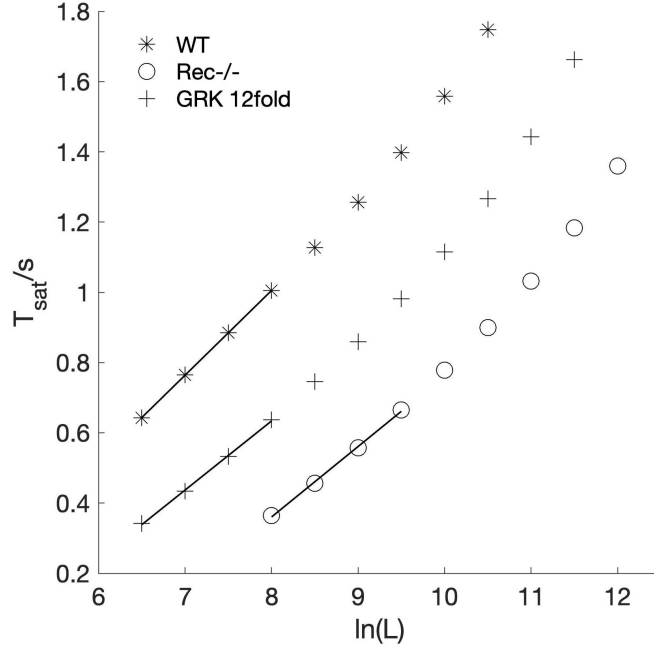


Figure 3.18: Pepperberg plot showing the time T_{sat} spent in saturation (over 90 % of the maximal amplitude) over the logarithm of the light intensity of the flash. The intensity is measured in photons/ μm^2 . The lines indicate a linear fit, whose slope is τ_D . Asterisks correspond to wild type results, circles correspond to the knockout of recoverin, and plus signs correspond to the 12-fold overexpression of the rhodopsin kinase.

Compared to the results presented in (Chen et al., 2012), this is qualitatively quite similar. The traces for the recoverin knockout and the rhodopsin kinase overexpression superimpose in the publication, but this is not reproduced in our model. Still, we can reproduce the fact that τ_D is equally reduced for both mutations. This indicates that a calcium feedback via recoverin and the rhodopsin kinase on the PDE is not necessary for this effect. The calcium feedback via recoverin and the rhodopsin kinase on the deactivation of rhodopsin is sufficient to qualitatively reproduce the observations of (Chen et al., 2012).

For all the different observations presented here, we could reproduce the different effects without the need for an additional feedback of calcium on the effector. Thus, we conclude that the proposed feedback mechanism on the PDE is not necessary and cannot be postulated from the results concerning the knockout of recoverin and the overexpression of the rhodopsin kinase.

3.5 Disease modelling

Using the model, we can also investigate the consequences of diseases which correlate with mutations in proteins of the phototransduction cascade. If we know the consequences of a point mutation on the kinetics and the interactions of the species involved in phototransduction, we can include this information into the modelling and investigate the consequences on light responses. This has already been done successfully for e.g. a model of the knockout of retinal pigment epithelium 65, a model for Leber congenital amaurosis and vitamin A deprivation (Dell’Orco and Koch, 2010), and a model of cone/rod dystrophies (Dell’Orco and Dal Cortivo, 2019).

Specifically, we wanted to investigate the molecular basis of retinitis pigmentosa and congenital stationary night blindness. Both diseases are caused by mutations in rhodopsin. Retinitis pigmentosa (RP) is a degenerative disease of the photoreceptors, leading to the dysfunction of rod cells. This causes cell death of the rods, as well as dysfunction and subsequent death of the cone cells. In patients, the first symptoms are impaired dark adaptation and night blindness, as rods degenerate. Since the degeneration starts from the rod-rich periphery, leaving intact cone cells in the fovea, patients then develop tunnel vision. However, with the progression of the disease, cone cells degenerate as well leading to blindness. Since no cure is known to date, the disease has a strong impact on patients’ physical and mental wellbeing.

Congenital stationary night blindness (CSNB) is similar to retinitis pigmentosa, but less severe. This disease is characterized by a loss of function of the rods alone and is not progressive. The cones are not affected by this, so patients lose their ability to see in dim light conditions, the so-called *scotopic vision*, but are still able to see in bright light conditions.

In the review (Athanasίου et al., 2018), rhodopsin mutations causing retinitis pigmentosa or congenital stationary night blindness are categorized into eight categories, which are listed in table 3.2. Please note that the categorization refers to the autosomal dominant forms of RP and CSNB, which are more common and better studied. These forms have a normal and a mutated copy of the rhodopsin gene.

CHAPTER 3. DETERMINISTIC MODELLING

Table 3.2: Categories for rhodopsin mutations causing RP or CSNB.

Category	Features
1	Disrupted trafficking to OS
2	Misfolding
3	Disrupted vesicular trafficking
4	Altered post-translational modifications
5	Altered transducin activation
6	Constitutive activation
7	Dimerization deficiency
Unclassified	Unknown biochemical or cellular mechanism

To understand the first four categories, let us focus on the synthesis of rhodopsin in the rod cell. Rhodopsin is constantly produced to renew old proteins. This production takes place in the endoplasmic reticulum, the protein factory of the cell. First, *translation* takes place: the messenger RNA from the nucleus is translated into a sequence of amino acids, forming the protein. Next, the protein is folded correctly and posttranslational modifications take place. In this step, the folding can go wrong due to a point mutation in the protein sequence. This leads to an altered secondary and tertiary structure of the rhodopsin. Those mutations are included in category **2**. The consequences of misfolding can be, for example, that the rhodopsin does not leave the endoplasmic reticulum to be transported to the outer segment, due to the quality control of the cell. This causes stress in the endoplasmis reticulum and can cause cell death.

Mutations can also disrupt the post-translational modifications, leading to an impaired stability or function of the rhodopsin. These mutations fall into category **4**. The consequences can be protein aggregation of the mutant rhodopsin or a decreased stability causing protein degeneration upon exposure to light.

After the synthesis of the rhodopsin, it is loaded into vesicles and transported to the outer segment, where it can fulfill its task in the phototransduction cascade. However, there are mutations that affect the formation of these vesicles or the trafficking to the outer segment. These fall into categories **3** and **1**. They lead to an unwanted accumulation of rhodopsin in wrong places in the cell, for example the inner segment. This can cause stress to the cell.

Categories **5** and **6** refer to the role of rhodopsin in the phototransduction cascade. The mutations in category **5** lead to an altered transducin activation. This means that the activation rate of transducin by light-activated rhodopsin is significantly changed. In category **6**, the interaction with transducin is also influenced: these mutants are constitutively active, which means that the transducin is constantly being activated regardless of whether rhodopsin is activated by light or not. Thus,

also in the dark, the cascade is constantly started.

Mutations in category **7** are characterized by their inability to form dimers. As discussed in section 1.1.5, rhodopsin forms dimers, which arrange in ordered oligomers. It is unclear whether the inability to form dimers is truly the cause of the disease for the mutants in this category, as the mutations are not yet well-studied.

Finally, reported mutations which are known to cause RP or CSNB, but which have not been studied in detail or where the precise disease mechanism is still unclear, fall into the unclassified category.

For the modelling, we can only take into account mutations that have an effect within the scope of the model. This means that we cannot model the influence of any altered trafficking or folding which leads to e.g. accumulation of the mutant rhodopsin or cell stress. However, we can model any change in the kinetics of the phototransduction cascade. This means that the categories **5**, altered transducin activation, and **6**, constitutive activation of the cascade, are within the scope of the modelling. Furthermore, any mutation that leads to an impaired stability of rhodopsin once it has reached the outer segment can be investigated.

After reviewing the references in (Athanasίου et al., 2018), I found that many mutations do not just have one consequence, such as only altered G-protein signalling. Instead, there is often a combination of different effects, e.g. a combination of altered activation of transducin, an altered stability of rhodopsin, and a possible mislocation in the retina. It is not clear whether the combination of all effects leads to the disease phenotype, or whether - and which - one of them is the main cause. Furthermore, it is not clear where the molecular distinction lies between CSNB and the much more severe RP, since many mutations leading to RP or CSNB share similar characteristics.

Therefore, I decided to not model the exact effect of individual mutations, but to group the effects to be investigated into four categories: A higher activation of transducin, a lower activation of transducin, a constitutive activation of transducin by opsin, and a faster thermal decay of activated rhodopsin. Like this, we can investigate the abstract consequences of these individual effects on the light response and see whether they could have a detrimental effect.

For investigations of separate mutations that have - among others - these consequences on the phototransduction cascade, please refer to the following publica-

CHAPTER 3. DETERMINISTIC MODELLING

tions: (Andrés et al., 2003), (Toledo et al., 2011), (Gross et al., 2003), (Budzynski et al., 2010), (Garriga et al., 1996), (Senin et al., 2006), (Deupi et al., 2012), (Fritze et al., 2003).

Thus, I created five mutant models based on the Invergo 2014 model, with generalized modifications as listed in table 3.3. The specific kinetic changes were informed by the above named references, but the changes in parameters were not exactly according to the mutations. To simulate a higher or lower activation of transducin, I changed $k_{G1,0}$ by a factor of 5 and 1/5, respectively. The rate constant $k_{G1,0}$ describes the first step of the activation of transducin: the binding of activated unphosphorylated rhodopsin to transducin. The rate constants for rhodopsin that has been phosphorylated n times are proportional to $k_{G1,0}$. Thus, if we change $k_{G1,0}$, we also change the rates of the binding of all phosphorylated forms of rhodopsin to transducin.

Table 3.3: Mutant models representing kinetic changes for RP or CSNB.

Model	Characteristic	Change in the model
M1	Higher transducin activation	5-fold increase of $k_{G1,0}$
M2	Constitutive activation	800,000-fold increase of k_{Ops}
M3	Faster thermal decay of rhodopsin	800-fold increase of k_{therm}
M4	Lower transducin activation	5-fold decrease of $k_{G1,0}$

To simulate a higher constitutive activation of the cascade, I increased the rate constant of opsin binding to transducin. Opsin is the chromophore-free version of rhodopsin, which is created during the shut-off of the light response. In the normal model, it can bind to the G-protein to activate the cascade as well, but with a very low rate constant k_{Ops} . To see an effect of the change in k_{Ops} , I had to increase it quite significantly, by 800,000. This is an unrealistically high value, but it is easier to see the general effect with such a high increase. Furthermore, we are not investigating realistic mutations here, but rather abstracted and simplified versions to recognize the general effects that are combined in realistic mutations.

Finally, I also included a mutant where the activated rhodopsin has a decreased stability and shuts off spontaneously (thermally) with a higher rate k_{therm} . Again, I had to increase k_{therm} by an unrealistically high value of 800 to make the general effect more easily visible.

With the modified models, I simulated light responses to two different light stimuli: the first stimulus just consists of a saturating flash at $t = 0$ s, and the second consists of a background and a saturating flash starting at $t = 0$ s. The resulting photocurrent ΔJ for all models is shown in figure 3.19.

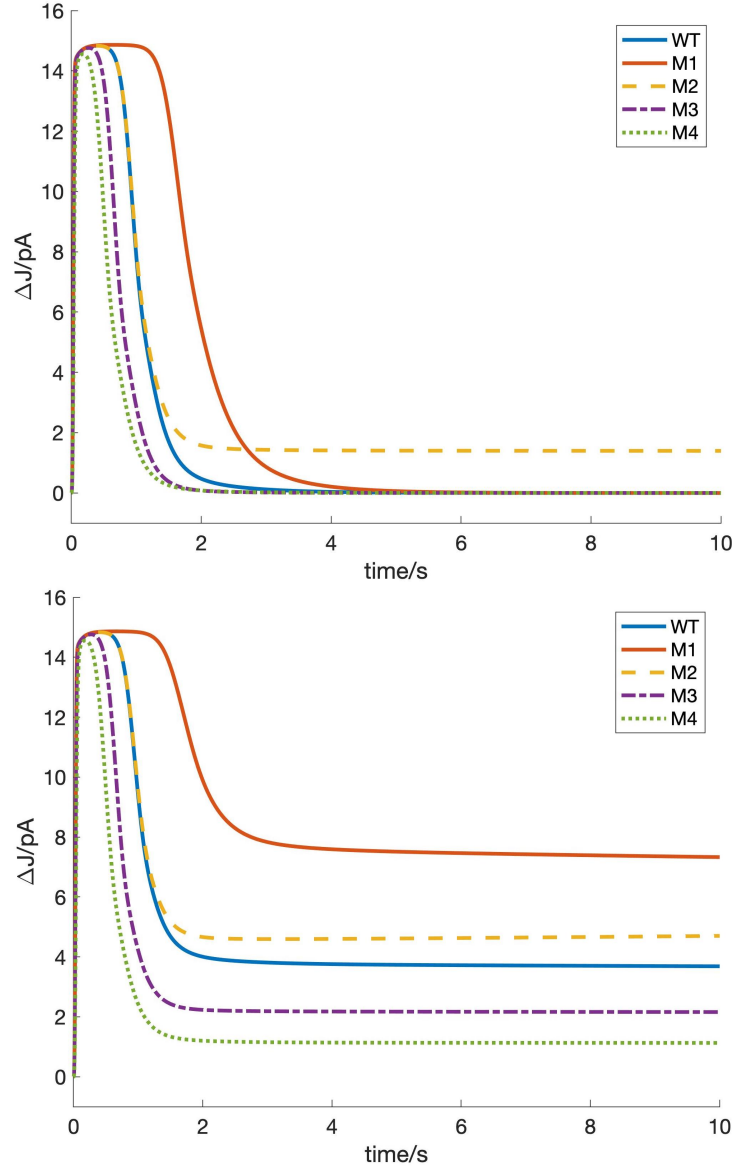


Figure 3.19: Photocurrent ΔJ for the four mutant models and the wild type model. In the upper panel, the light stimulus just consists of a flash at $t = 0$ s. In the lower panel, the light stimulus consists of a flash and a background starting at $t = 0$ s. The different models are the wild type (WT, solid blue line), the mutant with a higher activation of transducin (M1, solid orange line), the mutant with a constitutive activation by opsin (M2, dashed yellow line), the mutant with a faster thermal decay of activated rhodopsin (M3, dot-dashed purple line) and the mutant with a lower activation of transducin (M4, dotted green line).

CHAPTER 3. DETERMINISTIC MODELLING

In the upper panel, we see the response to just the saturating flash without any background. For the two mutants influencing the activation of transducin (M1 and M4), we can see that the effect is equivalent to a brighter or dimmer flash, respectively. This is due to the fact that either more or less transducin molecules and thus effector molecules are activated, as can also be seen in figure 3.20 in the upper panel. That figure shows the effector for the same stimuli as in figure 3.19. For the mutant with a lower thermal stability of rhodopsin (M3), we can see that the light response is shorter in figure 3.19 and that fewer effector molecules are activated in figure 3.20. This is due to the fact that the activated rhodopsin is unstable and decays very quickly compared to the wild type.

Finally, for the mutant with a constitutive activation by opsin, we can see that the response to the initial flash is the same as for the wild type. However, after the flash has ended, there is an increased ΔJ in the dark. This is due to the fact that opsin is produced in the recycling of rhodopsin. This opsin continues to activate transducin, since it takes a rather long time to be recycled to rhodopsin.

In the lower panel in figure 3.19 and 3.20, we can see the response to a saturating flash with a background, starting at $t = 0$ s, in terms of the photocurrent and the effector. For the mutants M1 and M4 with a higher and lower activation of the transducin, we can again see that the response corresponds to one with a higher and lower intensity of the flash and background, respectively.

For the mutant M3 with a decreased thermal stability of activated rhodopsin, we can see that the response to the flash is shorter and that the response to the background is lower. If the rhodopsin activated by the background decays more quickly, then the level of activated rhodopsin from the background illumination is generally lower.

Finally, for the mutant with a higher constitutive activity of opsin, we can see that the response to the background is higher than for the wild type. The wild type and all other mutants have a slowly decreasing response to the background in terms of the photocurrent. This is due to light adaptation. However, the mutant M2 has a slightly increasing response to the background - this is due to the fact that more and more opsin is produced in the shut-off of rhodopsin, which activates the cascade. This indicates that light adaptation is disturbed in the mutant with a constitutive activation of the cascade by opsin.

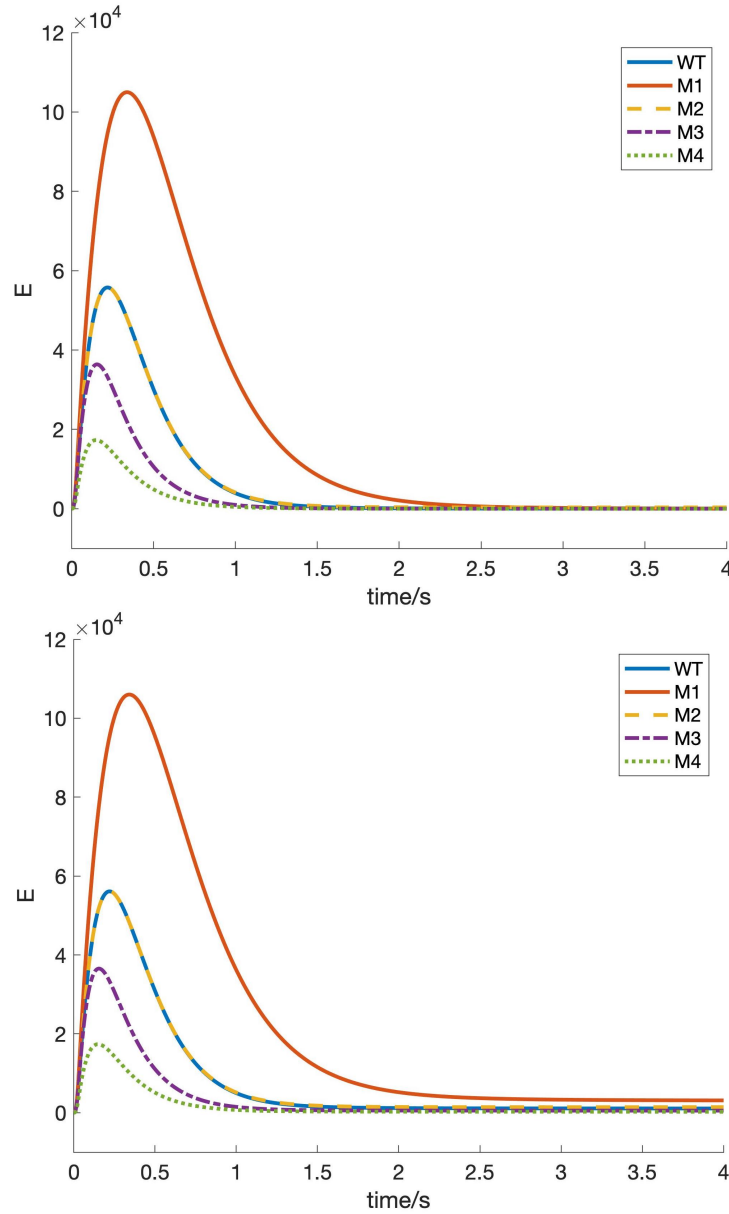


Figure 3.20: Effector for the four mutant models and the wild type model. In the upper panel, the light stimulus just consists of a flash at $t = 0$ s. In the lower panel, the light stimulus consists of a flash and a background starting at $t = 0$ s. The different models are the wild type (solid blue line), the mutant with a higher activation of transducin (M1, solid orange line), the mutant with a constitutive activation by opsin (M2, dashed yellow line), the mutant with a faster thermal decay of activated rhodopsin (M3, dot-dashed purple line) and the mutant with a lower activation of transducin (M4, dotted green line).

We can also investigate the effect of the different mutants on the calcium level in the cell. This is interesting because disturbed calcium levels can lead to cell stress and death. The calcium levels for the same stimuli - flash and flash plus background - can be seen in figure 3.21.

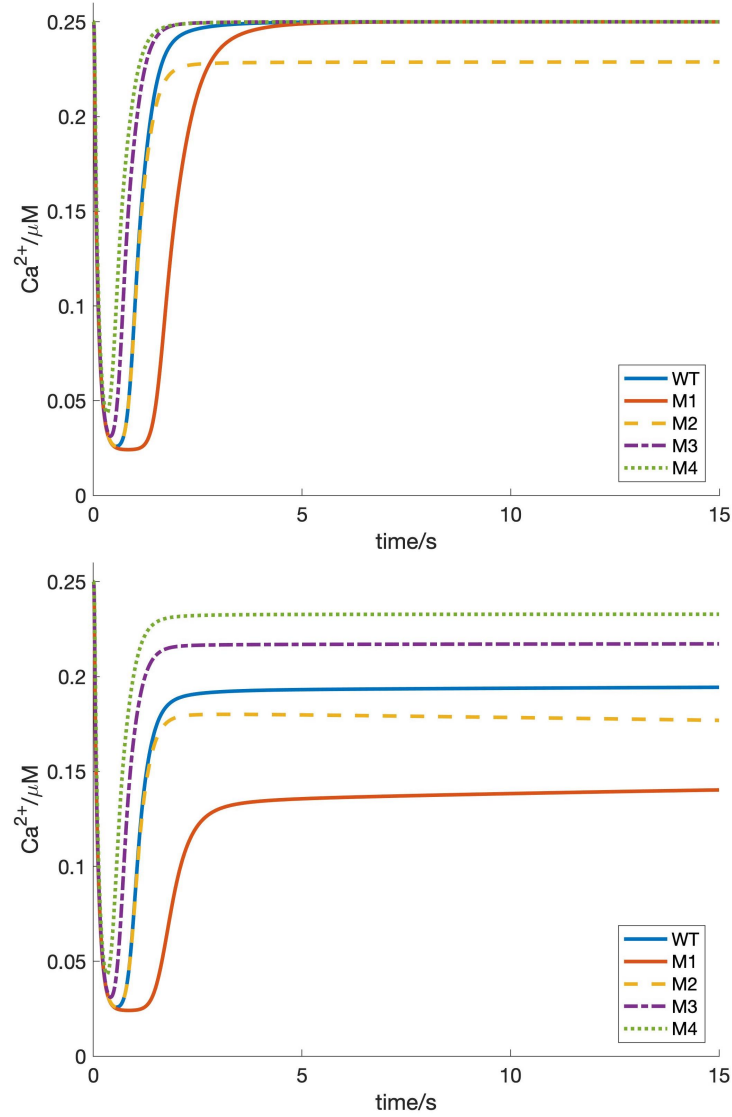


Figure 3.21: Calcium level for the four mutant models and the wild type model. In the upper panel, the light stimulus just consists of a flash at $t = 0$ s. In the lower panel, the light stimulus consists of a flash and a background starting at $t = 0$ s. The different models are the wild type (solid blue line), the mutant with a higher activation of transducin (M1, solid orange line), the mutant with a constitutive activation by opsin (M2, dashed yellow line), the mutant with a faster thermal decay of activated rhodopsin (M3, dot-dashed purple line) and the mutant with a lower activation of transducin (M4, dotted green line).

In the upper panel, we can see that, as a response to the flash, the calcium level decreases and then recovers. For all mutants except for the constitutive activation mutant M2, the calcium level has returned to its dark level after about five seconds. For M2 however, the calcium level stays at a lower value. This is again due to the activity of the opsin, which is created as the rhodopsin activated by the flash is shut off. We can see that the calcium level is disturbed for a long time.

For the stimulus consisting of a flash and a background, we see the same effect on the calcium level. After the flash, the calcium level stays lower than for the wild type. Again, we can observe that all mutants except for M2 exhibit light adaptation, as the calcium level slowly increases back towards its dark value even with the background illumination. For M2 however, this is not the case, as the opsin continues to activate the cascade.

Concluding from the results on disease modelling, we can use it to give us an indication of disease mechanisms and to help us understand how exactly phototransduction diseases work at the level of the phototransduction cascade.

4 | Stochastic modelling

In this chapter, I am presenting the development of the stochastic models as well as the resulting simulations of single photon responses and other dim light responses. Doing stochastic simulations is important for the investigation of single photon responses. In deterministic simulations, only the *average* behaviour of the responses can be studied. However, due to the inherent randomness of the responses, each single photon response is different from the average behaviour. To find out more about the statistical properties of single photon responses, like the variability and its dependence on different features of the phototransduction cascade, we need to perform stochastic simulations of an ensemble of single photon responses.

4.1 Stochastic amphibian model

My first approach toward creating a stochastic model was to make versions of the Dell’Orco 2009 and Invergo 2014 models that would be suited for stochastic simulations.

The basic approach I followed for all the stochastic models was to separate the model into a frontend model - which is simulated stochastically - and a deterministic backend model. This idea was first implemented in (Hamer et al., 2005). The frontend model simulates the effector and all species influencing it: rhodopsin, transducin, recoverin, the rhodopsin kinase, arrestin, opsin, PDE and RGS. For these molecular species, we are dealing with potentially low numbers of activated or interacting molecules, and therefore it is essential that they are treated stochastically (see section 2.2.4).

The backend contains the molecular species which lie downstream from the effector: cGMP, calcium, the GC-GCAP system and the ion channels. The molecular species in the backend model are abundant, therefore it is not strictly necessary to perform a stochastic simulation, and it would be very time-consuming due to the large number of interactions.

The complete simulation is performed by first simulating the frontend to arrive at a trace for the effector, which is then used as an input for the backend to compute ΔJ . Due to this subdivision of the model, all feedback mechanisms from

CHAPTER 4. STOCHASTIC MODELLING

the backend species to the frontend species need to be deleted, since the backend simulation takes place after the frontend simulation.

The first stochastic model I worked with was the amphibian stochastic model derived from the Dell’Orco 2009 model. Daniele Dell’Orco had already divided the model into a frontend and a backend model, which I was able to use. The frontend model is the normal model, where the molecular species of free calcium, calcium in buffers and cGMP were deleted, as well as all reactions involving them. From these deleted species and their reactions, the backend was built up. The frontend and backend model are shown in figure 4.1 and all reactions and parameters can be found in the appendix in section A.1.

Since the original Dell’Orco model does not contain any feedback from the backend into the frontend, no reactions needed to be deleted. However, some simplifications were carried out.

First of all, RGS is not treated as a variable molecular species in the model, since its concentration hardly changes during dim light responses. Reducing the number of variable molecular species reduces the computational effort to simulate the model, thus RGS was set to a constant value and included in the reaction rates. Furthermore, the recoverin dynamics were deleted from the model. In the original Dell’Orco 2009 model, recoverin in the rhodopsin kinase-binding form was assumed to stay at its dark concentrations, which is known as a quasi-steady state assumption. It is valid whenever the concentration does not deviate much from the steady state (dark) concentration. Since the concentration of rhodopsin kinase hardly changes during the single photon response, these dynamics were deleted in the stochastic model.

Importantly, models are not allowed to contain variables for stochastic simulations with `IQMstochsim2`. Therefore, all variables had to be replaced by parameters. In the frontend, this concerned a few reaction rate constants that were expressed as a function of the number of phosphorylations of rhodopsin, such as the rate constants for the interaction of transducin or arrestin with rhodopsin. The rate constants were calculated and replaced by parameters with their numerical values. Moreover, the effector had been expressed as a variable before - it will be explained in the next paragraph how the effector was now extracted from the simulation.

4.1. STOCHASTIC AMPHIBIAN MODEL

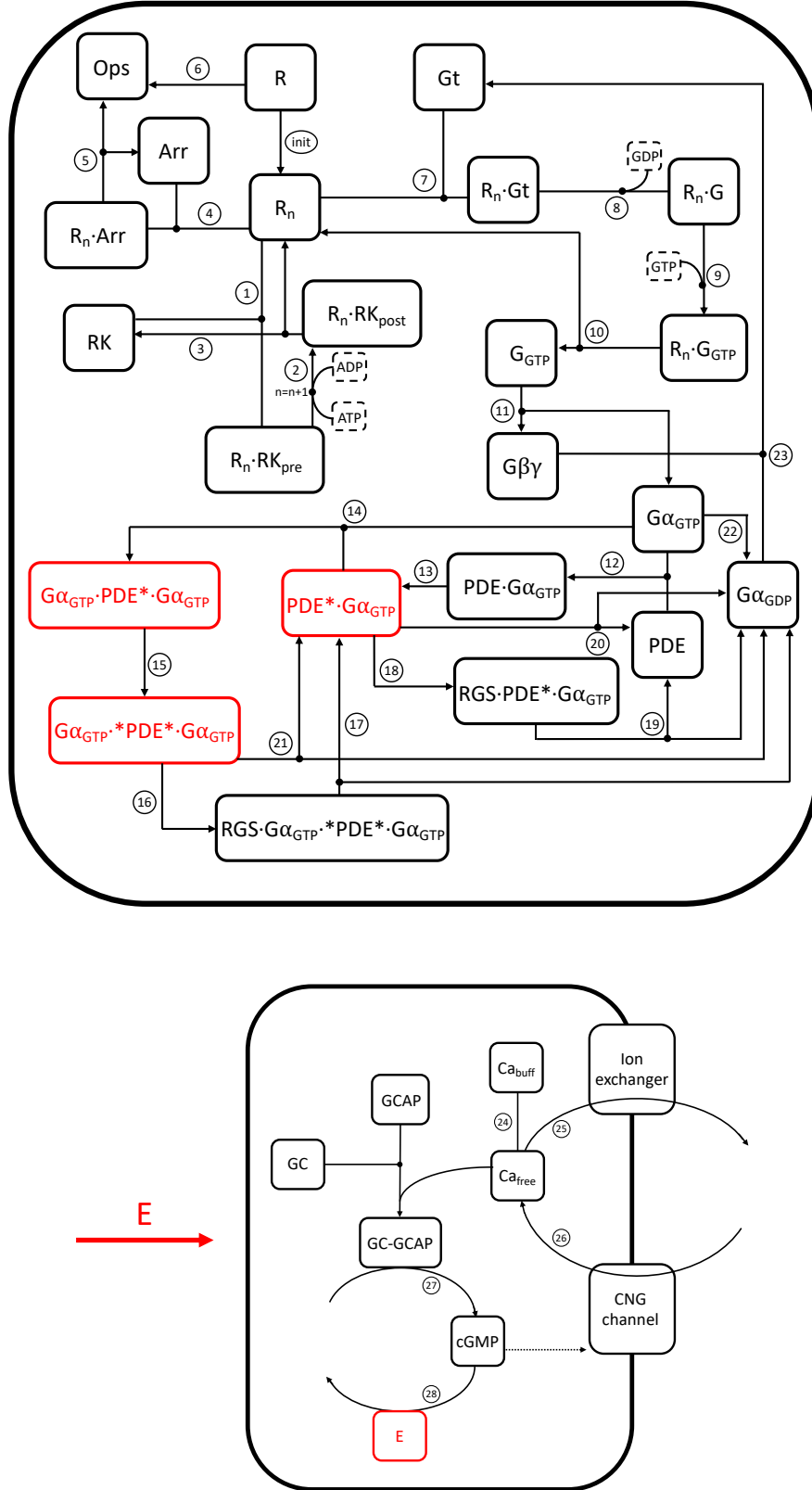


Figure 4.1: Stochastic frontend (top) and backend (bottom) of the amphibian model. The species making up the effector in the frontend model are marked red. Those are used as an input for the backend model. The numbered reaction equations and all parameters can be found in the appendix in section A.1.

CHAPTER 4. STOCHASTIC MODELLING

The initial condition of $R_0 = 1$ was set in the model: the simulation thus starts with one activated rhodopsin molecule to simulate a single photon response. The activation reaction $R \rightarrow R_0$ and the stimulus definition were removed from the model, since we now set the activated rhodopsin as an initial condition.

Importantly, for the stochastic simulations, the molecular species amounts (i.e. initial conditions) need to be specified in terms of molecule *numbers*, not concentrations, since the stochastic simulation takes into account single reactions and thus single molecular events. This is already the case for the molecular species in the frontend, thus no further modifications are necessary.

To carry out a simulation of a single photon response, first the frontend is simulated for a desired time (e.g. 10 seconds). Next, we need to extract the trace for the effector from the simulation results. Since the effector is no longer included as a variable in the model, we instead extract the molecular species traces for `PDE*` and `*PDE*` by calling `simulation.statevalues`.

Then, the effector is input into the backend by using the interpolation function `interp0IQM` for the trace of the activated PDE species and inputting the resulting trace into the model as a variable using `model.variables`. We can then perform a simulation for the resulting backend model.

In figure 4.2, ten traces for the effector, resulting from the stochastic frontend simulation, and the photocurrent ΔJ , resulting from the consecutive deterministic backend simulation, are shown. They are compared to the result of the fully deterministic simulation. The maximum effector numbers lie between 100 and 400 activated PDE subunits. The resulting ΔJ has maximum amplitudes between 0.8 and 2.3 pA. There is obviously some variability between the separate runs of the stochastic simulations, but the resulting traces for ΔJ still show similar kinetics, as we would expect.

4.1. STOCHASTIC AMPHIBIAN MODEL

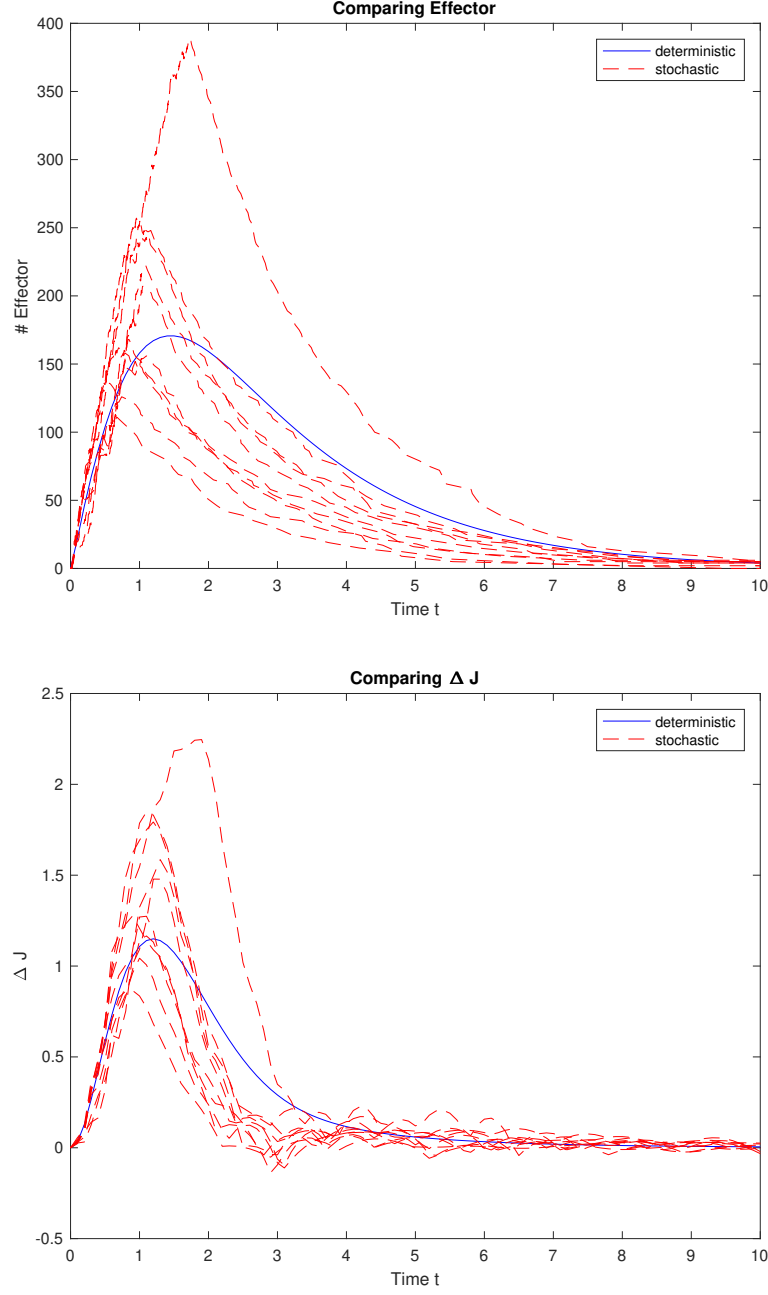


Figure 4.2: Stochastic and deterministic simulation results for single photon responses in the stochastic amphibian model. In the upper panel, the effector is shown over the time in seconds. In the lower panel, the photocurrent ΔJ in pA is shown. Blue traces result from deterministic simulations, while red dashed traces are the result of 10 runs of stochastic simulations.

4.1.1 Multiple phosphorylation sites

Using the stochastic model, I wanted to check the influence of multiple phosphorylation sites on the reproducibility of single photon responses like in (Doan

et al., 2006). In this publication, phosphorylation sites of rhodopsin in mouse rods were removed using mutagenesis and single photon responses were measured. The experimental results show that multiple phosphorylation sites are essential for reproducible single photon responses and that the SPR variability increases with fewer available sites.

To recreate this experiment in my simulations, I created models with fewer available phosphorylation sites: from the normal 6 sites down to 0. The different phosphorylation sites are treated as identical and interchangeable in the model: we only keep track of the absolute number of phosphorylations of each rhodopsin molecule, not of the specific phosphorylation site that was phosphorylated. This simplifying assumption is due to two factors: firstly, we do not have sufficient information to model different phosphorylation sites and it would increase the computational demand. Secondly, the results in (Doan et al., 2006) show that it is mainly the number of phosphorylation sites that matters, not so much the specific site that was removed.

Usually, in deterministic simulations, the most elegant solution would be to create an experiment for each amount of available phosphorylation sites and to merge these with the same, unchanged model for the simulations using `IQMmergemodexp`. However, models resulting from the function `IQMmergemodexp` are not suitable for stochastic simulations, since the changes in parameters and/or states are incorporated as variables, and models for stochastic simulations are not allowed to contain variables. Thus, it is necessary to create separate models for each number of phosphorylation sites. This has no consequences on the outcome of the simulations, since the modifications to the model are identical.

After those modifications, I simulated single photon responses in these models. The results can be found in figure 4.3. For each number of available phosphorylation sites, I performed 10 stochastic simulations.

As can be seen in the figure, the variability of the single photon responses increases when fewer phosphorylation sites can be phosphorylated. Furthermore, the shut-off takes longer, the more sites have been removed. For zero phosphorylation sites, the responses take a longer time than the simulated 80 s to shut off.

This result is very similar to what was found experimentally using mutagenesis in mouse rods in (Doan et al., 2006): all six phosphorylation sites are required for reproducible single photon responses. The reason behind this is that the multiple phosphorylations lead to a multi-step shut-off process: each separate phosphoryla-

4.1. STOCHASTIC AMPHIBIAN MODEL

tion contributes to reducing the affinity for the G-protein, thus preventing further activation of the cascade. At the same time, the affinity for arrestin increases, and thus also the probability of a complete shut-off (Gibson et al., 2000). When we decrease the number of possible phosphorylations, we decrease the number of intermediate shut-off steps. This increases the variability and the duration of the single photon response, on average.

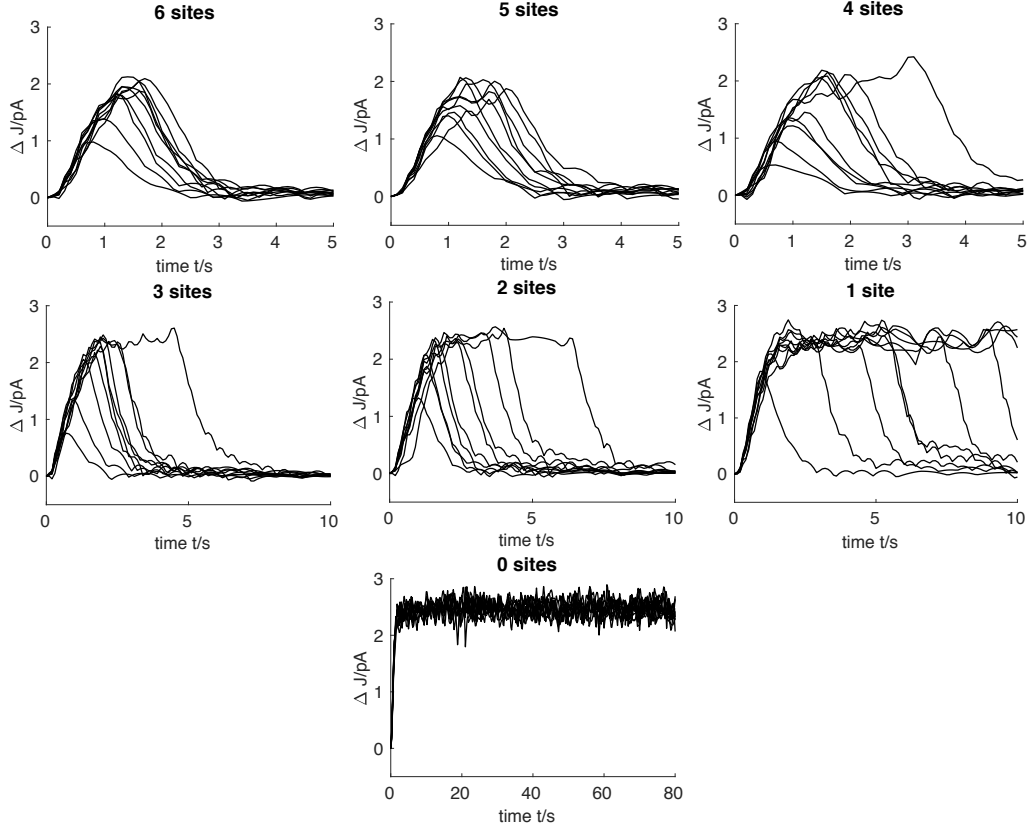


Figure 4.3: Single photon responses simulated with the stochastic amphibian model with 6 to 0 available phosphorylation sites. Each plot contains 10 stochastic simulation runs.

In the simulations with zero phosphorylation sites, rhodopsin cannot be phosphorylated anymore. This also means that it cannot be shut off by arrestin, because this requires at least one phosphorylation. The only shut-off option is the thermal or spontaneous shut-off of rhodopsin, which has a comparatively low rate and thus takes a longer time.

To summarize, we can reproduce the results concerning the importance of the phosphorylation of rhodopsin from single-cell recordings in mouse rods from (Doan et al., 2006) in our simulations. We will investigate this effect in more detail for

the other models in the following.

4.2 Stochastic mouse model

Next, I created a stochastic mouse model from the Invergo 2014 model. I created a frontend and backend model by separating the species and their reactions as described before. In this case, I had to delete a feedback mechanism that fed back from the backend into the frontend model, namely the calcium feedback on recoverin and the rhodopsin kinase.

To make sure that this change did not disturb the kinetics, at least for dim light responses, I investigated the consequences of the removal in deterministic simulations in detail, as already described in section 3.2. I found out that there were no consequences for the kinetics of the light response for brief flashes without any background illumination. Since we want to simulate single photon responses with the stochastic model, this is fine: we will not simulate stimulus paradigms where the deletion of the feedback would have any consequences. Thus, I removed recoverin from the model and assumed the concentration of rhodopsin kinase to be static (the so-called quasi-steady state assumption).

The frontend thus contains the species rhodopsin, rhodopsin kinase, opsin, arrestin, transducin, PDE, and RGS, and their interactions. The backend contains all the species downstream from the effector: cGMP and calcium as well as their regulation by the GC-GCAP system and the channels, implicitly in the reaction rates.

I made a few modifications to the model in parallel to the amphibian model. All reaction equations and parameters of the new model can be found in the appendix in section A.2.

Obviously, I also needed to replace all variables by numerical parameters. Furthermore, I deleted the activation of rhodopsin and the stimulus description. Moreover, I modified the model slightly by removing reactions that were not immediately important for the simulations I wanted to perform.

Those reactions are the recycling of opsin and the precoupling of rhodopsin and transducin. The recycling of opsin to recreate rhodopsin does not matter for the single photon response and other brief flashes, since the recycled rhodopsin will not be activated within the short time frame of the photoresponse. Therefore, I left it out to save computational power.

The precoupling of rhodopsin and transducin and its impact on the single photon

response will be investigated in detail in section 4.5. For this model, I wanted to simplify the initial condition and just consider non-precoupled activated rhodopsin. Thus, I removed the precoupling reactions for this first investigation.

With the new stochastic frontend and deterministic backend, we were able perform simulations in the same way as with the amphibian model. In figure 4.4, I show the resulting effector and photocurrent ΔJ .

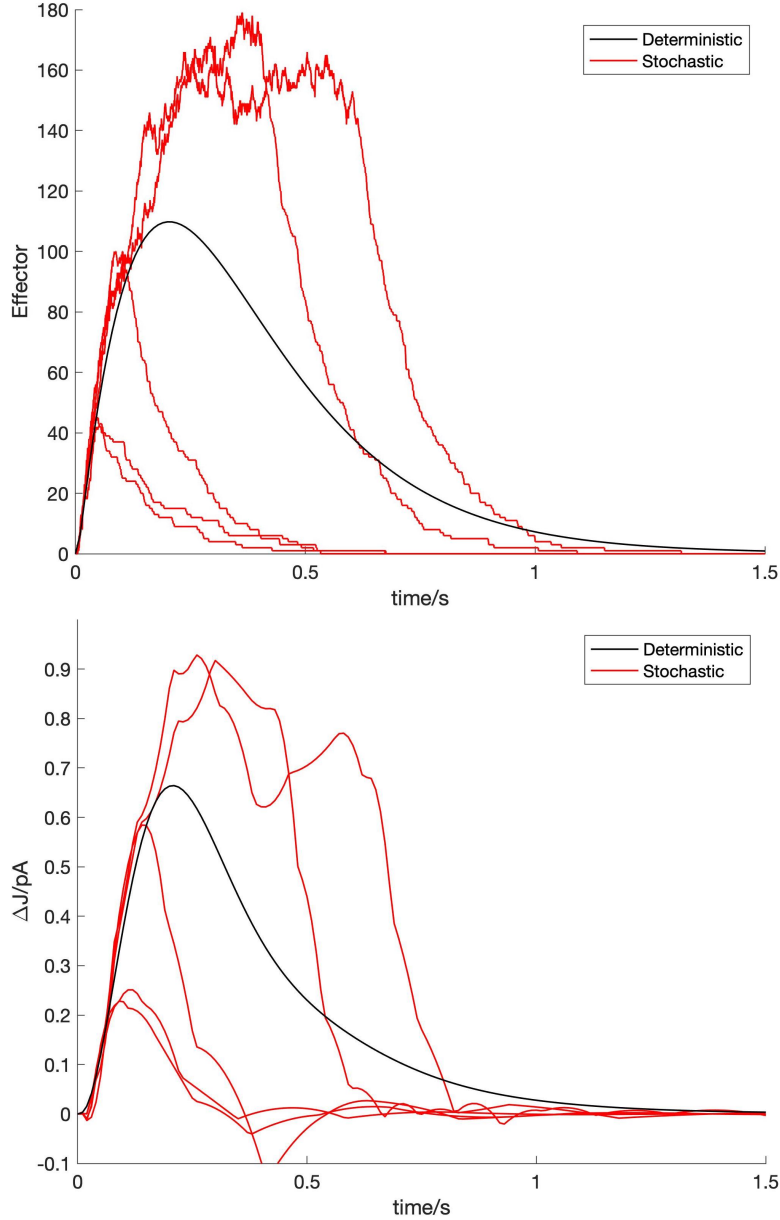


Figure 4.4: Stochastic and deterministic simulation results for single photon responses in the stochastic mouse model. In the upper panel, the effector is shown. In the lower panel, the photocurrent ΔJ is shown. Black traces result from deterministic simulations, while red traces are the result of 5 runs of stochastic simulations.

Again, we can see that the stochastic simulations show some variability, but a common response shape. Compared to the amphibian single photon response in figure 4.2, the single photon response in the mouse model is much faster in the excitation and recovery phase. The average number of activated effector subunits is slightly higher than 100 and therefore comparable to the simulation results in the amphibian model. The amplitude of the photocurrent is lower, at 0.65 pA as compared to 1.2 pA in the amphibian model.

4.2.1 Multiple phosphorylation sites

Like in the amphibian model, I wanted to check the influence of the availability of multiple phosphorylation sites on the reproducibility of the single photon response in the mouse model.

Thus, I did simulations in the stochastic mouse model for different numbers of available phosphorylation sites of rhodopsin. The results can be found in figure 4.5.

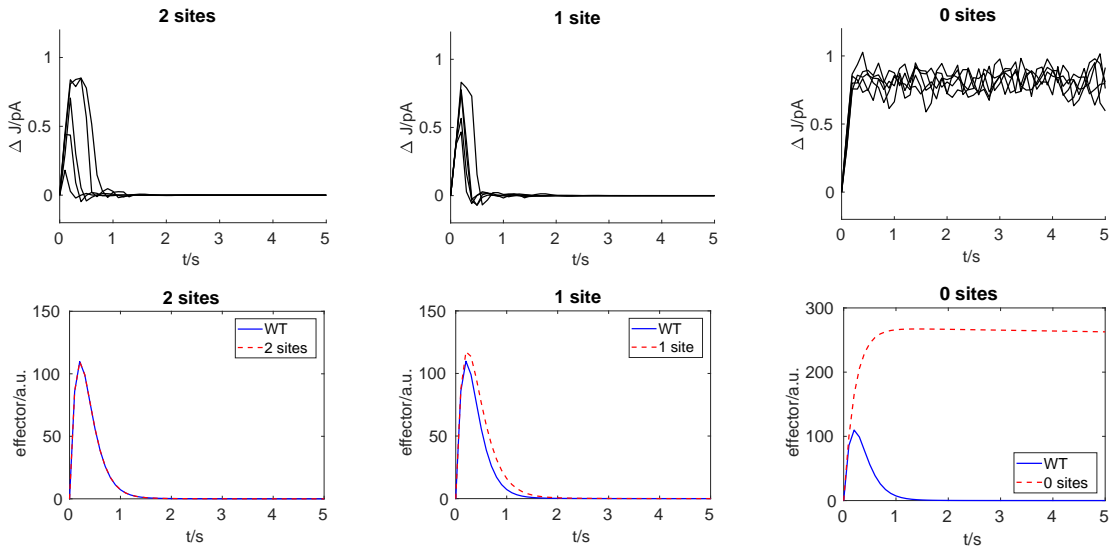


Figure 4.5: Single photon responses simulated with the stochastic mouse model with two to zero available phosphorylation sites. The upper row shows stochastic simulations. Each image contains five stochastic simulation runs. The lower row shows deterministic simulations of the effector during the single photon response with two to zero available phosphorylation sites (dashed red lines), compared to the model with the full six phosphorylation sites (solid blue lines).

The upper row of the figure shows stochastic simulations for different numbers of available phosphorylation sites like in figure 4.3. However, I only display the data for two to zero available phosphorylation sites, since the simulations for larger

numbers of available sites looked very similar: there was no noticeable increase in variability or in the duration of the single photon responses.

In the lower row, I show deterministic simulations of the effector compared between the model with 6 available phosphorylation sites (blue solid lines) and the model with two to zero available phosphorylation sites. In the deterministic simulation, we cannot examine the change in variability, but the increase in duration of the response can be compared more easily, without any distractions by the noisiness of the responses. In these simulations, we can see that the duration of the single photon response only starts to increase when we have only one phosphorylation site left.

To conclude, in the mouse model, we only need two to three phosphorylation sites to reproduce the results of the normal model with the full six phosphorylation sites. This is in contrast to the experimental results by (Doan et al., 2006) from mice, and to the simulated results in the amphibian model, where all phosphorylation sites are significant. Possible reasons for this difference are discussed in chapter 5.

4.2.2 Different knockout models

To further assess the suitability of the model for simulating single photon responses, I simulated single photon responses in different knockout models. These results can be compared to various experimentally recorded single photon responses, which are shown in figure 4.6 on the left.

Before doing any of the simulations, I improved the model by re-introducing recoverin, using a quasi-steady state assumption that the calcium-free, the calcium-bound and the rhodopsin kinase-bound states of recoverin are in their respective steady-state dark concentrations throughout the entire simulation. As previously discussed, this simplification is only valid for brief flashes of light without any sustained background - this is the case for the single photon responses simulated here.

Next, I created models for the different knockout conditions. As explained earlier, we cannot use the experiment description with `IQMmergemodexp` with the stochastic simulations and have to create separate models. To create the knockout models, I only removed the knocked-out molecular species, and none of the kinetic parameters of the model were changed for the simulations. For the implementation of the GCAPs knockout, see section 3.1.1: the activity of the GC is fixed at its dark activity.

I implemented models with a knockout of the rhodopsin kinase, a knockout of the GCAPs, a knockout of arrestin, and a completely substituted mutant of rhodopsin (CSM) where all the phosphorylation sites are substituted, i.e. knocked out. The results of a first deterministic investigation can be found in figure 4.6.

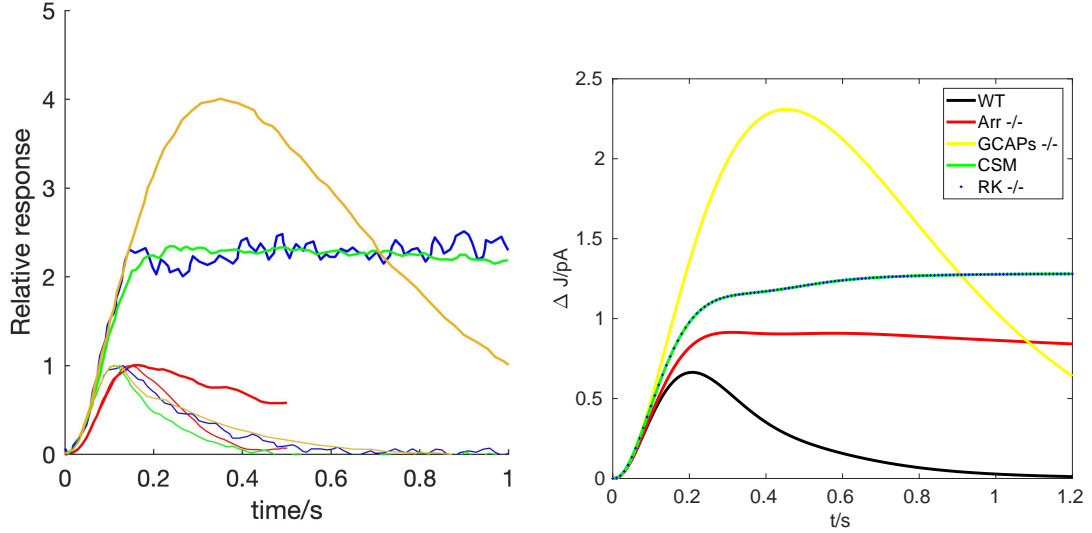


Figure 4.6: Single photon responses in different knockout models. Left: experimental data from mouse rods. Arrestin knockout (Arr $-/-$, red) from (Xu et al., 1997), completely substituted mutant (CSM, green) from (Mendez et al., 2000), GCAPs knockout (GCAPs $-/-$, yellow) from (Burns et al., 2002), rhodopsin kinase knockout (RK $-/-$, blue) from (Chen et al., 1999). The respective wild type responses are plotted in matching colors with a thinner line, and all responses have been normalized to a maximum wild type amplitude of 1 pA. The arrestin knockout response has been scaled to the same amplitude as the wild type response. Right: deterministically simulated single photon responses in models with the respective knockouts: arrestin (Arr $-/-$, red), GCAPs (GCAPs $-/-$, yellow), rhodopsin kinase (RK $-/-$, blue) and the completely substituted mutant (CSM, green) as well as the wild type (WT, black).

We can see that the model is generally able to reproduce the changed kinetics of the single photon response in the different knockout conditions.

In the GCAPs knockout (yellow line in the left and right panel), the amplitude of the single photon response is increased about four-fold and the shut-off is much slower. This is reproduced well in the simulated responses. The reason for the changed kinetics is that the GC is not regulated in a calcium-dependent manner anymore when the GCAPs are missing. As a consequence of the light response, the cGMP and calcium concentrations drop. In the wild type, the GCAPs then activate the GC to produce more cGMP than the dark rate because of the drop in calcium concentration. This restores the cGMP concentration, which opens the

cyclic nucleotide gated channels, in turn restoring the calcium concentration.

In the knockout, this is not the case: the GC stays at its dark production rate of cGMP. The upstream part of the signalling cascade (rhodopsin, transducin, PDE) is normally shut off, but the low GC activity in the absence of the GCAPs cannot counterbalance the hydrolytic rate of cGMP. Thus, ΔJ reaches a much higher amplitude and takes a longer time to return to the dark state.

Knocking out the rhodopsin kinase (blue lines) and removing all of rhodopsin's phosphorylation sites (green lines) has the same effect on the light response. The consequence of the modifications is the same: rhodopsin can no longer be phosphorylated. In the experimental and simulated data, we observe that the light response rises to about the double amplitude of the wild type single photon response and then stays at this amplitude, with no shut-off taking place. This is because rhodopsin does not get phosphorylated and the activation of the photo-transduction cascade is thus not terminated. The phosphorylation of rhodopsin is an essential first step of the shut-off: not only does it decrease rhodopsin's activity by reducing the affinity for transducin, but it also enables binding to arrestin, which completely terminated rhodopsin's activity.

When no phosphorylation can take place, because the rhodopsin kinase is missing or because rhodopsin has no phosphorylation sites, rhodopsin cannot be shut off and it cannot bind to arrestin. The only possibility for the shut-off is the thermal decay of activated rhodopsin, which has a low rate and thus takes a long time to spontaneously occur. Thus, the light response increases to a higher amplitude and stays there, because the activity of rhodopsin is not terminated.

Finally, the arrestin knockout (red lines) also impacts the shut-off of the response. Unfortunately, the experimental data from (Xu et al., 1997) only extend for 0.5 s. Still, we can see that the response amplitude decreases after the maximum, but less strongly than in the wild type. In the simulations, this looks slightly different. We cannot compare the response amplitudes, since the experimental trace for the knockout is normalized to the same amplitude as the wild type response. However, the shut-off in the simulated data is weaker than in the experimental data: the decrease in amplitude after the maximum is slower.

In summary, the model reproduces the experimental data well, except for the shut-off for the arrestin knockout. This is further discussed in chapter 5.

4.3 Small stochastic model

Before performing more quantitative comparisons and stochastic simulations of single photon responses, I wanted to update the model in parallel to the deterministic model in section 3.1.1. Furthermore, when doing stochastic simulations, I noticed that many of the simulated species hardly change during the single photon response. If their removal or a quasi-steady state assumption does not change the kinetics of the single photon response, they do not need to be in the stochastic model for simulating single photon responses, since including them only increases the computational demand of the simulations.

With this in mind, I set out to update the model to the new insights into the effector, which are that fewer effector-transducin complexes are activated than was assumed earlier (just 12-14) (Yue et al., 2019), and that the main effector is the double-activated PDE, with the single-activated form only having a fraction of the activity (2.5 % rather than 50 %, as assumed before) (Qureshi et al., 2018).

Please recall that, for the deterministic model, we were able to achieve a lower number of effector-transducin complexes. However, it was not possible to arrive at a sufficient number of double-activated PDE molecules.

However, for the stochastic model, I had an idea how to integrate this result as well. The problem with the deterministic model had been that the activated species were effectively diluted over the entire outer segment, resulting in a low concentration, specifically of the activated transducin and PDE. Since those concentrations are multiplied for the rate of the second activation of a single-activated PDE, this rate was basically too low to reliably lead to even one double-activated PDE molecule during the single photon response.

I realized that it was possible to scale down the model to smaller volumes, leading to less dilution of the activated species and higher effective rates, e.g. for the second activation of the PDE. For a model that is essentially made to simulate single photon responses, this does not lead to any problems with the depletion of, for example, the G-protein. The frontend species interact with the disc membrane anyways and do not typically diffuse very far during the time span of a single photon response. The backend species do, but the backend will not be scaled down - only the frontend, to arrive at a more realistic description of the effector.

4.3. SMALL STOCHASTIC MODEL

I scaled down the stochastic mouse model to a volume of about two discs and adapted some of the previously adapted parameters similarly to the procedure described in section 3.1.1. I furthermore reduced the model by removing some reactions that were not relevant for the single photon response and thus only slowed down the stochastic simulations. All reaction equations and parameters of the new model can be found in the appendix in section A.4.

I removed opsin from the model: the recycling of opsin to rhodopsin does not contribute to brief responses like the single photon response. Opsin can activate the cascade, but this reaction has a very low rate and the probability of actually seeing it in stochastic simulations is thus also low. Therefore, it was possible to remove opsin from the model without disturbing the kinetics of the single photon response.

I also removed all phosphorylation sites of rhodopsin beyond three sites. As already hinted at in section 4.2.1, only two of the phosphorylation sites of rhodopsin are typically phosphorylated during the single photon response. To check this more quantitatively, I performed a deterministic simulation of the single photon response in the updated deterministic model and checked the numbers of rhodopsin in the different phosphorylation states. The result can be found in figure 4.7.

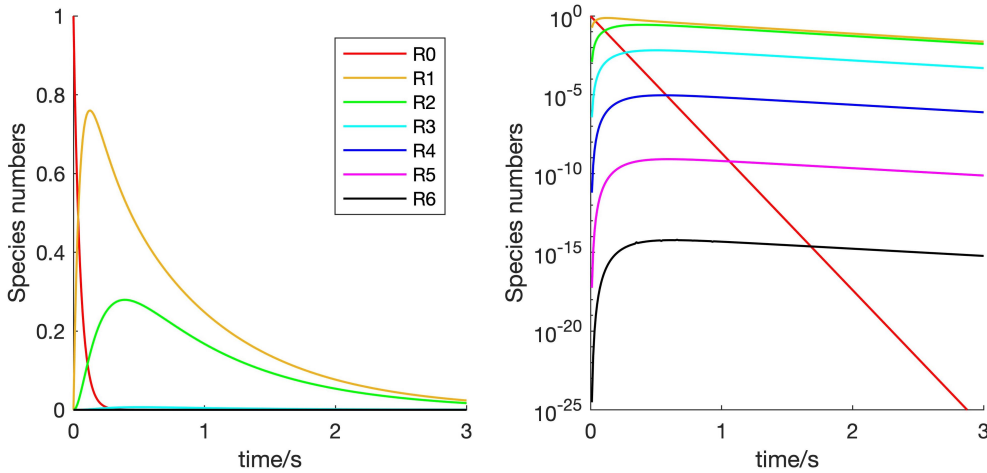


Figure 4.7: Rhodopsin in the different phosphorylation states during the deterministically single photon response. Left, with linear axes and right, with semilogarithmic axes. The line colors represent the amount of phosphorylations of the activated rhodopsin: zero (red), one (yellow), two (green), three (light blue), four (dark blue), five (pink) and six (black).

When interpreting the figure, we need to keep in mind that we are looking at the result of a deterministic simulation. This means that, when the molecule number of a particular species is lower than one, this is the *average* number of molecules

CHAPTER 4. STOCHASTIC MODELLING

that we would expect over a large number of realizations. When this number is very small, the molecular species will rarely be found in stochastic simulations.

At time $t = 0$ s, we start with one activated rhodopsin with zero phosphorylations. The amount of rhodopsin with zero phosphorylations then quickly decays, as rhodopsin gets phosphorylated. From the linear shape in the semilogarithmic plot we can confirm that this is an exponential decay, as we would expect for a single-step shut-off.

Both the rhodopsin with one and two phosphorylations are present in amounts larger than 0.1 molecules, which means that we would definitely see them in stochastic simulations. In the plot with the linear y-axis, it can be nicely seen that the peak in molecule numbers for higher phosphorylations is shifted towards larger times, since each phosphorylation step takes some time.

For three and more phosphorylations, we can see in the semilogarithmic plot that they become less and less abundant and thus less and less probable to be found during a simulation. For four phosphorylations, the peak lies around 10^{-5} - this makes it so improbable to find this species in a simulation that we would probably never see it in the amount of simulations we run. Thus, we can make a cut-off after three phosphorylations without disturbing any kinetics.

I also left out the dimerization and tetramerization of arrestin. For the duration and amplitude of the single photon response, there is hardly any change in these species, so they can be left out without any problems. The same goes for recoverin, as before: the feedback of recoverin on the rhodopsin kinase only becomes important for stimuli with a prolonged background, which is not the case when simulating single photon responses. Therefore, it is also left out.

Another novelty of the small stochastic model is that the precoupling of rhodopsin is added back into the model. We wanted to investigate the consequences of the precoupling mechanism on the single photon response, which is why I added it back into the model. In section 4.5, I will explain how I modified the initial conditions to compare single photon responses triggered by precoupled and non-precoupled rhodopsin molecules.

There was one issue with the precoupling reaction: in the dark state, many G-proteins rapidly associate and dissociate with rhodopsin, which is responsible for a lot of reaction events in the simulations. I realized that these reactions are

4.3. SMALL STOCHASTIC MODEL

basically irrelevant as long as two conditions are met: first, they do not involve any activated rhodopsin - since we will treat this case separately in the initial conditions, this condition is met. Secondly, the reactions need to be in equilibrium: in that case, the amount of precoupled rhodopsin and G-protein will stay constant, apart from small fluctuations. This is the case in the dark. For the situation after an illumination, let us take a look at the reaction rates for the association (v_f) and dissociation (v_r) of non-activated rhodopsin and G-protein between their separate forms and the complex $R \cdot Gt$:

$$\begin{aligned} v_f &= k_{Gpre1} * Gt * R \\ v_r &= k_{Gpre2} * R \cdot Gt. \end{aligned} \tag{4.1}$$

In the dark state, this reaction is in equilibrium, thus $v_f = v_r$ and $v_f - v_r = 0$. After illumination, the concentration of free G-protein Gt decreases, since some of the G-protein is associating to rhodopsin and PDE. Thus, the rate v_f of formation of the pre-complexes decreases, while the dissociation rate v_r stays the same. The effect is a slight decrease of formed pre-complex, freeing up some rhodopsin and G-protein.

My idea was to substitute this reversible reaction by an irreversible reaction, in the direction of the dissociation of the complexes, since this is the relevant reaction direction for the single photon response. It saves the computational effort of a lot of separate association events, while still allowing for the effect of some additional G-protein being released from $R \cdot Gt$ -precomplexes as a result of the light response. This reaction then goes into the dissociation direction, with the rate

$$v = k_{Gpre2} * R \cdot Gt - k_{Gpre1} * Gt * R. \tag{4.2}$$

In equilibrium, the rate is zero, leading to stable population of precoupled and non-precoupled rhodopsin and transducin. There is no interconversion between the two, but as established above, this does not matter as long as we define the activation of the cascade as an initial condition. As a result of the light response, $k_{Gpre1} * Gt * R$ decreases and becomes smaller than $k_{Gpre2} * R \cdot Gt$, leading to a non-zero dissociation rate for the precomplexes. This results in the dynamics that we are interested in, while reducing the computational effort of doing the simulations.

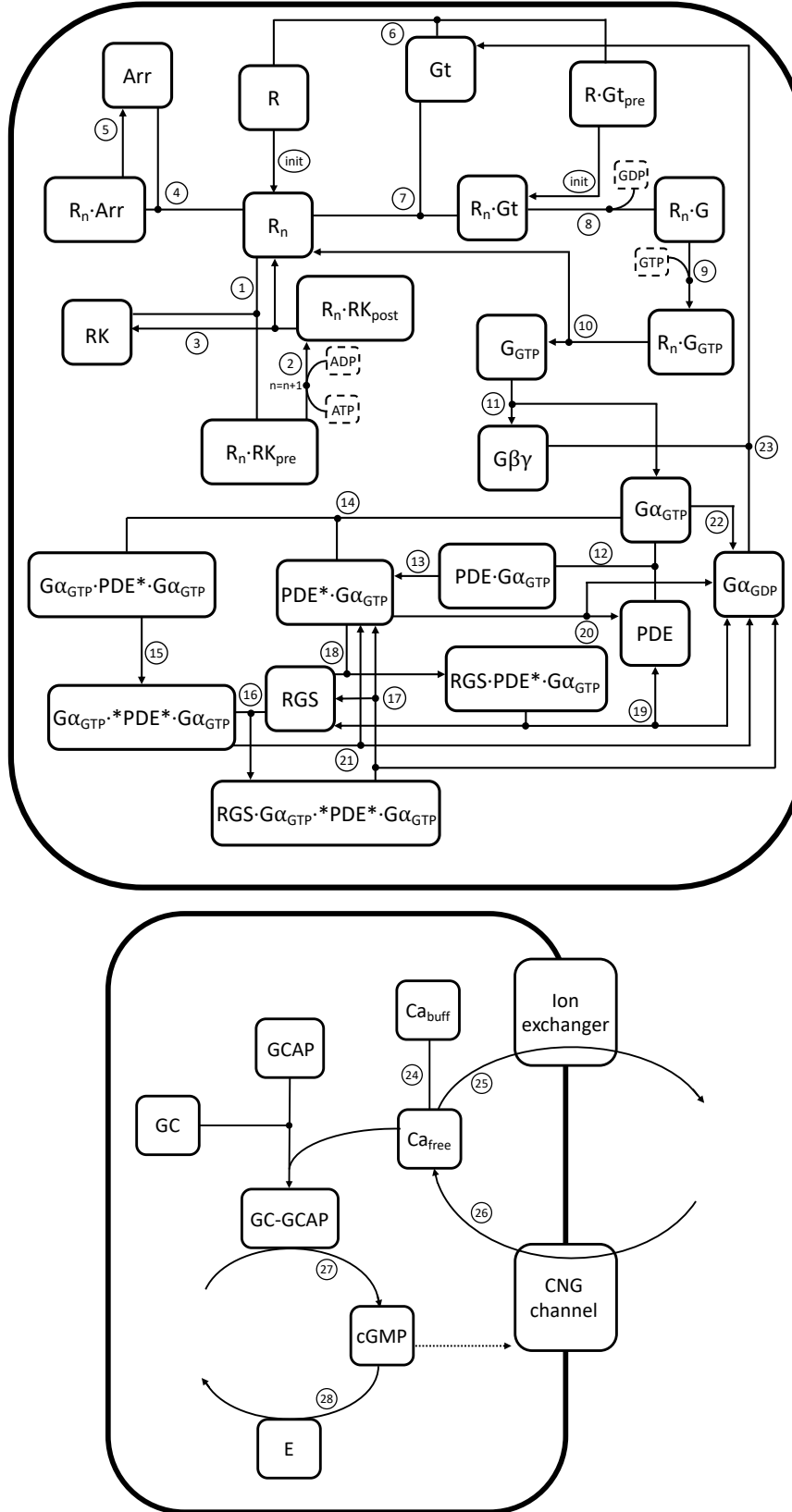


Figure 4.8: Reaction network for the new, small stochastic model. The upper network is the stochastic frontend model, which has been scaled down to a smaller volume. The lower network is the deterministic backend, which is simulated for the full outer segment volume. The numbered reaction equations and all parameters can be found in the appendix in section A.4.

In the backend, the only change was to adapt the parameter defining the catalytic activity of the effector, β_{sub} , to the new amount of effector molecules. The backend is simulated deterministically for the full outer segment volume, using the effector from the frontend model as an input.

The final reaction network for the small model can be found in figure 4.8.

4.3.1 Single photon responses in the new model

I performed simulations of single photon responses in the new small model. After the model reduction as described previously, the simulations run rather quickly: on a desktop computer or the computational cluster CARL, I was able to run 100 stochastic simulations of the single photon response within a matter of minutes.

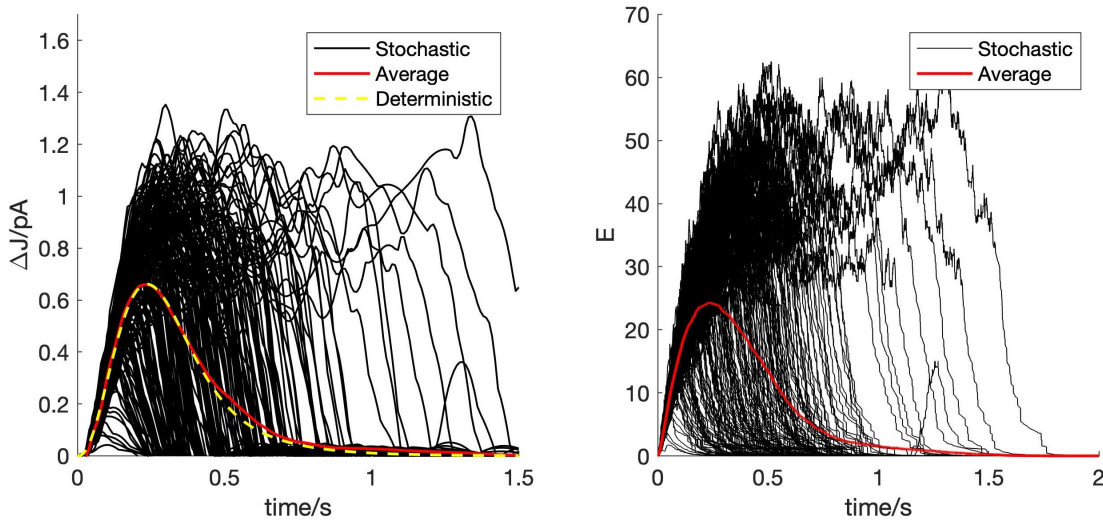


Figure 4.9: Single photon responses in the new small model. On the left, ΔJ resulting from 200 stochastic simulations is shown (black lines), as well as the average of the stochastic simulations (red line) and the result of the deterministic simulation of the single photon response in the small model (dashed yellow line). On the right, the effector is shown for the same simulations (black lines) along with its average (red line).

In figure 4.9, the ΔJ and the effector resulting from 200 stochastic simulations are shown. In the left panel, ΔJ of the stochastic simulations is shown in black lines, along with the average from the stochastic simulations (red lines) and the result from a deterministic simulation of the single photon response in the small model (dashed yellow line). We can see that the average response shape almost completely overlaps with the deterministic result, which is a nice consistency check. The stochastic runs shown some variability, but share a common shape, especially

in the rising phase. However, there are also some responses which have a considerably lower or higher amplitude than the average response. This is investigated further in section 4.6.

The effector in this model now follows the new formulation:

$$E = 0.025 \cdot \text{PDE}^* + {}^*\text{PDE}^*, \quad (4.3)$$

according to the new insight that the single-activated form of the PDE only has 2.5% of the hydrolytic activity on cGMP of the double-activated form. In figure 4.10, we can see how the resulting effector is split into the contributions of the single- and double-activated PDE.

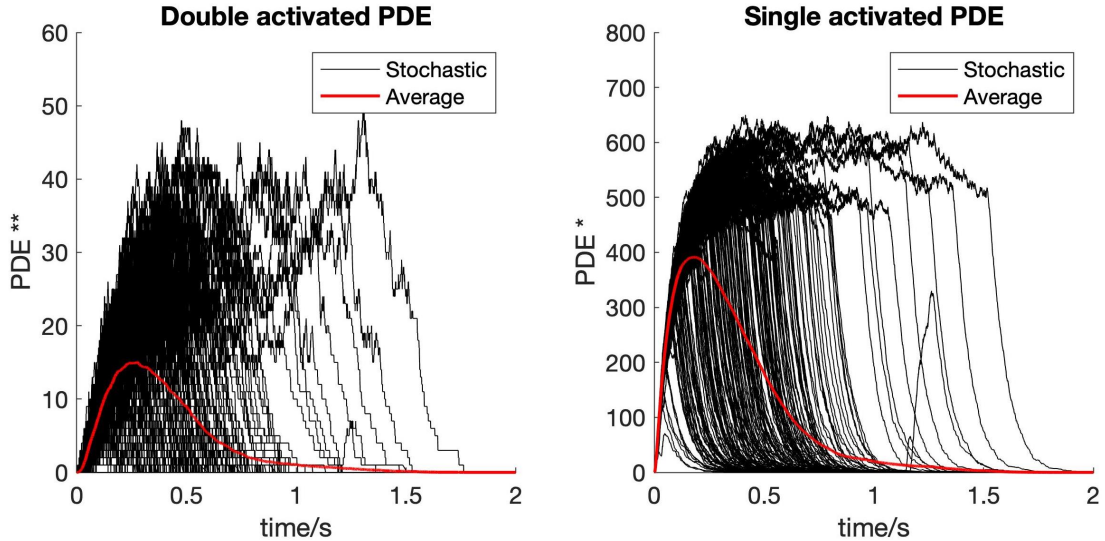


Figure 4.10: Single- and double-activated PDE during single photon responses in the new small model, resulting from 200 stochastic simulations. Each stochastically simulated trace is shown (black lines), as well as the average of the stochastic simulations (red line). On the left is the double-activated PDE and on the right is the single-activated PDE.

The average number of double-activated PDE molecules is now in line with the result of 12-14 activated transducin-PDE complexes from (Yue et al., 2019). To achieve this number of double-activated PDE molecules, a high number of single-activated molecules are required in the model (ca. 400, on average). This results in a total effector of about 24.

4.3.2 Different knockout models

We can also do the same benchmark test with the new small stochastic model as for the old stochastic mouse model: simulating single photon responses in different knockout conditions. Thus, I created models with the different genetic modifications based on the small model: knockouts of arrestin, of the rhodopsin kinase, and of the GCAPs, as well as the completely substituted mutant of rhodopsin (CSM), where all phosphorylation sites are substituted. This time, I performed stochastic simulations instead of deterministic simulations and averaged over 100 stochastic simulation runs for each of the conditions. The results are shown in figure 4.11.

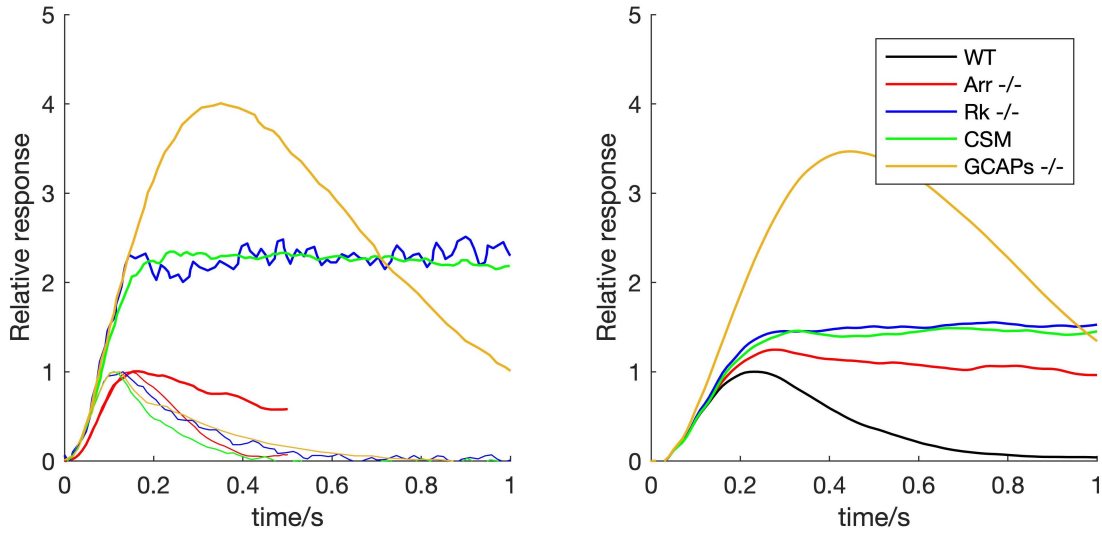


Figure 4.11: Single photon responses in different knockout models. Left: experimental data from mouse rods. Arrestin knockout (Arr $-/-$, red) from (Xu et al., 1997), completely substituted mutant (CSM, green) from (Mendez et al., 2000), GCAPs knockout (GCAPs $-/-$, yellow) from (Burns et al., 2002), rhodopsin kinase knockout (RK $-/-$, blue) from (Chen et al., 1999). The respective wild type responses are plotted in matching colors with a thinner line, and all responses have been normalized to a maximum wild type amplitude of 1 pA. The arrestin knockout response has been scaled to the same amplitude as the wild type response. Right: stochastically simulated single photon responses in models with the respective knockouts: arrestin (Arr $-/-$, red), GCAPs (GCAPs $-/-$, yellow), rhodopsin kinase (RK $-/-$, blue) and the completely substituted mutant (CSM, green) as well as the wild type (WT, black). Each trace corresponds to the average over 100 stochastically simulated single photon responses. All responses have been scaled with the amplitude of the wild type response.

We can observe the same behaviour in the results from the new small model as in the mouse model in figure 4.6. The general changes in kinetics are well reproduced, but there is a discrepancy for the arrestin knockout. For a further discussion of

the different knockout models, see the results for the mouse model in section 4.2.2. The possible reasons for the discrepancy for the arrestin knockout are discussed in chapter 5.

Since the behaviour of the model with the presented genetic modifications has not changed, we can verify that the changes in the new small model have not disturbed the general kinetics and the role of the different elements of the cascade.

4.4 Comparison to novel electrophysiological data

Our collaborators in Pisa, Sabrina Asteriti and Lorenzo Cangiano, performed electrophysiological recordings of dim light responses in single mouse rods within whole retina mounts. My aim was to compare these novel electrophysiological results to my simulated data.

4.4.1 Categorization of the dim flash responses

First, I needed to categorize the recorded dim light responses into failures to respond, single photon responses and multiple photon responses. Due to the quantized, stochastic nature of the light when we approach single-photon intensities, it is difficult to reliably deliver one photon to the rod for each recording. The result of the measurements is thus a mixture of failures, where no photon was absorbed, single photon responses, and multiple photon responses, where more than one photon was absorbed in the rod.

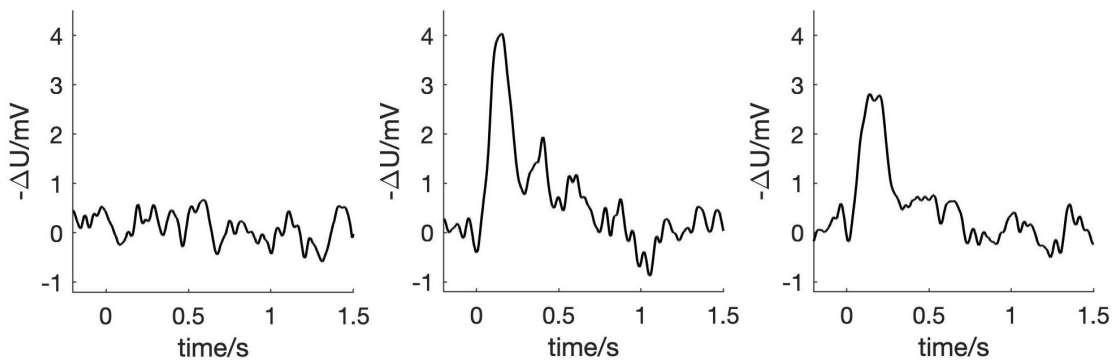


Figure 4.12: Three examples of the electrophysiologically recorded dim light responses. The responses are measured in terms of photovoltage, ΔU .

In figure 4.12, I show some examples of the dim light responses. They are measured in terms of the photovoltage, ΔU , like the bright light responses in section

4.4. COMPARISON TO NOVEL ELECTROPHYSIOLOGICAL DATA

3.3. The stimulus is delivered at $t = 0$ s. The responses we see in the example figure could be a failure to respond (left), a multiple photon response (middle), and a single photon response (right) - but to make a less subjective and more quantitative categorization, we cannot rely on our impression alone. Instead, we use a more systematic method of categorizing the responses.

To categorize the responses, we sort them by their rising phases. The rising phase of the single photon response is especially reproducible, much more so than the shut-off. The procedure is explained, among others, in (Hamer et al., 2005) and references therein. After briefly explaining the procedure, I will go through it step by step with images. First, we compute the mean response from all recordings - please note that this is not the mean single photon response, since the failures to respond and multiple photon responses are still included. Then, we scale the mean response to each recording separately, calculating the scaling factor that yields the best fit during the rising phase. This gives us a scaling factor for each response. We plot all scaling factors in a histogram, fit a sum of Gaussians to the histogram, and compute the intersections - this will then give us the cut-off scaling factors between which the single photon responses lie.

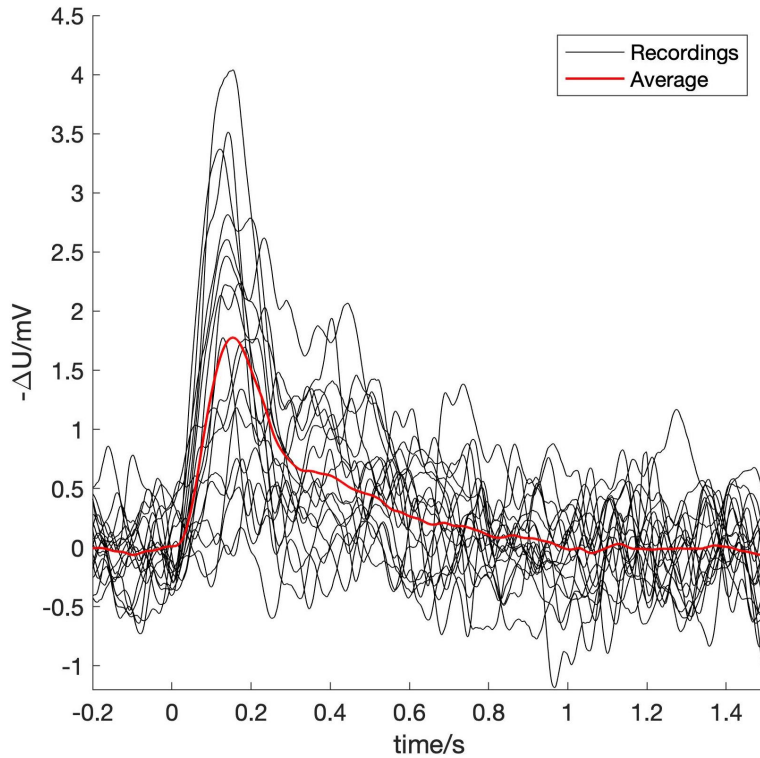


Figure 4.13: A few examples of dim flash responses (black lines) and the mean (red line) of the entire dataset of recordings (which contains 173 recordings).

CHAPTER 4. STOCHASTIC MODELLING

The first step is to compute the mean response. This is shown in figure 4.13: the mean of all 173 recordings in the dataset (cell1200112) as well as a few example recordings.

The next step is to scale the mean to each of the recordings. We can calculate the optimal scaling factor S yielding the best fit over the rising phase of the response as follows:

$$S = \frac{\sum_{i=a}^b m(i) \cdot x(i)}{\sum_{i=a}^b m(i) \cdot m(i)}, \quad (4.4)$$

where $m(i)$ is the mean response, $x(i)$ is the individual recording, a is the start of the stimulus, and b is the peak of the mean response, which is where the rising phase ends. This gives us the scaling factor S calculated over the rising phase for each of the individual recordings. Some example responses with their corresponding scaled mean response can be found in figure 4.14. These are the same responses as in figure 4.12.

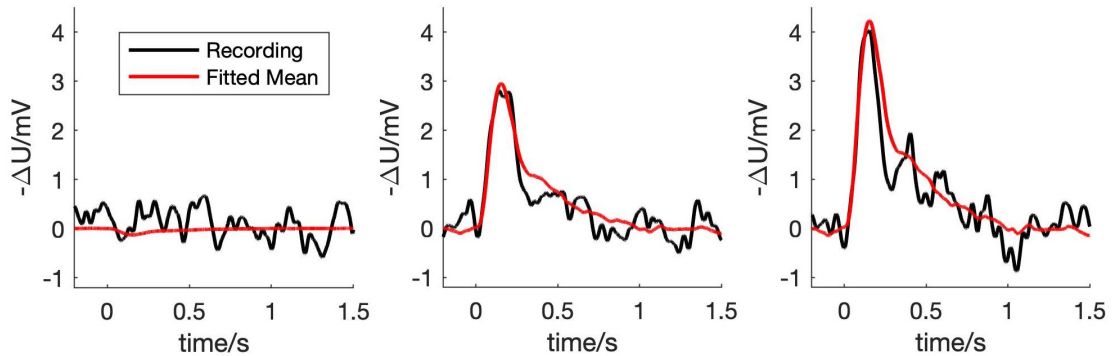


Figure 4.14: Three individual electrophysiologically recorded dim light responses (black lines), as well as the scaled mean (red lines) to each of them.

The next step in the procedure is to create a histogram of the scaling factors produced by the fitting procedure. These scaling factors are a comparable measure to the amplitude, but better: they are connected to the timing of the stimulus and the response. We will next use the scaling factors to categorize the responses, but first we need to find out where to set the cut-off scaling factors between failures, single photon responses and multiple photon responses. For this we use the histogram, shown in figure 4.15.

4.4. COMPARISON TO NOVEL ELECTROPHYSIOLOGICAL DATA

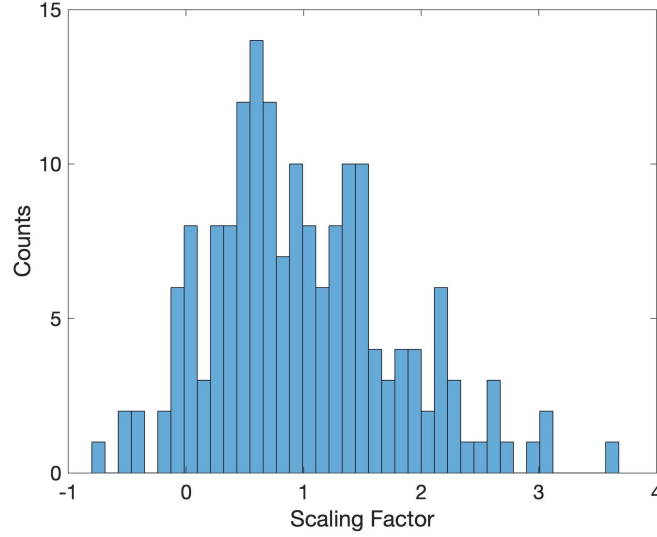


Figure 4.15: Histogram of the scaling factors for the individual responses, determined by scaling the mean response to create the best fit to each response.

In the histogram, we can see that the scaling factors are not uniformly distributed, but grouped into different peaks. One peak is centered around a scaling factor of zero - these are the failures. The next peak centered around 0.7 are the single photon responses. The peaks around larger values for the scaling factor correspond to multiple photon responses.

To quantitatively determine where to place the borders between the different categories, we fit a sum of Gaussians function to the histogram:

$$f(S) = \sum_i \frac{c_i}{\sigma_i} \cdot e^{-\frac{1}{2} \left(\frac{S - \mu_i}{\sigma_i} \right)^2}, \quad (4.5)$$

where i is the amount of Gaussians required for a good fit (corresponding to the amount of peaks), c_i is a normalization factor, μ_i the mean and σ_i the standard deviation, respectively for the i -th Gaussian. By defining this function in MATLAB and inputting starting guesses for the parameters c_i , μ_i and σ , we can use the function `fitnlm` to fit the function to the histogram. We can see the fit as well as the histogram in figure 4.16.

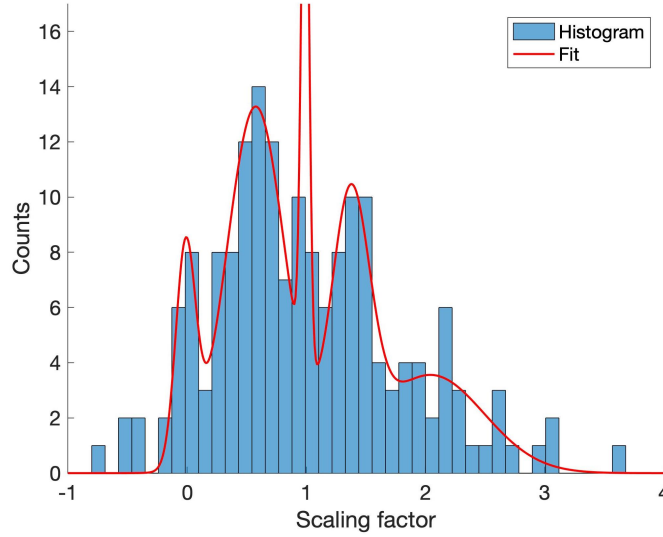


Figure 4.16: Histogram of the scaling factors for the individual responses with a fit of a sum of Gaussians function.

The fit consists of five separate Gaussians, so that the peaks for higher scaling factors are lumped in one peak. But this does not matter: we are interested in the intersections between the first three Gaussians, which will give us the borders for the scaling factors to differentiate between failures, single photon responses and multiple photon responses. The intersection between the first and second Gaussian yields the cut-off scaling factor for failures S_F : responses with smaller scaling factors are categorized as failures to respond. The intersection between the second and third Gaussian yields the cut-off scaling factor S_{SPR} for single photon responses: responses with scaling factors between S_F and S_{SPR} are categorized as single photon responses. All responses with larger scaling factors are categorized as multiple photon responses.

This procedure is quite delicate for noisy recordings. The electrophysiologically recorded responses had been boxcar-filtered, which is a quite strong filtering, when I first received them and started the categorization procedure. By calculating the scaling factor for the rising phase and making the histogram categorization, I achieved categorization results for two out of the total 6 files with recordings. Later, we revised the filtering once again and tried the same procedure with less strongly filtered data (using a Gaussian filter). However, this was not successful since the data was too noisy to clearly separate into groups in the histogram.

The method is often used to categorize dim flash responses, but it does have one disadvantage: particularly small single photon responses may be categorized

4.4. COMPARISON TO NOVEL ELECTROPHYSIOLOGICAL DATA

as failures, and particularly large single photon may be categorized as multiple photon responses. This leads to an underestimation of the variability of the single photon responses, as I show in section 4.6.

4.4.2 Conversion of photovoltage to photocurrent

After doing the categorization for the datasets `cell200112` and `cell200111`, we ended up with 91 single photon responses, 89 failures to respond, and 126 multiple photon responses. In order to compare the experimental data to the simulated single photon responses, we first converted the responses from the photovoltage, ΔU to photocurrent, ΔJ .

For the conversion, I used the frequency-dependent complex impedance $Z(f)$ of the rod cells, as recorded by Sabrina Asteriti and Lorenzo Cangiano. Briefly explained, the time-domain signals of ΔU were Fourier transformed to the frequency domain, where they were multiplied with $1/Z(f)$ to arrive at the frequency domain representation of ΔJ . This was Fourier transformed again to go back to the time domain.

The complex resistance was measured by injecting a sinusoidal current stimulus with exponentially varying amplitude into the cell and measuring the resulting ΔU (Cangiano et al., 2007). The rod impedance was then fitted to a model impedance of a neuron expressing a time-dependent negative feedback conductance with a single time constant, given by

$$Z(f) = \frac{1}{g_{\text{leak}} + 2\pi i f c_m + g_{\text{neg}}(1 + H)}, \quad (4.6)$$

with the membrane passive leakage conductance g_{leak} , the membrane capacitance c_m , the steady state value g_{neg} of the negative feedback conductance, and

$$H = \frac{\hat{g}}{1 + 2\pi i f \tau}, \quad (4.7)$$

with the deviance \hat{g} from the Ohmic behaviour of the negative feedback conductance and the time constant τ of the negative feedback conductance.

Having fitted this model to the response, we arrived at a model of the frequency-dependent complex impedance $Z(f)$. I then used it to convert the photovoltage to photocurrent by dividing by $Z(f)$ in the frequency domain. To get to the frequency domain, I Fourier transformed the signals. For this I used MATLAB's fast

Fourier transform function `fft`, which can be used to Fourier transform discrete time signals to the frequency domain. In the frequency domain, I divided by the complex impedance, making sure to properly deal with the real and imaginary parts of the signal.

This yields the frequency-domain $\Delta J(f)$, which I subsequently transformed back to the time domain. For this I used MATLAB's inverse fast Fourier transform `ifft`. The output was $\Delta J(t)$, the time domain photocurrent.

The entire conversion is carried out by the script `conversionscript.m`, which I wrote: the input arguments are the time and photovoltage to be converted, and the output is the converted photocurrent.

Since the fast Fourier transform leads to some signal artefacts at the beginning and the end of the signal, I had to make sure to exclude these parts of the signal from any subsequent analyses. Also, the conversion amplifies high frequency noise, which is why I lowpass-filtered the photocurrent after the conversion using MATLAB's function `lowpass` with a passband frequency of 40 Hz.

4.4.3 Results and comparison to simulations

The electrophysiologically recorded single photon responses, identified by categorization with the histogram method and converted to photocurrent, are shown in figure [4.17](#).

In the figure, I scaled the responses of both data sets separately to an average single photon response of 1 and then pooled the responses from both data sets. We can see that the average failure response is flat, which is a good proof of principle that the categorization worked out well in terms of differentiating between responses and failures to respond. The single photon responses are quite variable, but follow a common shape.

4.4. COMPARISON TO NOVEL ELECTROPHYSIOLOGICAL DATA

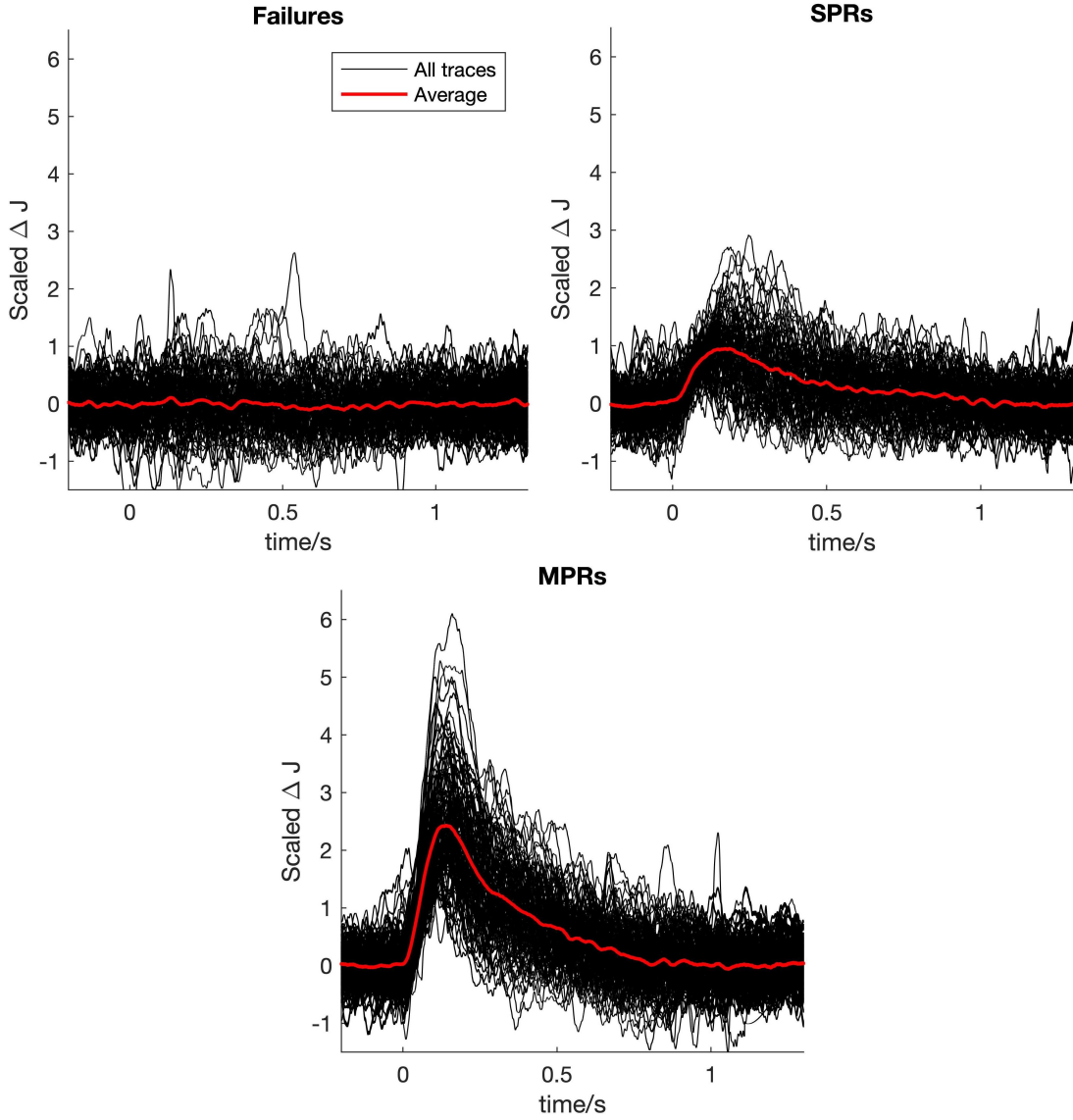


Figure 4.17: The categorized photocurrent responses: upper left, failures to respond; upper right, single photon responses; and lower plot, multiple photon responses. The individual traces are shown in black, with their average in red.

As a first comparison between simulations and experiment, I compared the average single photon response from the electrophysiological recordings to the average simulated single photon response from the stochastic simulations, see figure 4.18.

Comparing the average responses, they look quite similar in general shape, the rising phase and the shut-off. When doing a more quantitative comparison, we noticed that the simulated single photon responses are a little slower in the rising phase: for the experimental responses, the time to peak is $t_{\text{TTP}} = 0.19 \text{ s}$, while for the simulated responses, $t_{\text{TTP}} = 0.24 \text{ s}$.

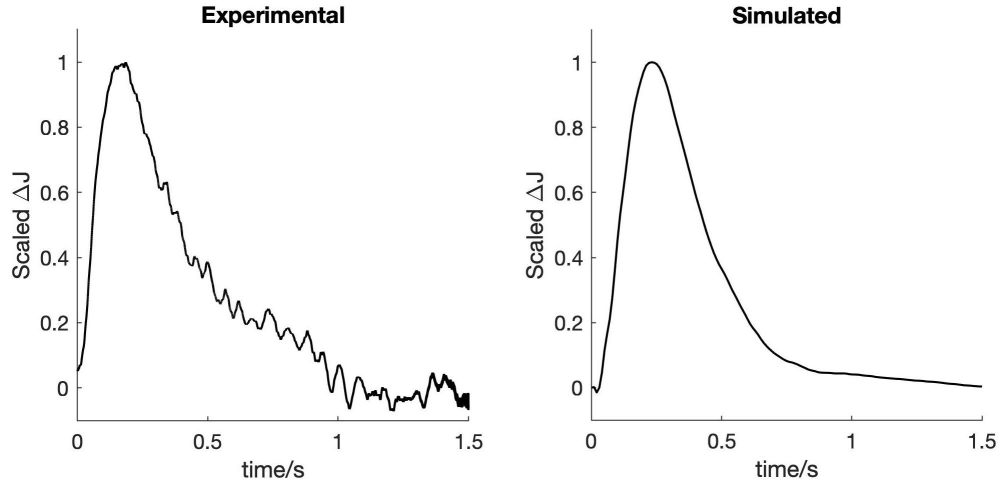


Figure 4.18: Side by side comparison of the average single photon response resulting from the categorized experimental dim flash responses, left, and from the stochastically simulated single photon responses, right. Both averages were scaled to an amplitude of 1.

I investigated the origin of this delay more closely and found that it arises in the activation of the PDE. Unfortunately, it was not easily fixed by adapting any parameters. Specifically, it arises in the step of the activation of the PDE from $\text{PDE} \cdot \text{G}_{\alpha\text{GTP}}$ to $\text{PDE}^* \cdot \text{G}_{\alpha\text{GTP}}$ and the further steps towards the double activation of the PDE, as can be seen in figure 4.19.

In the figure, I plotted the normalized molecule numbers of the different species between the activated transducin and the double-activated PDE. We can see that $\text{G}_{\alpha\text{GTP}}$ and $\text{PDE} \cdot \text{G}_{\alpha\text{GTP}}$ reach their peak rapidly, within 0.05 s after the activation of rhodopsin. Thus, the G-protein is rapidly activated and rapidly associates with the PDE. Next, the single-activated form $\text{PDE}^* \cdot \text{G}_{\alpha\text{GTP}}$ reaches its peak at 0.21 s. Thus, it is the activation step of the PDE that introduces a delay.

The same counts for the double-activated form: the pre-complex reaches its peak at 0.15 s, while the double-activated form only peaks at 0.26 s. Since the effector is made up from both the single-activated and the double-activated form of the PDE, its peak lies in between the single- and double-activated maxima, at 0.24 s.

I tried to change the rate of the activation step, but this did not decrease the delay. To be clear, the delay in itself is not a problem, since the electrophysiological response has its maximum at 0.19 s. Thus, it is fine that a delay is introduced in the activation step, it is just slightly too large.

4.4. COMPARISON TO NOVEL ELECTROPHYSIOLOGICAL DATA

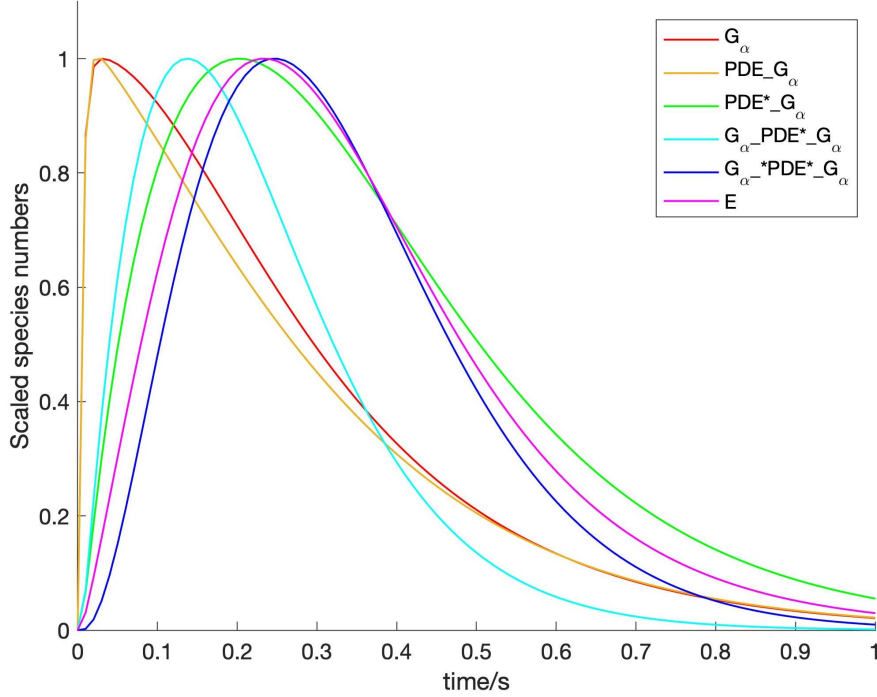


Figure 4.19: Scaled species numbers for different steps in the activation of the PDE during the single photon response, resulting from a deterministic simulation. In the order of activation, the species are $G_{\alpha\text{GTP}}$ (red), $\text{PDE} \cdot G_{\alpha\text{GTP}}$ (yellow), $\text{PDE}^* \cdot G_{\alpha\text{GTP}}$ (green), $G_{\alpha\text{GTP}} \cdot \text{PDE}^* \cdot G_{\alpha\text{GTP}}$ (light blue), $G_{\alpha\text{GTP}} \cdot \text{PDE}^* \cdot G_{\alpha\text{GTP}}$ (blue), as well as the total effector E (magenta).

I also tried to remove the activation step altogether by assuming that the PDE is immediately activated upon binding of the G-protein. However, this also did not significantly decrease the delay: it was then between the single- and double-activated form of the PDE.

The delay could be an artefact of the fact that we do not perform space-resolved simulations, where the activation step would be much faster than the other rates, since it does not require any diffusion. However, though this time-to-peak may be at the upper limit of measured time-to-peaks, it is not completely unrealistic (Cangiano et al., 2012).

Next, let us take a look at the statistical properties of the single photon responses. Typically, the variability of the responses is quantified by computing the coefficient of variation of their amplitudes and the areas:

$$CV = \frac{\sigma}{\mu}, \quad (4.8)$$

with the mean μ and the standard deviation σ , which is the square root of the variance: $\sigma = \sqrt{v}$. Both the mean and the standard deviation are computed for all areas and amplitudes of the single photon responses, respectively.

Before computing the standard deviation from the variance, the variance of the failures is subtracted. This is to quantify the variance arising from just the single photon responses, and to subtract that resulting from dark noise and measurement noise.

For the electrophysiological responses, I computed the coefficients of variability over a duration of 1.5s after the stimulus. This yielded $CV_{\text{area}} = 0.37$ and $CV_{\text{amp}} = 0.23$, which is in line with previously computed values (Hamer et al., 2005).

For the simulated single photon responses, I calculated the coefficients of variability over the same duration of 1.5s after the stimulus. This resulted in $CV_{\text{area}} = 0.87$ and $CV_{\text{amp}} = 0.34$. The CV of the amplitude is well reproduced by the simulations, but the CV of the area is quite high in comparison.

This could be due to several reasons: the shut-off of rhodopsin could be responsible, or a missing shut-off mechanism on the effector, or it could be an effect of the categorization of the responses, which will be investigated in section 4.6. A more detailed discussion of the difference between the measured and simulated CV of the area can be found in chapter 5.

I checked an effect that could have an influence on the calculated CV: the variance of the amplitude and area of the dark noise, which is subtracted from the experimental recordings. In the simulations, there is no dark noise or measurement noise, which is why we do not need to subtract it. This could however lead to a larger CV, since the subtraction of dark noise reduces the variance for the experimental recordings. To test this last hypothesis, I tried adding dark noise from the experimental traces to the simulated data. This did not lead to any conclusive results, however: the CV was not significantly changed (data not shown).

4.5 Precoupling

In this section, we are investigating the effect of the precoupling on the single photon response. The effect is described in detail in section 1.1.5.

To investigate the effect of precoupling, I changed the initial condition in the

stochastic model from one activated (single) rhodopsin to one activated rhodopsin-transducin complex. Then, I investigated the resulting single photon responses from deterministic and stochastic simulations.

For a first investigation, I carried out a deterministic simulation of the single photon response with the two different initial conditions. The result can be found in figure 4.20.

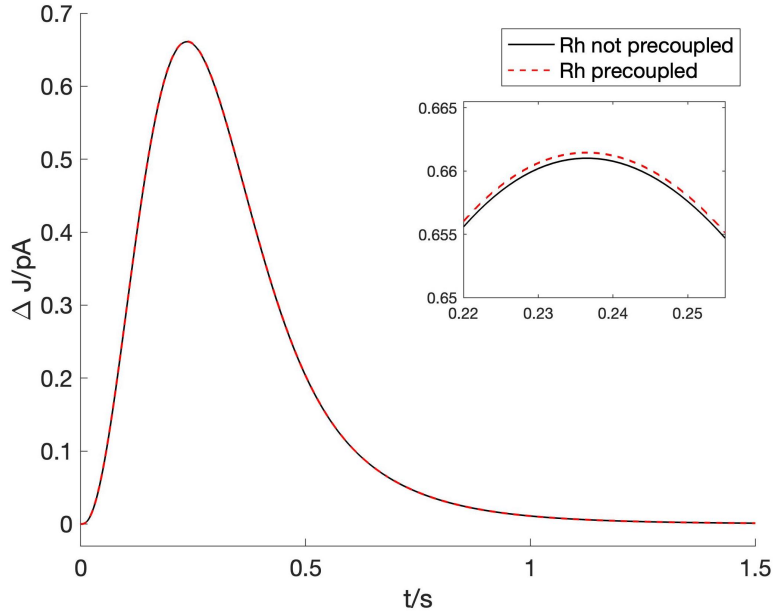


Figure 4.20: Comparison of the photocurrent resulting from deterministic simulations of the single photon response with two different initial conditions: an activated single rhodopsin (solid black line) or an activated precoupled rhodopsin-transducin complex (dashed red line). The inset shows a zoom on the peak of the response.

In the figure, we can see that the photocurrent appears to be almost equal for the two different initial conditions. Only in the zoom in the inset do we recognize that the trace resulting from the precoupled rhodopsin reaches a very slightly higher amplitude.

Why is this the case? We could assume that the precoupling would result in a higher amplitude or a lower time to peak - after all, the rhodopsin starts out already associated to a G-protein, which accelerates the response. Without precoupling, the first G-protein has to associate with rhodopsin before it can be activated. However, when we take a look at the trace for the activated G-protein in figure 4.21, we realize that this does not have a large effect.

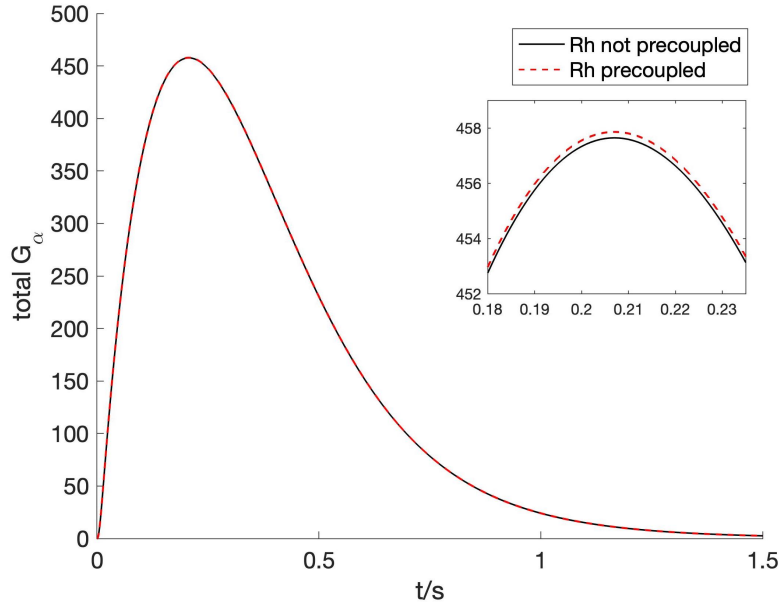


Figure 4.21: Comparison of the total activated G-protein $G_{\alpha GTP}$ resulting from deterministic simulations of the single photon response with two different initial conditions: an activated single rhodopsin (solid black line) or an activated pre-coupled rhodopsin-transducin complex (dashed red line). The inset shows a zoom on the peak. The total $G_{\alpha GTP}$ consists of all free $G_{\alpha GTP}$ as well as that bound to PDE.

The total amount of activated G-protein peaks at around 458 G-proteins in this model, so one single activated G-protein cannot make a large difference. Furthermore, the activation of the G-protein starts very rapidly, so the time advantage of rhodopsin already being associated with a G-protein does not have a big impact. We can also see this when we look at the amount of rhodopsin bound to G-protein in figure 4.22.

In the figure, the amount of unphosphorylated activated rhodopsin bound to transducin is plotted for the first 0.1 s of the single photon response. For the precoupled initial condition, this is the molecular species that is activated as an initial condition, which is why it starts at 1 for $t = 0$ s. Without precoupling, $R_0 = 1$ is the initial condition and binding to Gt occurs next, as a the first step in the activation of the G-protein. Thus, at $t = 0$ s the trace for the non-precoupled condition starts at 0 and starts to rise.

From this state, the exchange of GDP to GTP is the next step - thus, the amount of $R_0 \cdot Gt$ decreases. Since this is a deterministic simulation, we see molecule numbers smaller than one, since they represent the equivalent of an average molecule number over many stochastic simulations.

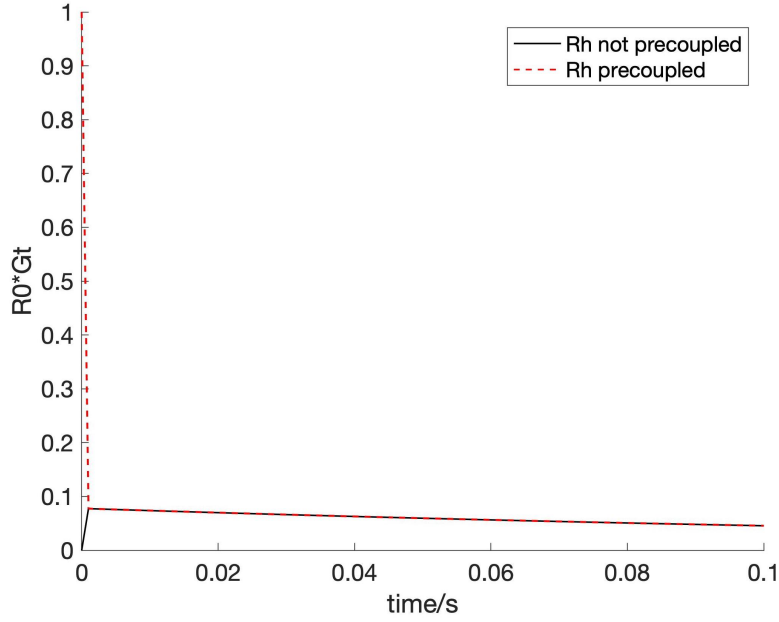


Figure 4.22: Comparison of the amount of activated, non-phosphorylated rhodopsin associated to Gt resulting from deterministic simulations of the single photon response with two different initial conditions: an activated single rhodopsin (solid black line) or an activated precoupled rhodopsin-transducin complex (dashed red line).

In figure 4.22, we can see that the traces for the precoupled and non-precoupled initial condition start at different points, but within one simulation step of 1 ms, they overlap and follow the same trace. This shows that the effect and the advantage of the precoupling basically vanishes after one simulation step in the model.

Thus, the precoupling does not have a large effect in the deterministic simulations. However, it could still have an effect on the reproducibility of the responses. To investigate this, I performed stochastic simulations. As the stochastic simulations introduce a lot of variability, it is important to be careful about making quick conclusions from a small number of simulations when comparing the two initial conditions.

In figure 4.23, the average single photon responses resulting from 1000 stochastic simulations each are compared for precoupled- and non-precoupled activated rhodopsin as the initial condition.

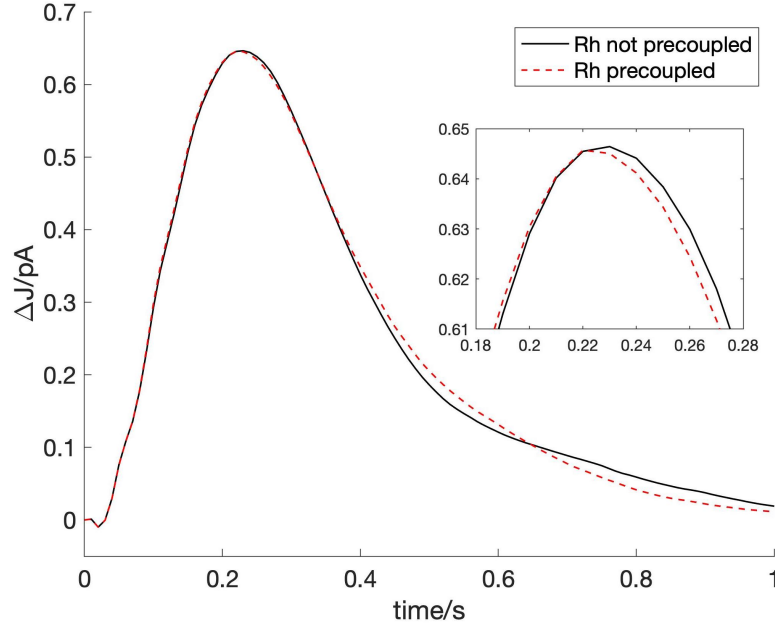


Figure 4.23: Comparison of the average photocurrent each resulting from 1000 stochastic simulations of the single photon response with two different initial conditions: an activated single rhodopsin (solid black line) or an activated precoupled rhodopsin-transducin complex (red dashed line). The inset shows a zoom on the peak of the response.

From the figure, we can see that, as we expected, there is not a large difference between the average responses after averaging over sufficiently many stochastic simulation runs. There is only a very small reduction of the time to peak. However, even though the average is almost the same, there might be a difference in the distribution of areas and amplitudes within the ensemble of simulations for the different initial conditions.

We can approximate these distributions by creating histograms of the areas and amplitudes of all 1000 simulated single photon responses. These histograms are shown in figure 4.24. The distributions allow for a better, more detailed comparison than just calculating the CV of the area or the amplitude.

In the figure, we can see that there is a difference between the histograms with and without precoupling. Specifically, the histograms for the precoupled initial condition appear to have a sharper peak. This hints at a higher reproducibility for the single photon responses amplitude and area, since the data are less distributed.

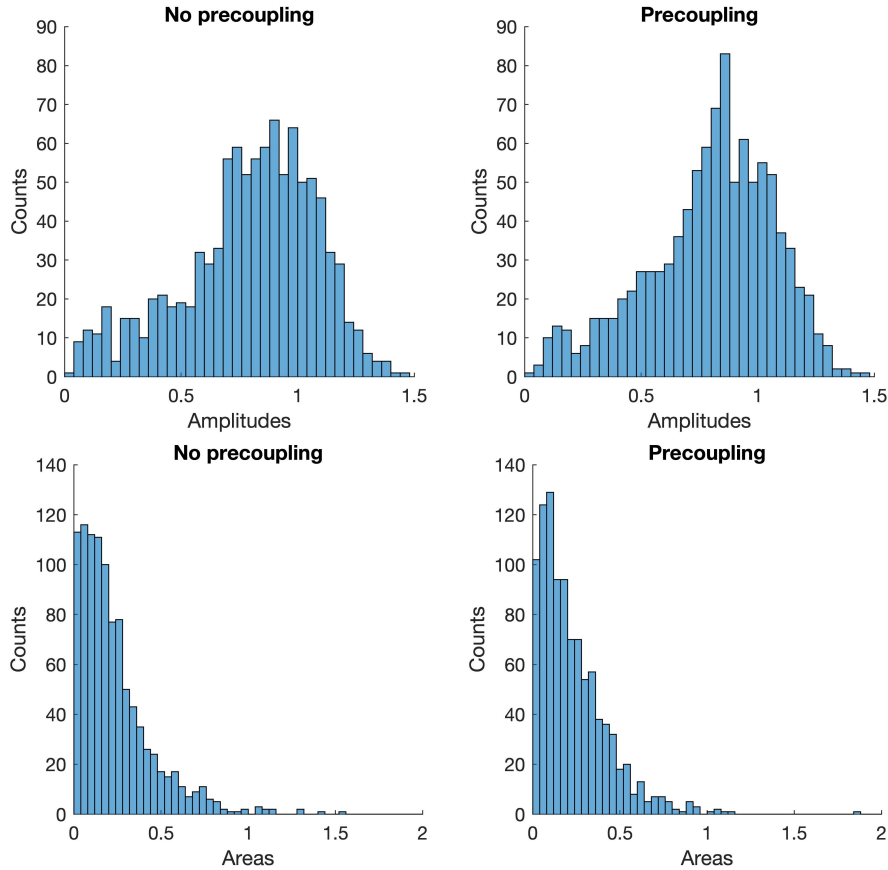


Figure 4.24: Histograms of the single photon response amplitudes (upper row) and areas (lower row), resulting from 1000 stochastic simulations each for two different initial conditions: the activated rhodopsin was precoupled (right) or not (left).

Especially concerning the amplitude, this could be beneficial: as explained in section 1.1.6, single photon responses need to be reliably differentiated from noise by neurons in order to produce a detectable stimulus in the retina. This is probably done by amplitude thresholding (Field and Rieke, 2002). For this, it is important that single photon response amplitudes are large enough to be clearly different from noise.

In the amplitude distributions, we can see that the non-precoupled initial condition produces some single photon responses with amplitudes close to zero. For the precoupled initial condition, there are fewer small responses. Thus, the precoupling could improve the reproducibility and increase the chance of detection of single photon events.

To conclude, we were not able to find a large difference in the average response shape of the single photon response for the two different initial conditions of the

initially activated rhodopsin being precoupled or not. However, with the stochastic simulations we were able to see that there appears to be a difference concerning the distribution of areas and amplitudes of the single photon responses resulting from the different initial conditions. The single photon responses resulting from a precoupled rhodopsin appear to be more reproducible. This result is independent from the assumed ratio of precoupled vs. non-precoupled rhodopsin molecules, since the two different initial conditions are directly compared.

4.6 Random initial conditions

In this section, we are investigating random initial conditions for the stochastic simulations and their consequences on single photon response variability. We do this to achieve results that are more comparable to the experimental situation: In the electrophysiological recordings, we have a mixture of single photon responses, failures, and multiple photon responses, with no direct way of knowing which responses arose from a single rhodopsin activation. Therefore, we categorize the responses by their response shape. This may lead to an underestimation of the variability of single photon response, since we could be categorizing particularly small single photon responses as failures to respond and particularly large single photon responses as multiple photon responses.

To check whether this is true, we recreated the initial conditions of the experiment more realistically in the simulations. In reality, when dim flashes are delivered, the amount of delivered photons follows a Poisson distribution:

$$P_{\lambda}(k) = \frac{\lambda^k}{k!} e^{-\lambda}, \quad (4.9)$$

where $P_{\lambda}(k)$ gives the probability of drawing the integer number k from a Poisson distribution with the expected value λ . In our case, k corresponds to the number of absorbed photons and thus activated rhodopsin molecules. The Poisson distribution for $\lambda = 1, 2$ and 4 is shown in figure [4.25](#).

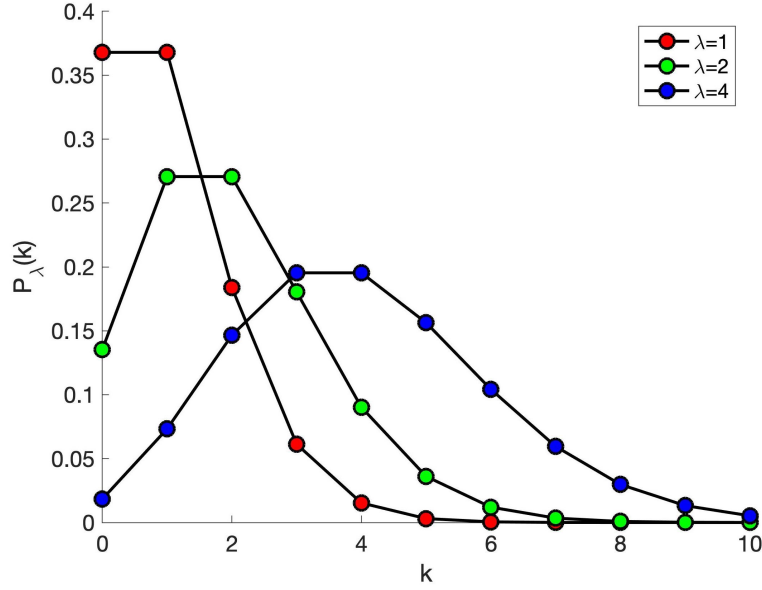


Figure 4.25: The Poisson distribution $P_\lambda(k)$ for $\lambda = 1$ (red symbols), 2 (green symbols) and 4 (blue symbols).

As an initial condition of the simulations, we draw a random number from a Poisson distribution for the number of activated rhodopsin molecules. λ can be chosen to set the ratio between failures, single photon responses and multiple photon responses, as it is also the expected value for the number of activated rhodopsin molecules.

Furthermore, we wanted the activated rhodopsin to represent a mixture of precoupled and non-precoupled molecules, as would also be the case in an experiment. For this I thought of an algorithm to choose the total number of activated rhodopsin molecules and decide whether they are precoupled or not, which is shown as pseudocode below:

```

set  $\lambda = 1$ 
set  $P_{\text{prec}} = 0.018$ 
for i=1 to number of simulations
    set R0 = 0
    set R0_Gt = 0
    num_act = poissrnd( $\lambda$ )
    for j=1 to num_act
        rnd = rand
        if rnd <  $P_{\text{prec}}$ 
            increase R0_Gt by 1

```

```

        else
            increase R0 by 1
        end
    end
end
for k=1 to R0_Gt
    do simulation with precoupled rhodopsin
end
for l=1 to R0
    do simulation with non-precoupled rhodopsin
end
sum effector from all simulations in this step
end

```

In the first **for**-loop, the total number `num_act` of activated rhodopsin molecules is chosen as a random Poisson number using MATLAB's function `poissrnd`. Then, in the next **for**-loop, the algorithm loops through all activated rhodopsin molecules and decides whether they are precoupled to transducin or not. These decisions are independent of each other.

For each of the activated molecules, they are precoupled with a probability of P_{prec} , which is set to 0.018. This is the ratio of precoupled rhodopsin molecules to the total amount of rhodopsin in the dark in the model. It corresponds to about 18% of the G-proteins being precoupled to rhodopsin, which is a lower limit. The factor of 10 comes from the ratio of 1:10 of G-protein to rhodopsin molecules.

The decision whether the activated rhodopsin is precoupled is realized by creating a random number uniformly distributed between 0 and 1 using `rand`. If the random number is smaller than P_{prec} , the rhodopsin is precoupled - this is exactly the case with a probability of 0.018. Otherwise, the activated rhodopsin is not precoupled.

The numbers of precoupled and non-precoupled rhodopsin in this simulation step, `R0` and `R0_Gt`, are kept track of. After having looped through all activated molecules, we can now carry out the simulation.

Since the activated rhodopsin molecules are located in different discs with a very high probability, we perform a separate simulation for each activated molecule, using the small model. This is done in the last two **for**-loops: we loop through the number of activated precoupled rhodopsin `R0_Gt` and the number of activated non-precoupled rhodopsin `R0` and do a simulation with the appropriate initial condition `R0_Gt=1` or `R0=1`.

4.6. RANDOM INITIAL CONDITIONS

As a last step, the effector from all simulations of this iteration is added together. Thus, we end up with the total effector resulting from a Poisson number of activated rhodopsins that are a mixture of precoupled and non-precoupled.

Of course, I also save the numbers of activated rhodopsin molecules - this means that we can later recall which responses are true failures to respond, true single photon responses with one activated rhodopsin, and true multiple photon responses with more than one activated rhodopsin.

Finally, the summed effector for each of the simulations is converted to photocurrent ΔJ by inputting it into the backend model.

In figure 4.26, I show the single and multiple photon responses resulting from a simulation of 200 dim flash responses with randomized initial conditions with $\lambda = 1$. The responses are categorized according to the true number of activated rhodopsin molecules.

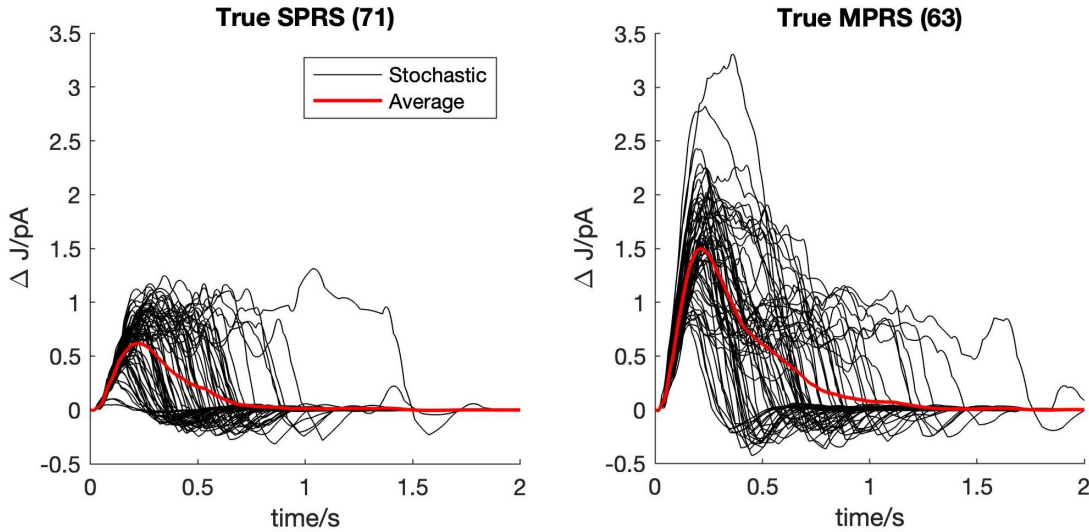


Figure 4.26: Single and multiple photon responses resulting from a simulation with random initial conditions. Failures are not shown, since they are flat lines. The simulation of 200 dim flashes resulted in 66 true failures, with no activated rhodopsin, 71 true single photon responses with one activated rhodopsin, and 63 true multiple photon responses with more than one activated rhodopsin. The individual responses are shown in black and their average in red.

The failures have not been plotted in the figure: they are just flat lines as we do not simulate any dark noise. We can see that there are a few very small single photon responses in the left plot of figure 4.26, and a few multiple photon responses that are close to the typical single photon response amplitude in the right plot.

Next, I investigated what happened when I categorized the responses without using my prior knowledge of the initial conditions. I used the histogram method and proceeded in exactly the same way as for the electrophysiological recordings. The result of the categorization can be found in figure 4.27.

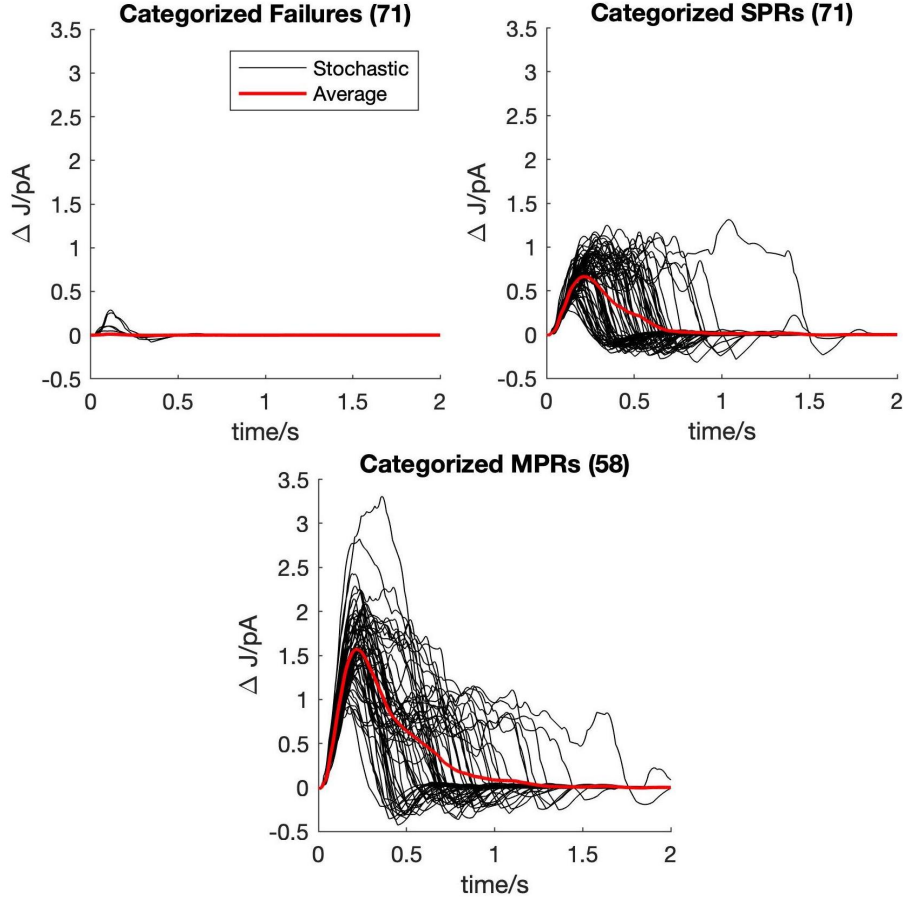


Figure 4.27: Categorized failures, single and multiple photon responses resulting from a simulation with random initial conditions. The categorization of 200 dim flash responses with the histogram method resulted in 71 categorized failures (upper left), 71 categorized single photon responses (upper right), and 58 categorized multiple photon responses (lower plot). The individual responses are shown in black and their average in red.

Interestingly, the categorization led to five true single photon responses being mis-categorized as failures. Furthermore, five true multiple photon responses were mis-categorized as single photon responses. The miscategorized responses are shown in figure 4.28.

In the figure, the responses are shown on the same y-axis as the categorized responses to make a comparison easier. Obviously, the single photon responses that

got miscategorized as failures were particularly small single photon responses. Similarly, the multiple photon responses that got miscategorized as single photon responses were within the upper range of single photon amplitudes, with amplitudes slightly below 1 pA.

The miscategorization has an effect on the variability of the categorized single photon responses. When we calculate the coefficients of variation for the true single photon responses, we arrive at $CV_{\text{amp}} = 0.38$ and $CV_{\text{area}} = 0.93$. However, when we calculate them for the categorized single photon response, they become smaller: $CV_{\text{amp}} = 0.29$ and $CV_{\text{area}} = 0.86$.

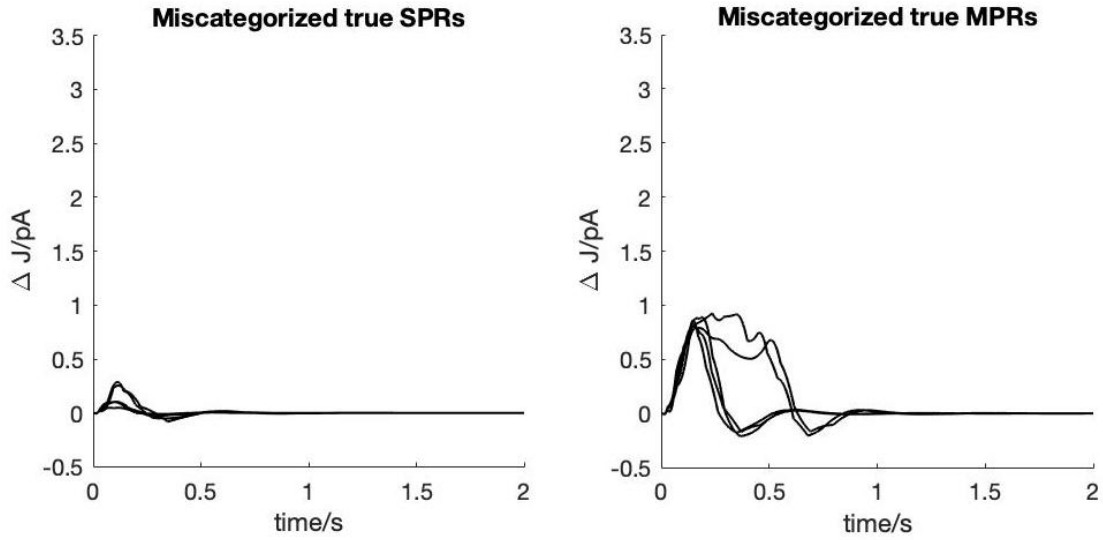


Figure 4.28: Miscategorized single and multiple photon responses resulting from a simulation with random initial conditions. The categorization of 200 dim flash responses with the histogram method resulted in five true single photon responses getting miscategorized as failures (left panel) and five true multiple photon responses getting miscategorized as single photon responses (right panel).

This shows that the method typically used to categorize single photon responses in dim light recordings leads to an underestimation of the true coefficients of variation, since aberrant single and multiple photon responses may be miscategorized. This should be taken into account when comparing, e.g., electrophysiologically recorded single photon responses and simulated single photon responses, and it also has some implications for the mathematical interpretation of the single photon response with its surprisingly low variability.

5 | Discussion

In this chapter, I will discuss the significance of the changes of the models and the new results presented in this thesis.

The type of modelling we chose for the phototransduction cascade was a comprehensive modelling approach based on the biochemical reactions of the cascade. We used mass-action kinetics for the reaction equations, which also includes the well-stirred assumption: the molecular species are equally distributed throughout the reaction volume and there is no spatial dependence. Any change in concentrations or molecule numbers is instantaneous.

The alternative would have been space-resolved simulations. Both approaches have some distinct advantages and disadvantages: The mass-action approach has the disadvantage that space-dependent phenomena, such as diffusion or organized molecular structures, cannot be easily simulated. Furthermore, if we are simulating a local phenomenon in a larger reaction volume, the results will not be accurate since the localized concentrations are spread out over the entire reaction volume, as will be discussed later.

On the other hand, in space-resolved models, simplifications need to be made because of a lack of information about the interacting species or to save computational effort, which is large compared to mass-action based modelling. We do not need to make these simplifications in a mass-action based model and can therefore perform fully explicit simulations of all the relevant interacting species.

This also means that we can perform simulations of conditions equivalent to genetically modified animals by making the same changes in our model. It provides a consistency check for our model: if we are able to reproduce the same results in our experiment, it means that our model faithfully recreates the underlying mechanisms. Furthermore, it can also help to show a potential for improvement of the model: if some effect is not correctly reproduced, this means that the underlying mechanism in the model is not correctly implemented. This could be because the simplifying assumptions of the modelling are incorrect, or because some (unknown) mechanism is still missing in the model.

5.1 Deterministic modelling

The new deterministic model is based on the Invergo 2014 mouse model, with an update of the effector as described in chapter 3. Both the Invergo 2014 model and the new model are able to reproduce many different salient effects of phototransduction in rods: responses to brief flashes of varying intensities, light adaptation phenomena, and altered responses in knockout animals. For the deterministic investigations, I used the Invergo 2014 model and the new model.

5.1.1 Bright light stimuli: Comparison to experiment

First of all, let us discuss the comparison of the new model with the experimentally recorded traces from our collaborators, Sabrina Asteriti and Lorenzo Cagniano from the University of Pisa. The experimental light stimulus consisted of a background with five superimposed flashes of increasing intensities. There were four different background intensities, starting at zero. The flashes ranged from dim to saturating. We developed this stimulus paradigm to investigate brief flash responses, light adaptation and saturation.

As described in section 3.3, I simulated light responses with the same paradigm for comparison to the experimental data. The experimental traces were recorded in ΔU , the change in membrane potential, while the simulated responses are in ΔJ , the photocurrent. Our collaborators measured the complex impedance, but this only allowed us to convert small signals, and the brighter flashes were too bright to be accurately converted. Thus, we compared the experimental results in ΔU to the simulated results in ΔJ . For the dim flash responses discussed later, we did use the conversion procedure.

When we compared the simulated and the experimental data, as shown in figure 3.14, we noticed that the dynamics were qualitatively reproduced: the backgrounds led to a faster response decay for the flashes, which was more pronounced the brighter the background was. However, the simulated responses took longer to shut off. This was also visible when comparing the time spent above half the maximum amplitude, T_{half} : the qualitative reduction of T_{half} by the backgrounds was reproduced, but the T_{half} were generally longer. This discrepancy could have several explanations:

It could be that there are shut-off and light adaptation mechanisms that are not included in the model, such as the action of calmodulin, which regulates the cGMP-sensitivity of the cyclic nucleotide-gated channels. Another light adaptation mech-

anism is the long-term migration of species such as arrestin between the outer and inner segment. This is also not included in the model. Furthermore, there is evidence suggesting that the current picture of phototransduction is lacking a feedback on the level of the effector, as is discussed in section 3.4. This could also be responsible for the observed differences.

Another reason for the difference could be that we are comparing ΔU , the photovoltage, with ΔJ , the photocurrent. We would expect the traces for ΔJ to have a faster rising phase, but a slower shut-off than ΔU , because the rod behaves like a band-pass filter. Thus, the difference between ΔU and ΔJ would be a correction that brings the experimental data closer to the simulated data.

Furthermore, the origin of the model is an amphibian model, which has slower response kinetics. The slower kinetics compared to the experimental data could be a remnant of the origin of the model, which means that more parameters would have to be adapted for a better fit.

Finally, the Invergo 2014 model (on which this model is based) was adapted to fit electrophysiological recordings of flashes in single cells from a chopped retina, while the data presented here are from an intact retina, which could also have an influence on the kinetics.

In summary, the model does reproduce the qualitative features of the responses to the new bright flash paradigm. But there is a discrepancy in the timing of the shut-off of the responses. By further adapting the mechanisms and parameters of the model, it could be possible to bring the results closer together. Furthermore, it is possible to extend the model to also include a simulation of the change in membrane potential, like the modelling done in (Kamiyama et al., 2009). This could help elucidate the differences between photovoltage and photocurrent.

5.1.2 Light adaptation

Because our model is comprehensive, we can study the consequences of the removal of species or mechanisms quite easily. To investigate its significance, I removed a mechanism that is important for light adaptation in section 3.2: the calcium feedback on recoverin and the rhodopsin kinase. The recoverin can undergo a calcium-dependent conformational change: in its calcium-bound form, it can bind to the rhodopsin kinase and prevent it from phosphorylating rhodopsin. When the calcium concentration is decreased as a consequence of the light response, the recoverin releases the rhodopsin kinase, which then phosphorylates rhodopsin - an important first step in the shut-off of the response.

In figures 3.7 and 3.11, we compared the response to a prolonged background and a

saturating stimulus between two different models: the normal model, and a model where this precise calcium feedback mechanism had been removed. In the normal model, light adaptation was apparent: the brighter the background was before the saturating flash, the shorter a time was spent in saturation after the flash. In the model without the calcium feedback, the effect of light adaptation vanished: all curves superimposed during the shut-off, regardless of the background intensity.

This means that the calcium feedback on recoverin and the rhodopsin kinase is essential for light adaptation for the type of light stimuli presented here. The reason is that, during the prolonged background, the feedback leads to the release of more rhodopsin kinase, which is then ready to phosphorylate the rhodopsin activated by the saturating flash and to start the shut-off of the response more rapidly. When we remove the feedback, this mechanism is no longer active: all saturating flashes are terminated with the same kinetics.

This is an example where the modelling helps to elucidate the specific role of a mechanism in the phototransduction cascade. In animal models, it would not be as easy to do the same experiment, but in the simulations we can simply change the reaction equations and examine the consequences.

5.1.3 Hypothesized calcium feedback on the effector

As explained in section 3.4, there is some indirect evidence pointing towards the regulation of the PDE by some additional mechanism in a calcium-dependent way. The rhodopsin kinase and/or recoverin are hypothesized to be responsible for this feedback. The evidence mainly comes from studies of light responses in genetically modified animals (Chen et al., 2012), (Morshedian et al., 2018). However, there is no direct biochemical evidence for an interaction of the rhodopsin kinase or recoverin with the PDE. Furthermore, the interpretation of the results is not straightforward: the results are from rods with a single or double genetic modification, influencing a complex signal transduction cascade with feedback loops. It is not immediately clear that there needs to be a rhodopsin kinase- and recoverin-mediated feedback on the level of the effector.

Therefore, I investigated the same knockout conditions and stimulus paradigms to see if I could reproduce the results with my model. As it stands, the model does not include any additional feedback mechanism of calcium on the PDE. However, we were able to reproduce the light adaptation results by (Morshedian et al., 2018). The main result was that light adaptation was disrupted in recoverin knockout rods. When we knock out the recoverin, we disrupt the calcium feedback on the rhodopsin kinase and thus on the shut-off of rhodopsin. This is sufficient to explain

the observed behaviour.

I furthermore implemented models with a 12-fold overexpression of the rhodopsin kinase and a knockout of the recoverin and compared light responses in these model to the normal model. As shown in figures 3.17 and 3.18, I was able to find the same qualitative effects as in (Chen et al., 2012), again without any additional calcium feedback on the PDE: τ_{Rec} and τ_{D} were decreased in the mutant models compared to the wild type.

From this, I conclude that, at least in our model, the hypothesized additional feedback mechanism is not required to reproduce the presented results. Even though the shut-off of the effector is believed to be rate-limiting in the normal light response, this is not necessarily the case in genetically altered versions of the phototransduction cascade. When the shut-off of rhodopsin is impaired, as is definitely the case when overexpressing the rhodopsin kinase or knocking out recoverin, this can significantly impact the response kinetics even without an additional feedback on the PDE.

A way to extend the modelling to further investigate these effects would be to actually include a calcium-dependent feedback on the PDE and investigate light responses in the resulting model. This could be done by making the rate of the shut-off of PDE (either with or without RGS) dependent on the calcium concentration, the rhodopsin kinase, or the recoverin.

5.1.4 Disease modelling

The model can be used to simulate light responses in disease conditions to find out more about the disease mechanism, if enough biochemical information about the disease is available. We decided to investigate the disease mechanism for retinitis pigmentosa and congenital stationary night blindness. Both diseases originate in the rod cells, but have drastically different consequences: Congenital stationary night blindness is not progressive and only causes night blindness and impaired scotopic vision. Retinitis pigmentosa leads to the successive degeneration of rods and cone cells, and thus to complete blindness. The cause of both diseases are mutations in the phototransduction genes. I studied mutations of rhodopsin that had consequences on the phototransduction cascade to find out more about the precise disease mechanisms in section 3.5.

After a literature review, I decided to study abstractions of the real mutations causing the disease, because they often cause a combination of disturbances in

the cascade. I investigated mutant models with a larger or smaller activation of transducin by activated rhodopsin, with a constitutive activation of the cascade by opsin, and with a lower thermal stability of the activated rhodopsin.

The results showed that light responses were impacted by the different mutations, see figures 3.19 to 3.21. For the mutants with a changed activation of transducin by activated rhodopsin, light responses were equivalent to a higher or lower light level, respectively. Most severely, the mutant with a consecutive activation of the cascade by opsin showed an impacted light response after a bright flash, as the produced opsin continues to activate the cascade. This also leads to disturbed calcium levels in the cell.

For RP patients, the disturbed calcium dynamics could be a significant factor in the degeneration of the cells: since people are rarely in complete darkness, there is always opsin in the rods. For some patients, it has been observed that avoiding bright light conditions may help to slow down the progression of the disease. This could be due to the fact that avoiding bright light also means avoiding the creation of a large amount of opsin in the rod, which would indirectly deregulate the calcium level.

In summary, the model is a useful tool to investigate the consequences of mutations on light responses, if the biochemical consequences of the mutation are known and fall within the scope of the model.

5.2 Stochastic modelling with the old mouse and amphibian model

A main update of the models was the conversion to stochastic models, which can be used to perform stochastic simulations of dim light responses. This is important, because we are interested in single photon response kinetics beyond the average response shape: with deterministic simulations, the only information we get are average kinetics and average molecule numbers of the single photon response. If we want to study, e.g., trial-by-trial variability or amplitude statistics, we need to perform stochastic simulations, which take into account the inherently stochastic and random nature of systems with few interacting molecules.

For the single photon response, the stochasticity is important: one single rhodopsin is activated and randomly shut off by the rhodopsin kinase and arrestin after a random time. During this time, it can thus activate a random amount of G-proteins,

5.2. STOCHASTIC MODELLING WITH THE OLD MOUSE AND AMPHIBIAN MODEL

which in turn activate a random amount of PDE. This results in a slightly different single photon response realization each time a photon is absorbed.

Because the activated molecular species that influence the kinetics of the effector are not very abundant, we need to simulate them stochastically. For the species downstream of the effector, stochasticity is not so important: calcium and cGMP are relatively abundant. Therefore, we split the models into a stochastic frontend and a deterministic backend. We only had to delete one feedback mechanism when doing so, but this had no consequences on the dim light responses we were investigating.

Using the thus created models, we were able to perform stochastic simulations of single photon responses in the amphibian Dell’Orco 2009 model (Dell’Orco et al., 2009) and the mouse model (Invergo et al., 2014). The differences in kinetics between amphibian and mouse were obvious: the single photon responses in the amphibian model were longer and had a larger amplitude. After simulating the first single photon responses, we could use the models for some further investigations.

5.2.1 The role of the phosphorylation sites

For both of the models, I investigated the effect of removing some or all of the available phosphorylation sites on the single photon responses in sections 4.1.1 and 4.2.1. This was studied experimentally in mice in (Doan et al., 2006), and the conclusion was that all phosphorylation sites are important for single photon responses with a low variability. For each removed phosphorylation site, an increase in the variability could be observed. The basic mechanism is that the phosphorylation of rhodopsin decreases its affinity for transducin while increasing the affinity for arrestin, and thus constitutes a multi-step shut-off. This leads to a decrease in variability with each step available for the shut-off.

In our simulations, we were able to see a similar behaviour as (Doan et al., 2006) in the amphibian model, as shown in figure 4.3. The variability of the single photon responses depended on the amount of available phosphorylation sites. Only models with five to six available phosphorylation sites had single photon responses with a normal variability and response duration.

However, when doing the same simulations in the mouse model, we were not able to see the same effect for all phosphorylation sites: only two to three sites are required for a normal variability and response duration, see figure 4.5.

Why is the behaviour of this model so different from the amphibian model? One possibility is the changed dependence of some reaction rates on the phosphorylation state. As described in 2.3.2, rhodopsin’s affinity for transducin, for the rhodopsin kinase, and for arrestin depend on its phosphorylation state, and this dependence has been changed in the transition from the amphibian to the mouse model.

Another factor is the duration of the single photon response. Since the rhodopsin is consecutively phosphorylated several times before the final shut-off, the duration is relevant for the number of phosphorylation sites that are actually occupied during the single photon response. In the amphibian model, I could find runs of the stochastic simulations of single photon responses where rhodopsin was consecutively phosphorylated up to six times. However, in the mouse model, rhodopsin was only very rarely phosphorylated more than two times. Obviously, if the phosphorylation sites are only very rarely used during the single photon response, they cannot contribute much to its variability or kinetics. In the mouse model, the complete shut-off of rhodopsin by arrestin occurs a lot faster than in the amphibian model, and thus the phosphorylation sites have less importance for the shut-off. This effect is investigated more closely in section 4.3, where I removed some of the phosphorylation sites to reduce the model.

To investigate the dependence of the variability of the single photon responses on the number of available phosphorylation sites more quantitatively, it would be possible to perform larger numbers of stochastic simulations and to compute the coefficients of variation. However, this would be quite time-consuming since the models are not reduced yet, unlike the later small version of the mouse model.

5.3 Update of the models and creation of the small model

I attempted to update the mouse model to incorporate two major new insights. The first is that fewer PDE molecules are activated during the single photon response than originally expected, namely 12-14 transducin-PDE complexes instead of ca. 100 (Yue et al., 2019). The second is that the main effector is the double-activated form of the PDE, as the single-activated form has less than 2.5 % of the full activity (Qureshi et al., 2018), (Lamb et al., 2018).

In the deterministic model, I was able to successfully include the first result by

5.3. UPDATE OF THE MODELS AND CREATION OF THE SMALL MODEL

changing one previously adapted parameter governing the activation of the G-protein by rhodopsin, as explained in section 3.1.1. This led to a decrease of the number of activated PDE subunits from 110 to 13 during the single photon response. This change in the model did not significantly impact the kinetics in all stimulus conditions we tested.

However, it was not possible to also include the result that the main effector is the double-activated PDE in the deterministic model. When investigating the composition of the effector in the Invergo 2014 model and the modified model with fewer effector molecules, it became apparent that the effector is basically only made up of single-activated PDE in those models. In the Invergo model, mathematically, one in 10^{12} of the effector molecules is double-activated, and in the modified model, it is one in 10^{13} . However, this is orders of magnitude fewer than one double-activated PDE molecule, and the double-activation would thus never occur in stochastic simulations of the model.

This discrepancy could not be removed by tuning the parameters, as it is due to a general problem with the modelling framework: because we assume a well-stirred volume, the concentrations of all molecules are effectively spread out over the entire reaction volume, which is the entire outer segment. As the concentrations of the single-activated PDE and the activated transducin are multiplied for the rate of the activation of the double-activated PDE, this rate is very low.

Thus, for the deterministic model, we stayed with the modified model with fewer activated PDE models. This model is able to accurately reflect the kinetic behaviour of the phototransduction cascade in many different light conditions and for animals with genetic modifications, it is only inaccurate in its depiction of the exact composition of the effector.

We were able to solve the problem of the double-activated effector for the stochastic simulations by scaling down the model to a smaller reaction volume, as explained in section 4.3. The new small model has a reaction volume of about two discs - this fits to the diffusional range of the molecular species in the frontend of the model, especially those that are constrained to the discs. The backend of the model was not scaled down. Since this model was made for stochastic simulations of single photon responses, we additionally removed a few molecular species and reactions that were not necessary for the single photon responses, such as long-term dimerization and tetramerization of arrestin.

In the thus simplified model, we were able to reach realistic numbers of double-activated PDE molecules after scaling some of the previously adapted parameters.

During the single photon response, typically, 12-14 double-activated PDE and about 450 single-activated PDE are produced. This is now in agreement with the results of (Yue et al., 2019) and (Qureshi et al., 2018), if we assume that the main effector species is the double-activated PDE.

To arrive at this amount of double-activated PDE molecules, a relatively high number of single-activated PDE molecules is required. In the model, we assume that they contribute to the total effector with 2.5 % of the activity of the double-activated PDE, which is the upper bound of the estimate by (Qureshi et al., 2018). We thus arrive at a total effector of ca. 24. This is not unrealistic, especially since the activity of the single-activated PDE could well be lower. However, the high number of single-activated PDE molecules could be an artefact of the modelling framework. In more accurate space-resolved simulations, a comparable number of double-activated PDE molecules is reached with a much lower number of single-activated PDE molecules (Lamb and Kraft, 2020). Still, we decided to stick with our mass-action approach because of its versatility and the fast simulations it allows.

5.4 Results in the small stochastic model

5.4.1 Comparison to electrophysiologically recorded single photon responses

The best test for the stochastic model is a comparison to experimental data. First, however, the experimental recordings have to be categorized: the recordings are a mixture of failures to respond to the stimulus, where no photon was absorbed, single photon responses, and multiple photon responses. This is simply due to the quantized nature of the light at low intensities, and the pure chance of the rod absorbing a photon or not. Since we do not know which traces correspond to which type of response, we need to categorize them first, before we can analyse the single photon responses.

For this categorization, we used the histogram method as described in section 4.4.1. The average response was scaled to each of the individual traces. This scaling factor was then plotted in a histogram, where different peaks could be seen for failures, single photon responses, and multiple photon responses. We then determined the border scaling factors between the types of responses by fitting a sum of Gaussians function to the histogram.

5.4. RESULTS IN THE SMALL STOCHASTIC MODEL

After categorizing the experimental recordings, we can do two main types of comparisons. First, we can compare the properties of the *average* single photon response. These are for example the response shape and quantitative measures like the time to peak. When we compared the average electrophysiologically recorded single photon response to the average of the simulations in figure 4.18, we were able to reproduce the general response shape well. However, the time to peak is larger: $t_{\text{TTP}} = 0.19\text{ s}$ for the experimental data, and $t_{\text{TTP}} = 0.24\text{ s}$ for the simulations. In my investigation of the origin of this delay, I found that it came from the activation of the PDE and the binding of the second transducin. Therefore, this delay is probably an artefact from our modelling framework: in space-resolved simulations, the activation of the PDE and the binding of the second transducin would be faster.

The second type of comparison we can do between the experimental and simulated single photon responses is to investigate the statistical properties of the ensemble of responses. Typically, the coefficients of variation of the amplitude and the area are considered. They typically lie around 0.3 for single photon responses in mouse rods (Hamer et al., 2005). For the electrophysiologically recorded responses, we arrive at values of $CV_{\text{area}} = 0.37$ and $CV_{\text{amp}} = 0.23$. For the simulated single photon responses, we get values of $CV_{\text{area}} = 0.87$ and $CV_{\text{amp}} = 0.34$. Thus, the variability of the amplitudes is comparable, but the variability of the areas is too high for the simulated single photon responses.

Where does this discrepancy arise from? There are different possibilities. First of all, it is possible that the shut-off is less variable in reality than in the model. This could be due to a different effect of the phosphorylations of rhodopsin, for example. This will be discussed further when we consider the different knockout models.

Furthermore, it could be due to the lack of an additional feedback on the level of the effector which has been proposed in recent years and is discussed in section 3.4. This feedback mechanism could also be responsible for a decrease in variability of single photon responses.

Another reason for the deviation could be the subtraction of the dark noise's variance when calculating the CV of the electrophysiologically recorded single photon responses. The simulations do not have any dark noise, and it is thus not subtracted, which could lead to a higher CV of the simulations. I tried to add dark noise from the experimental data to the simulations, but the results were inconclusive, as the CV was not changed significantly (data not shown).

CHAPTER 5. DISCUSSION

There were a few issues when trying this: the experimentally recorded responses have a much higher sampling frequency than the simulated responses, so it was necessary to resample the noise to a lower sampling interval. Furthermore, it is not clear whether the noise during the responses is as high as the dark noise. For example, one noise source is the spontaneous activation of PDE molecules. Since many PDE molecules are activated by transducin during the single photon response, fewer of them are available to be activated spontaneously. Thus, the noise from this source is lower during the response than in the dark - this would lead to an actual reduction of the response variance when subtracting the dark variance. In the model, a way to investigate this further would be to include the noise sources in the model, by explicitly modelling the spontaneously activated PDE in a spontaneous activation reaction, whose rate does not depend on transducin. Further noise sources could be included, for example measurement noise, after an analysis of the noise from the recordings.

Finally, there is an effect of the categorization on the variability of the single photon responses. The simulated responses that we used for the comparison were all true single photon responses, where the initial condition was set to one activated rhodopsin molecule. The experimental single photon responses are categorized single photon responses, which were categorized according to their rising phases in the histogram method.

By simulating single photon responses with *random initial conditions* in section 4.6, we were able to compare the true single photon responses to the categorized single photon responses. We noticed that a few small single photon responses had been miscategorized as failures, and a few small multiple photon responses had been miscategorized as single photon responses, as shown in figure 4.28. The miscategorization led to an overall decrease in the coefficients of variation, demonstrating that the categorization procedure leads to an underestimation of the variability of the single photon response.

This is an interesting result: when we evaluate dim light recordings, it is impossible to know for certain which of the responses are true single photon responses. The only option to analyse single photon responses is by categorizing them first, but this already introduces a bias. By performing simulations with random initial conditions and doing the exact same procedure of categorization, we were able to conclude that this procedure leads to an underestimation of the variability and therefore needs to be taken with a grain of salt.

5.4.2 Knockout models

Next, we can use the model to simulate different knockout conditions. This allows us to check whether the model reproduces experimental results and is robust to changes in the kinetics. We did this comparison for the stochastic mouse model based on the Invergo 2014 model and for the new small model in sections 4.2.2 and 4.3.1.

When we compared the single photon responses in different knockout conditions, we saw that the models are able to faithfully reproduce the salient features of the rhodopsin kinase knockout, the completely substituted mutant of rhodopsin, and the GCAPs knockout (see figures 4.6 and 4.11). This shows that the models are robust in predicting the shut-off of the response when rhodopsin cannot be phosphorylated and when the guanylate cyclase is not regulated in a calcium-dependent manner.

However, for the arrestin knockout, there was a discrepancy: the response did not decrease as strongly as in the experiment after the maximum was reached. This could be due to different mechanism that are not correctly implemented in the model, or that are missing.

In the arrestin knockout, rhodopsin's activity is only shut off by rhodopsin being phosphorylated. It is possible that the decrease in rhodopsin's activity due to phosphorylations is underestimated in the models, and the role of arrestin is overestimated. Another possibility lies in a splice variant of arrestin that is also present in mouse rods, named p44. P44 is identical to arrestin in sequence, except for the last 35 amino acids. There is some evidence that it can also interact with rhodopsin, see (Pulvermüller et al., 1997). If p44 is also involved in the shut-off of the response, it would still be present and active in the experimental knockout. However, in the simulations, there is no p44 in the models and all the activity by any type of arrestin is deleted in the knockout model. This could explain the difference in shut-off we observed.

In summary, the model is quite robust when simulating different knockout conditions. We are able to reproduce most of the salient features of the knockout. The only issue where a further development of the model is necessary is the knockout of arrestin. Future perspectives could be a review of the effect of the phosphorylations on the activity of rhodopsin, or the addition of p44 into the model.

5.4.3 Precoupling

By changing the initial condition in the model, we were able to investigate the effect of precoupling in section 4.5. We compared simulations of single photon responses with two different initial conditions: one activated rhodopsin that is not precoupled to transducin, or one that is already precoupled to transducin. In deterministic simulations, the difference between the two initial conditions was very small, as shown in figure 4.20. The time to peak was slightly faster for the precoupled initial condition, but there was no large effect on the amplitude or time to peak.

This is surprising at a first glance, since the precoupled condition should give an advantage: after all, the first transducin is already bound to rhodopsin and can thus be activated faster than in the non-precoupled case. However, a large number of activated G-proteins is required to achieve a sufficiently high number of double-activated PDE molecules in this model. Thus, the effect of one transducin that is activated earlier is vanishingly small compared to the total of 458 activated transducin molecules. Our investigation further showed that the effect from the precoupling vanishes very quickly, after one simulation step of 1 ms.

To investigate this effect without the constraints of the modelling framework, space-resolved simulations would be beneficial. These might yield the same amount of double-activated PDE molecules without the need for such a large number of activated G-proteins, and thus one more activated G-protein could have a much larger effect.

In the stochastic simulations, we were however able to see that there is a difference in the variability of the single photon responses resulting from the different initial conditions: as shown in figure 4.24, the precoupling leads to slightly sharper distributions of the single photon response amplitudes and areas, which could have a beneficial effect for phototransduction. In order to reliably detect single photon response stimuli, when only few rods produce a signal, downstream neurons need to sort out responses from noise. This is probably done by amplitude thresholding (Field and Rieke, 2002), which is why reproducible amplitudes would be beneficial for the detection of single photon stimuli. Again, this effect could be much larger in a model where fewer transducin molecules are activated. Thus, for a further investigation of these promising initial results, space-resolved simulations would be necessary.

5.5 Conclusion

To conclude, the mass-action kinetics-based modelling performed here is a powerful tool to simulate light responses in many different conditions: light conditions ranging from single photon responses to bright flashes and light adaptation, as well as genetically altered conditions to mimic the effects in knockout animals or in disease conditions.

In deterministic simulations, I compared the model to novel experimentally recorded responses. I further investigated a relevant mechanism for light adaptation, namely the calcium feedback on the rhodopsin kinase and recoverin, which regulates the shut-off of rhodopsin. By investigating models with altered expression levels of the rhodopsin kinase and recoverin, I was able to demonstrate that there is no need in the model for an additional feedback on the shut-off of the effector to explain new results which had pointed in that direction. By modelling different generalized mutants of retinitis pigmentosa, I could show that calcium levels are impacted, especially when opsin is constitutively active. This could help explain the disease phenotype of cell death.

I updated the model to more accurately reflect new results concerning the precise nature and number of the effector and created stochastic versions of two pre-existing models and a new stochastic model. Using these models, I was able to investigate different effects in dim light responses. First of all, I investigated the role of the amount of phosphorylation sites of rhodopsin on the variability of single photon responses. Surprisingly, the results were quite different in the amphibian and the mouse model: in the amphibian model, all six phosphorylation sites were required for a low variability, while in the mouse model, only two to three were needed.

I also compared the simulated single photon responses in the new model to novel electrophysiologically recorded responses. The response shape was very similar, but the time to peak was a little slower in the simulated data. Furthermore, the coefficient of variability of the amplitude is comparable, but the coefficient of variability of the area is higher in the simulated data. I was however able to show that the categorization typically used for experimentally recorded dim light responses leads to an underestimation of the variability of the single photon response. For this, I performed stochastic simulations with randomized initial

CHAPTER 5. DISCUSSION

conditions and categorized the responses in the same way as the experimental data.

I also compared single photon responses in different knockout conditions in the stochastic mouse model and the new stochastic model to experimental results. For the knockout of the GCAPs and the rhodopsin kinase as well as the completely substituted mutant of rhodopsin, the results were consistent with the experiments. However, for the arrestin knockout, we observed a difference in the shut-off of the response.

Finally, I also investigated the effect of precoupling and was able to show that single photon responses arising from precoupled rhodopsin exhibit less variability, which could be beneficial for downstream signalling in the retina.

A | Models

In this appendix, I am listing the reaction equations, parameters, and initial conditions making up the modified models I have worked with in this thesis. For the original amphibian and mouse model, which these reaction equations and parameters are based on, see the supplementary information of (Dell’Orco et al., 2009) and (Invergo et al., 2014), respectively.

Please note that R refers to non-activated rhodopsin, while R_n stands for activated rhodopsin that has been phosphorylated n (up to six) times.

A.1 Stochastic amphibian model

This is the stochastic amphibian model created from the original deterministic amphibian model. The reaction equations and parameters listed here are based on the model presented in (Dell’Orco et al., 2009).

Table A.1: Reaction equations in the stochastic amphibian frontend model.

Nr.	Reaction equation	Rate
1	$R_n + RK \leftrightarrow R_n_RK_{pre}$	$v_f = k_{RK1,n} \cdot RK \cdot R_n$ $v_r = k_{RK2} \cdot R_n_RK_{pre}$
2	$R_n_RK_{pre} \rightarrow R_{n+1}_RK_{post}$	$v_f = k_{RK3,ATP} \cdot R_n_RK_{pre}$
3	$R_{n+1}_RK_{post} \rightarrow R_{n+1} + RK$	$v_f = k_{RK4} \cdot R_{n+1}_RK_{post}$
4	$Arr + R_n \leftrightarrow R_n_Arr$	$v_f = k_{A1,n} \cdot Arr \cdot R_n$ $v_r = k_{A2} \cdot R_n_Arr$
5	$R_n_Arr \rightarrow Ops + Arr$	$v_f = k_{A3} \cdot R_n_Arr$
6	$R_n \rightarrow Ops$	$v_f = k_{therm} \cdot R_n$
7	$Gt + R_n \leftrightarrow R_n_Gt$	$v_f = k_{G1,n} \cdot Gt \cdot R_n$ $v_r = k_{G2} \cdot R_n_Gt$
8	$R_n_Gt \leftrightarrow R_n_G$	$v_f = k_{G3} \cdot R_n_Gt$ $v_r = k_{G4,GDP} \cdot R_n_G$
9	$R_n_G \rightarrow R_n_G_{GTP}$	$v_f = k_{G5,GTP} \cdot R_n_G$
10	$R_n_G_{GTP} \rightarrow R_n + G_{GTP}$	$v_f = k_{G6} \cdot R_n_G_{GTP}$
11	$G_{GTP} \rightarrow G_{\alpha GTP} + G_{\beta\gamma}$	$v_f = k_{G7} \cdot G_{GTP}$
12	$PDE + G_{\alpha GTP} \leftrightarrow PDE_G_{\alpha GTP}$	$v_f = k_{P1} \cdot PDE \cdot G_{\alpha GTP}$ $v_r = k_{P1_{rev}} \cdot PDE_G_{\alpha GTP}$

APPENDIX A. MODELS

13	$\text{PDE_G}_{\alpha\text{GTP}} \rightarrow \text{PDE}^*_{\text{G}_{\alpha\text{GTP}}}$	$v_f = k_{\text{P2}} \cdot \text{PDE_G}_{\alpha\text{GTP}}$
14	$\text{PDE}^*_{\text{G}_{\alpha\text{GTP}}} + \text{G}_{\alpha\text{GTP}} \rightarrow \text{G}_{\alpha\text{GTP_PDE}^*_{\text{G}_{\alpha\text{GTP}}}}$	$v_f = k_{\text{P3}} \cdot \text{PDE}^*_{\text{G}_{\alpha\text{GTP}}} \cdot \text{G}_{\alpha\text{GTP}}$
15	$\text{G}_{\alpha\text{GTP_PDE}^*_{\text{G}_{\alpha\text{GTP}}}} \rightarrow \text{G}_{\alpha\text{GTP_PDE}^*_{\text{G}_{\alpha\text{GTP}}}}$	$v_f = k_{\text{P4}} \cdot \text{G}_{\alpha\text{GTP_PDE}^*_{\text{G}_{\alpha\text{GTP}}}}$
16	$\text{G}_{\alpha\text{GTP_PDE}^*_{\text{G}_{\alpha\text{GTP}}}} \rightarrow \text{RGS_G}_{\alpha\text{GTP_PDE}^*_{\text{G}_{\alpha\text{GTP}}}}$	$v_f = k_{\text{RGS1,RGS}_{\text{tot}}} \cdot \text{G}_{\alpha\text{GTP_PDE}^*_{\text{G}_{\alpha\text{GTP}}}}$
17	$\text{RGS_G}_{\alpha\text{GTP_PDE}^*_{\text{G}_{\alpha\text{GTP}}}} \rightarrow \text{PDE}^*_{\text{G}_{\alpha\text{GTP}}} + \text{G}_{\alpha\text{GDP}}$	$v_f = k_{\text{RGS2}} \cdot \text{RGS_G}_{\alpha\text{GTP_PDE}^*_{\text{G}_{\alpha\text{GTP}}}}$
18	$\text{PDE}^*_{\text{G}_{\alpha\text{GTP}}} \rightarrow \text{RGS_PDE}^*_{\text{G}_{\alpha\text{GTP}}}$	$v_f = k_{\text{RGS1,RGS}_{\text{tot}}} \cdot \text{PDE}^*_{\text{G}_{\alpha\text{GTP}}}$
19	$\text{RGS_PDE}^*_{\text{G}_{\alpha\text{GTP}}} \rightarrow \text{PDE} + \text{G}_{\alpha\text{GDP}}$	$v_f = k_{\text{RGS2}} \cdot \text{RGS_PDE}^*_{\text{G}_{\alpha\text{GTP}}}$
20	$\text{PDE}^*_{\text{G}_{\alpha\text{GTP}}} \rightarrow \text{PDE} + \text{G}_{\alpha\text{GDP}}$	$v_f = k_{\text{PDE}_{\text{shutoff}}} \cdot \text{PDE}^*_{\text{G}_{\alpha\text{GTP}}}$
21	$\text{G}_{\alpha\text{GTP_PDE}^*_{\text{G}_{\alpha\text{GTP}}}} \rightarrow \text{PDE}^*_{\text{G}_{\alpha\text{GTP}}} + \text{G}_{\alpha\text{GDP}}$	$v_f = k_{\text{PDE}_{\text{shutoff}}} \cdot \text{G}_{\alpha\text{GTP_PDE}^*_{\text{G}_{\alpha\text{GTP}}}}$
22	$\text{G}_{\alpha\text{GTP}} \rightarrow \text{G}_{\alpha\text{GDP}}$	$v_f = k_{\text{G}_{\text{shutoff}}} \cdot \text{G}_{\alpha\text{GTP}}$
23	$\text{G}_{\beta\gamma} + \text{G}_{\alpha\text{GDP}} \rightarrow \text{Gt}$	$v_f = k_{\text{G}_{\text{recyc}}} \cdot \text{G}_{\beta\gamma} \cdot \text{G}_{\alpha\text{GDP}}$

Table A.2: Reaction equations in the stochastic amphibian backend model.

Nr.	Reaction equation	Rate
24	$\text{Ca}_{\text{free}}^{2+} \leftrightarrow \text{Ca}_{\text{buff}}^{2+}$	$v_f = k_1 \cdot (e_{\text{T}} - \text{Ca}_{\text{buff}}^{2+}) \cdot \text{Ca}_{\text{free}}^{2+}$ $v_r = k_2 \cdot \text{Ca}_{\text{buff}}^{2+}$
25	$\text{Ca}_{\text{free}}^{2+} \rightarrow$	$v_f = \gamma_{\text{Ca}} \cdot (\text{Ca}_{\text{free}}^{2+} - \text{Ca}_0^{2+})$
26	$\rightarrow \text{Ca}_{\text{free}}^{2+}$	$v_f = \frac{10^6 \cdot f_{\text{Ca}} \cdot J_{\text{dark}}}{(2+f_{\text{Ca}}) \cdot F \cdot V_{\text{cyto}}} \cdot \left(\frac{\text{cGMP}}{\text{cGMP}_{\text{dark}}} \right)^{n_{\text{CG}}}$
27	$\rightarrow \text{cGMP}$	$v_f = \frac{\alpha_{\text{max}}}{1 + \left(\frac{\text{Ca}_{\text{free}}^{2+}}{K_{\text{C}}} \right)^m}$
28	$\text{cGMP} \rightarrow$	$v_f = (\beta_{\text{dark}} + \beta_{\text{sub}} \cdot E) \cdot \text{cGMP}$

Table A.3: Parameters in the stochastic amphibian frontend model.

Name	Value
$k_{\text{RK1},n}$	$\begin{cases} k_{\text{RK1},0} \cdot e^{-\omega \cdot n} & n < 6 \\ 0 & n = 6, \end{cases}$
$k_{\text{RK1},0}$	$7.643 \cdot 10^{-3}/\text{s}$
ω	0.70635
k_{RK2}	$250/\text{s}$
$k_{\text{RK3,ATP}}$	$400/\text{s}$
k_{RK4}	$20/\text{s}$
$k_{\text{A1},n}$	$n \cdot k_{\text{Arr}}$
k_{Arr}	$8.4558 \cdot 10^{-9}/\text{s}$
k_{A2}	$2.3 \cdot 10^{-3}/\text{s}$
k_{A3}	$3.5 \cdot 10^{-3}/\text{s}$

A.1. STOCHASTIC AMPHIBIAN MODEL

k_{therm}	0.0238/s
$k_{\text{G1},n}$	$k_{\text{G1},0} \cdot e^{-\omega \cdot n}$
$k_{\text{G1},0}$	$2.6456 \cdot 10^{-5}/\text{s}$
k_{G2}	2000/s
k_{G3}	2000/s
k_{G4}	600/s
$k_{\text{G5,GTP}}$	750/s
k_{G6}	2000/s
k_{G7}	200/s
k_{P1}	$4.9834 \cdot 10^{-4}/\text{s}$
$k_{\text{P1}_{\text{rev}}}$	0/s
k_{P2}	58.7798/s
k_{P3}	$1.4981 \cdot 10^{-5}/\text{s}$
k_{P4}	200/s
$k_{\text{RGS1,RGS}_{\text{tot}}}$	0.4710/s
k_{RGS2}	256.07/s
$k_{\text{PDE}_{\text{shutoff}}}$	0.033/s
$k_{\text{G}_{\text{shutoff}}}$	$8.25 \cdot 10^{-4}/\text{s}$
$k_{\text{G}_{\text{recyc}}}$	0.033/s

Table A.4: Parameters and variables in the stochastic amphibian backend model.

Name	Value
k_1	0.5/s μM
e_{T}	400 μM
k_2	2.5/s
γ_{Ca}	47.554/s
Ca_0^{2+}	0.01 μM
f_{Ca}	0.2
J_{dark}	29.7778 pA
F	96485.3415/cm
V_{cyto}	1 pL
$\text{cGMP}_{\text{dark}}$	4 μM
n_{CG}	3
α_{max}	$\beta_{\text{dark}} \cdot \text{cGMP}_{\text{dark}} \cdot \left(1 + \left(\frac{\text{Ca}_{\text{dark}}^{2+}}{K_{\text{C}}}\right)^m\right)$
β_{dark}	1.2/s
$\text{Ca}_{\text{dark}}^{2+}$	0.6 μM
K_{C}	0.17 μM
m	2.5
β_{sub}	$4.3 \cdot 10^{-4}/\text{s}$
E	$\text{PDE}^*_{-}\text{G}_{\alpha\text{GTP}} + \text{G}_{\alpha\text{GTP}}_{-}\text{PDE}^*_{-}\text{G}_{\alpha\text{GTP}} + 2 \cdot \text{G}_{\alpha\text{GTP}}_{-}^*\text{PDE}^*_{-}\text{G}_{\alpha\text{GTP}}$
J	$\frac{2}{2+f_{\text{Ca}}} \cdot \left(\frac{\text{cGMP}}{\text{cGMP}_{\text{dark}}}\right)^{n_{\text{CG}}} \cdot J_{\text{dark}} + \frac{f_{\text{Ca}}}{f_{\text{Ca}}+2} \cdot \frac{\text{Ca}_{\text{free}}^{2+}-\text{Ca}_0^{2+}}{\text{Ca}_{\text{dark}}^{2+}-\text{Ca}_0^{2+}} \cdot J_{\text{dark}}$
ΔJ	$J_{\text{dark}} - J$

APPENDIX A. MODELS

Table A.5: Nonzero initial conditions in the stochastic amphibian frontend model.

Species	Molecules
R0(0)	1
Gt(0)	$3.6 \cdot 10^8$
PDE(0)	$1.335 \cdot 10^7$
Arr(0)	$3.13 \cdot 10^7$
RK(0)	10838

Table A.6: Nonzero initial conditions in the stochastic amphibian backend model.

Species	Concentration
$\text{Ca}_{\text{free}}^{2+}(0)$	$0.6 \mu\text{M}$
$\text{Ca}_{\text{buff}}^{2+}(0)$	$42.857 \mu\text{M}$
cGMP(0)	$4 \mu\text{M}$

A.2 Stochastic mouse model

This is the stochastic mouse model created from the original deterministic mouse model. The reaction equations and parameters listed here are based on the model presented in (Invergo et al., 2014).

Table A.7: Reaction equations in the stochastic mouse frontend model.

Nr.	Reaction equation	Rate
1	$\text{R}_n + \text{RK} \leftrightarrow \text{R}_n\text{-RK}_{\text{pre}}$	$v_f = k_{\text{RK1},n} \cdot \text{RK} \cdot \text{R}_n$ $v_r = k_{\text{RK2}} \cdot \text{R}_n\text{-RK}_{\text{pre}}$
2	$\text{R}_n\text{-RK}_{\text{pre}} \rightarrow \text{R}_{n+1}\text{-RK}_{\text{post}}$	$v_f = k_{\text{RK3,ATP}} \cdot \text{R}_n\text{-RK}_{\text{pre}}$
3	$\text{R}_{n+1}\text{-RK}_{\text{post}} \rightarrow \text{R}_{n+1} + \text{RK}$	$v_f = k_{\text{RK4}} \cdot \text{R}_{n+1}\text{-RK}_{\text{post}}$
4	$\text{Arr} + \text{R}_n \leftrightarrow \text{R}_n\text{-Arr}$	$v_f = k_{\text{A1},n} \cdot \text{Arr} \cdot \text{R}_n$ $v_r = k_{\text{A2}} \cdot \text{R}_n\text{-Arr}$
5	$\text{R}_n\text{-Arr} \Rightarrow \text{Ops} + \text{Arr}$	$v_f = k_{\text{A3}} \cdot \text{R}_n\text{-Arr}$
6	$\text{R}_n \rightarrow \text{Ops}$	$v_f = k_{\text{therm}} \cdot \text{R}_n$
7	$\text{Gt} + \text{Ops} \leftrightarrow \text{Ops_Gt}$	$v_f = k_{\text{Ops}} \cdot \text{Gt} \cdot \text{Ops}$ $v_r = k_{\text{G2}} \cdot \text{Ops_Gt}$
8	$\text{Ops_Gt} \leftrightarrow \text{Ops_G}$	$v_f = k_{\text{G3}} \cdot \text{Ops_Gt}$ $v_r = k_{\text{G4,GDP}} \cdot \text{Ops_G}$
9	$\text{Ops_G} \rightarrow \text{Ops_G}_{\text{GTP}}$	$v_f = k_{\text{G5,GTP}} \cdot \text{Ops_G}$
10	$\text{Ops_G}_{\text{GTP}} \rightarrow \text{Ops} + \text{G}_{\text{GTP}}$	$v_f = k_{\text{G6}} \cdot \text{Ops_G}_{\text{GTP}}$
11	$\text{Gt} + \text{R}_n \leftrightarrow \text{R}_n\text{-Gt}$	$v_f = k_{\text{G1},n} \cdot \text{Gt} \cdot \text{R}_n$ $v_r = k_{\text{G2}} \cdot \text{R}_n\text{-Gt}$
12	$\text{R}_n\text{-Gt} \leftrightarrow \text{R}_n\text{-G}$	$v_f = k_{\text{G3}} \cdot \text{R}_n\text{-Gt}$ $v_r = k_{\text{G4,GDP}} \cdot \text{R}_n\text{-G}$

A.2. STOCHASTIC MOUSE MODEL

13	$R_n\text{-G} \rightarrow R_n\text{-G}_{GTP}$	$v_f = k_{G5,GTP} \cdot R_n\text{-G}$
14	$R_n\text{-G}_{GTP} \rightarrow R_n + G_{GTP}$	$v_f = k_{G6} \cdot R_n\text{-G}_{GTP}$
15	$G_{GTP} \rightarrow G_{\alpha GTP} + G_{\beta\gamma}$	$v_f = k_{G7} \cdot G_{GTP}$
16	$PDE + G_{\alpha GTP} \leftrightarrow PDE\text{-}G_{\alpha GTP}$	$v_f = k_{P1} \cdot PDE \cdot G_{\alpha GTP}$ $v_r = k_{P1,rev} \cdot PDE\text{-}G_{\alpha GTP}$
17	$PDE\text{-}G_{\alpha GTP} \rightarrow PDE^*\text{-}G_{\alpha GTP}$	$v_f = k_{P2} \cdot PDE\text{-}G_{\alpha GTP}$
18	$PDE^*\text{-}G_{\alpha GTP} + G_{\alpha GTP} \rightarrow G_{\alpha GTP}\text{-}PDE^*\text{-}G_{\alpha GTP}$	$v_f = k_{P3} \cdot PDE^*\text{-}G_{\alpha GTP} \cdot G_{\alpha GTP}$
19	$G_{\alpha GTP}\text{-}PDE^*\text{-}G_{\alpha GTP} \rightarrow G_{\alpha GTP}\text{-}^*PDE^*\text{-}G_{\alpha GTP}$	$v_f = k_{P4} \cdot G_{\alpha GTP}\text{-}PDE^*\text{-}G_{\alpha GTP}$
20	$G_{\alpha GTP}\text{-}^*PDE^*\text{-}G_{\alpha GTP} + RGS \rightarrow RGS\text{-}G_{\alpha GTP}\text{-}^*PDE^*\text{-}G_{\alpha GTP}$	$v_f = k_{RGS1} \cdot RGS \cdot G_{\alpha GTP}\text{-}^*PDE^*\text{-}G_{\alpha GTP}$
21	$RGS\text{-}G_{\alpha GTP}\text{-}^*PDE^*\text{-}G_{\alpha GTP} \rightarrow PDE^*\text{-}G_{\alpha GTP} + G_{\alpha GDP} + RGS$	$v_f = k_{RGS2} \cdot RGS\text{-}G_{\alpha GTP}\text{-}^*PDE^*\text{-}G_{\alpha GTP}$
22	$PDE^*\text{-}G_{\alpha GTP} + RGS \rightarrow RGS\text{-}PDE^*\text{-}G_{\alpha GTP}$	$v_f = k_{RGS1} \cdot RGS \cdot PDE^*\text{-}G_{\alpha GTP}$
23	$RGS\text{-}PDE^*\text{-}G_{\alpha GTP} \rightarrow PDE + G_{\alpha GDP} + RGS$	$v_f = k_{RGS2} \cdot RGS\text{-}PDE^*\text{-}G_{\alpha GTP}$
24	$PDE^*\text{-}G_{\alpha GTP} \rightarrow PDE + G_{\alpha GDP}$	$v_f = k_{PDE,shutoff} \cdot PDE^*\text{-}G_{\alpha GTP}$
25	$G_{\alpha GTP}\text{-}^*PDE^*\text{-}G_{\alpha GTP} \rightarrow PDE^*\text{-}G_{\alpha GTP} + G_{\alpha GDP}$	$v_f = k_{PDE,shutoff} \cdot G_{\alpha GTP}\text{-}^*PDE^*\text{-}G_{\alpha GTP}$
26	$G_{\alpha GTP} \rightarrow G_{\alpha GDP}$	$v_f = k_{G,shutoff} \cdot G_{\alpha GTP}$
27	$G_{\beta\gamma} + G_{\alpha GDP} \rightarrow G_t$	$v_f = k_{G,recyc} \cdot G_{\beta\gamma} \cdot G_{\alpha GDP}$
28	$Arr + Arr \leftrightarrow Arr_{di}$	$v_f = k_{A4} \cdot Arr \cdot Arr$ $v_r = k_{A5} \cdot Arr_{di}$
29	$Arr_{di} + Arr_{di} \leftrightarrow Arr_{tetra}$	$v_f = k_{A4} \cdot Arr_{di} \cdot Arr_{di}$ $v_r = k_{A5} \cdot Arr_{tetra}$

Table A.8: Reaction equations in the stochastic mouse backend model.

Nr.	Reaction equation	Rate
30	$Ca_{free}^{2+} \leftrightarrow Ca_{buff}^{2+}$	$v_f = k_1 \cdot (e_T - Ca_{buff}^{2+}) \cdot Ca_{free}^{2+}$ $v_r = k_2 \cdot Ca_{buff}^{2+}$
31	$Ca_{free}^{2+} \rightarrow$	$v_f = \gamma_{Ca} \cdot (Ca_{free}^{2+} - Ca_0^{2+})$
32	$\rightarrow Ca_{free}^{2+}$	$v_f = \frac{10^6 \cdot f_{Ca} \cdot J_{dark}}{(2+f_{Ca}) \cdot F \cdot V_{cyto}} \cdot \left(\frac{cGMP}{cGMP_{dark}} \right)^{n_{CG}}$
33	$\rightarrow cGMP$	$v_f = \frac{\alpha_{max}}{1 + \left(\frac{Ca_{free}^{2+}}{K_{C1}} \right)_1^m} + \frac{\alpha_{max}}{1 + \left(\frac{Ca_{free}^{2+}}{K_{C2}} \right)_2^m}$
34	$cGMP \rightarrow$	$v_f = (\beta_{dark} + \beta_{sub} \cdot E) \cdot cGMP$

APPENDIX A. MODELS

Table A.9: Parameters in the stochastic mouse frontend model.

Name	Value
$k_{\text{RK1},n}$	$\begin{cases} k_{\text{RK1},0} \cdot e^{-\omega \cdot n} & n < 6 \\ 0 & n = 6 \end{cases}$
$k_{\text{RK1},0}$	0.1724/s
ω	2.5
k_{RK2}	250/s
$k_{\text{RK3,ATP}}$	4000/s
k_{RK4}	250/s
$k_{\text{A1},n}$	$\begin{cases} k_{\text{Arr}} + (n - 1)m_{\text{Arr}} & n \leq 4 \\ k_{\text{Arr}} + 3m_{\text{Arr}} & n > 4 \end{cases}$
k_{Arr}	$9.9147 \cdot 10^{-6}$ /s
m_{Arr}	$9.5475 \cdot 10^{-6}$
k_{A2}	0.026/s
k_{A3}	1.1651/s
k_{therm}	0.0238/s
k_{Ops}	$6.1172 \cdot 10^{-13}$
k_{G2}	2200/s
k_{G3}	8500/s
k_{G4}	400/s
$k_{\text{G5,GTP}}$	3500/s
k_{G6}	8500/s
$k_{\text{G1},n}$	$k_{\text{G1},0} \cdot e^{-\omega_{\text{G}} \cdot n}$
$k_{\text{G1},0}$	$1 \cdot 10^{-3}$ /s
ω_{G}	0.6
k_{G7}	200/s
k_{P1}	0.05497/s
$k_{\text{P1}_{\text{rev}}}$	0/s
k_{P2}	940.7/s
k_{P3}	$1.4983 \cdot 10^{-9}$ /s
k_{P4}	21.088/s
k_{RGS1}	$4.8182 \cdot 10^{-5}$ /s
k_{RGS2}	98/s
$k_{\text{PDE}_{\text{shutoff}}}$	0.1/s
$k_{\text{G}_{\text{shutoff}}}$	0.05/s
$k_{\text{G}_{\text{recyc}}}$	2/s
k_{A4}	$2.9965 \cdot 10^{-7}$ /s
k_{A5}	0.424/s

A.2. STOCHASTIC MOUSE MODEL

Table A.10: Parameters and variables in the stochastic mouse backend model.

Name	Value
k_1	9.37059/s μ M
e_T	400 μ M
k_2	46.412/s
γ_{Ca}	981.356/s
Ca_0^{2+}	0.023 μ M
f_{Ca}	0.12
J_{dark}	14.87 pA
F	96485.3/cm
V_{cyto}	0.03916 pL
$cGMP_{dark}$	6.4944 μ M
n_{CG}	3.8
α_{max}	$\beta_{dark} \cdot cGMP_{dark} \cdot \left(1 + \left(\frac{Ca_{dark}^{2+}}{K_C}\right)^m\right)$
β_{dark}	3.19/s
Ca_{dark}^{2+}	0.25 μ M
K_{C1}	0.171 μ M
K_{C2}	0.059 μ M
m_1	3
m_2	1.5
β_{sub}	$2.1826 \cdot 10^{-3}$ /s
E	$PDE^* \cdot G_{\alpha GTP} + G_{\alpha GTP} \cdot PDE^* \cdot G_{\alpha GTP} + 2 \cdot G_{\alpha GTP} \cdot PDE^* \cdot G_{\alpha GTP}$
J	$\frac{2}{2+f_{Ca}} \cdot \left(\frac{cGMP}{cGMP_{dark}}\right)^{n_{CG}} \cdot J_{dark} + \frac{f_{Ca}}{f_{Ca}+2} \cdot \frac{Ca_{free}^{2+} - Ca_0^{2+}}{Ca_{dark}^{2+} - Ca_0^{2+}} \cdot J_{dark}$
ΔJ	$J_{dark} - J$

Table A.11: Nonzero initial conditions in the stochastic mouse frontend model.

Species	Molecules
R0(0)	1
Gt(0)	$8.1525 \cdot 10^6$
PDE(0)	$2 \cdot 10^6$
Arr(0)	$1.26076 \cdot 10^6$
Arr _{di} (0)	$1.1233 \cdot 10^6$
Arr _{tetra} (0)	$891810 \cdot 10^6$
RK(0)	580
RGS(0)	100000

Table A.12: Nonzero initial conditions in the stochastic mouse backend model.

Species	Concentration
$Ca_{free}^{2+}(0)$	0.25 μ M
$Ca_{buff}^{2+}(0)$	19.2199 μ M
cGMP(0)	6.4944 μ M

A.3 Updated deterministic mouse model

In the updated deterministic mouse model, most parameters were transferred directly from the mouse model from (Invergo et al., 2014), where a full list of parameters can be found in the supplementary information. Here is a list of the changed parameters for the updated model.

Table A.13: Parameter changes in the updated deterministic mouse model.

Parameter	Former Value	New Value
k_{G3}	8500/s	250/s
β_{sub}	$2.1826 \cdot 10^{-3}/\text{s}$	0.019/s

A.4 Small stochastic model

The basis of the small stochastic model is the mouse model from (Invergo et al., 2014). In the frontend, many reactions that were unnecessary for dim light responses were deleted or simplified, and some other reactions were modified. Furthermore, the frontend model was scaled down by reducing molecule numbers and scaling up the reaction rate constants accordingly. In the following tables, the new reactions, initial conditions, and parameters as well as their scaling are listed.

The backend was directly transferred from the stochastic mouse model, as given in tables A.8, A.10, and A.12, with one change: β_{sub} was changed to 0.01/s.

Please note that the number of available phosphorylation sites was reduced to three in this model, and therefore rhodopsin’s phosphorylation state n goes from zero to three.

A.4. SMALL STOCHASTIC MODEL

Table A.14: Reaction equations in the small stochastic frontend model.

Nr.	Reaction equation	Rate
1	$R_n + RK \leftrightarrow R_n\text{-}RK_{\text{pre}}$	$v_f = k_{RK1,n} \cdot RK \cdot R_n$ $v_r = k_{RK2} \cdot R_n\text{-}RK_{\text{pre}}$
2	$R_n\text{-}RK_{\text{pre}} \rightarrow R_{n+1}\text{-}RK_{\text{post}}$	$v_f = k_{RK3,ATP} \cdot R_n\text{-}RK_{\text{pre}}$
3	$R_{n+1}\text{-}RK_{\text{post}} \rightarrow R_{n+1} + RK$	$v_f = k_{RK4} \cdot R_{n+1}\text{-}RK_{\text{post}}$
4	$Arr + R_n \leftrightarrow R_n\text{-}Arr$	$v_f = k_{A1,n} \cdot Arr \cdot R_n$ $v_r = k_{A2} \cdot R_n\text{-}Arr$
5	$R_n\text{-}Arr \rightarrow Arr$	$v_f = k_{A3} \cdot R_n\text{-}Arr$
6	$R\text{-}Gt \rightarrow Gt + R$	$v_f = k_{Gpre2} \cdot R\text{-}Gt - k_{Gpre1} \cdot R \cdot Gt$
7	$Gt + R_n \leftrightarrow R_n\text{-}Gt$	$v_f = k_{G1,n} \cdot Gt \cdot R_n$ $v_r = k_{G2} \cdot R_n\text{-}Gt$
8	$R_n\text{-}Gt \leftrightarrow R_n\text{-}G$	$v_f = k_{G3} \cdot R_n\text{-}Gt$ $v_r = k_{G4,GDP} \cdot R_n\text{-}G$
9	$R_n\text{-}G \rightarrow R_n\text{-}G_{GTP}$	$v_f = k_{G5,GTP} \cdot R_n\text{-}G$
10	$R_n\text{-}G_{GTP} \rightarrow R_n + G_{GTP}$	$v_f = k_{G6} \cdot R_n\text{-}G_{GTP}$
11	$G_{GTP} \rightarrow G_{\alpha GTP} + G_{\beta\gamma}$	$v_f = k_{G7} \cdot G_{GTP}$
12	$PDE + G_{\alpha GTP} \leftrightarrow PDE\text{-}G_{\alpha GTP}$	$v_f = k_{P1} \cdot PDE \cdot G_{\alpha GTP}$ $v_r = k_{P1rev} \cdot PDE\text{-}G_{\alpha GTP}$
13	$PDE\text{-}G_{\alpha GTP} \rightarrow PDE^*\text{-}G_{\alpha GTP}$	$v_f = k_{P2} \cdot PDE\text{-}G_{\alpha GTP}$
14	$PDE^*\text{-}G_{\alpha GTP} + G_{\alpha GTP} \leftrightarrow G_{\alpha GTP}\text{-}PDE^*\text{-}G_{\alpha GTP}$	$v_f = k_{P3} \cdot PDE^*\text{-}G_{\alpha GTP} \cdot G_{\alpha GTP}$ $v_r = k_{P3rev} \cdot G_{\alpha GTP}\text{-}PDE^*\text{-}G_{\alpha GTP}$
15	$G_{\alpha GTP}\text{-}PDE^*\text{-}G_{\alpha GTP} \rightarrow G_{\alpha GTP}\text{-}^*PDE^*\text{-}G_{\alpha GTP}$	$v_f = k_{P4} \cdot G_{\alpha GTP}\text{-}PDE^*\text{-}G_{\alpha GTP}$
16	$G_{\alpha GTP}\text{-}^*PDE^*\text{-}G_{\alpha GTP} + RGS \rightarrow RGS\text{-}G_{\alpha GTP}\text{-}^*PDE^*\text{-}G_{\alpha GTP}$	$v_f = k_{RGS1} \cdot RGS \cdot G_{\alpha GTP}\text{-}^*PDE^*\text{-}G_{\alpha GTP}$
17	$RGS\text{-}G_{\alpha GTP}\text{-}^*PDE^*\text{-}G_{\alpha GTP} \rightarrow PDE^*\text{-}G_{\alpha GTP} + G_{\alpha GDP} + RGS$	$v_f = k_{RGS2} \cdot RGS\text{-}G_{\alpha GTP}\text{-}^*PDE^*\text{-}G_{\alpha GTP}$
18	$PDE^*\text{-}G_{\alpha GTP} + RGS \rightarrow RGS\text{-}PDE^*\text{-}G_{\alpha GTP}$	$v_f = k_{RGS1} \cdot RGS \cdot PDE^*\text{-}G_{\alpha GTP}$
19	$RGS\text{-}PDE^*\text{-}G_{\alpha GTP} \rightarrow PDE + G_{\alpha GDP} + RGS$	$v_f = k_{RGS2} \cdot RGS\text{-}PDE^*\text{-}G_{\alpha GTP}$
20	$PDE^*\text{-}G_{\alpha GTP} \rightarrow PDE + G_{\alpha GDP}$	$v_f = k_{PDEshutoff} \cdot PDE^*\text{-}G_{\alpha GTP}$
21	$G_{\alpha GTP}\text{-}^*PDE^*\text{-}G_{\alpha GTP} \rightarrow PDE^*\text{-}G_{\alpha GTP} + G_{\alpha GDP}$	$v_f = k_{PDEshutoff} \cdot G_{\alpha GTP}\text{-}^*PDE^*\text{-}G_{\alpha GTP}$
22	$G_{\alpha GTP} \rightarrow G_{\alpha GDP}$	$v_f = k_{Gshutoff} \cdot G_{\alpha GTP}$
23	$G_{\beta\gamma} + G_{\alpha GDP} \rightarrow Gt$	$v_f = k_{Grecyc} \cdot G_{\beta\gamma} \cdot G_{\alpha GDP}$

APPENDIX A. MODELS

In the following table, parameters that have been changed with respect to the mouse model (and not only scaled) are marked in red.

Table A.15: Parameters in the small stochastic frontend model.

Name	Unscaled value	Scaling	Scaled value
$k_{\text{RK1},n}$	$\begin{cases} k_{\text{RK1},0} \cdot e^{-\omega \cdot n} & n < 3 \\ 0 & n = 3 \end{cases}$	/	/
$k_{\text{RK1},0}$	0.03103	·580	18/s
ω	2.5	/	2.5
k_{RK2}	250/s	/	250/s
$k_{\text{RK3,ATP}}$	4000/s	/	4000/s
k_{RK4}	250/s	/	250/s
$k_{\text{A1},n}$	$k_{\text{Arr}} + (n - 1)m_{\text{Arr}}$	/	/
k_{Arr}	$9.9147 \cdot 10^{-6}/\text{s}$	·580	$5.751 \cdot 10^{-3}/\text{s}$
m_{Arr}	$9.5475 \cdot 10^{-6}$	·580	$5.538 \cdot 10^{-3}/\text{s}$
k_{A2}	0.026/s	/	0.026/s
k_{A3}	1.1651/s	/	1.1651/s
k_{Gpre1}	$1.6 \cdot 10^{-3}$	·580 ²	538.4/s
k_{Gpre2}	$6.93 \cdot 10^5$	·580	$4.019 \cdot 10^8/\text{s}$
$k_{\text{G1},n}$	$k_{\text{G1},0} \cdot e^{-\omega_{\text{G}} \cdot n}$	/	/
$k_{\text{G1},0}$	$2.5862 \cdot 10^{-3}$	·580	1.5/s
ω_{G}	0.6	/	0.6
k_{G2}	2600/s	/	2600/s
k_{G3}	85000/s	/	85000/s
k_{G4}	400/s	/	400/s
$k_{\text{G5,GTP}}$	12000/s	/	12000/s
k_{G6}	85000/s	/	85000/s
k_{G7}	200/s	/	200/s
k_{P1}	0.05497/s	·580	31.8826/s
$k_{\text{P1}_{\text{rev}}}$	100/s	/	100/s
k_{P2}	940.7/s	/	940.7/s
k_{P3}	0.05497/s	·580	31.8826/s
$k_{\text{P3}_{\text{rev}}}$	3000/s	/	3000/s
k_{P4}	940.7/s	/	940.7/s
k_{RGS1}	$1.0344 \cdot 10^{-4}/\text{s}$	·580	0.06/s
k_{RGS2}	140/s	/	140/s
$k_{\text{PDE}_{\text{shutoff}}}$	0.1/s	/	0.1/s
$k_{\text{G}_{\text{shutoff}}}$	0.05/s	/	0.05/s
$k_{\text{G}_{\text{recyc}}}$	2/s	/	2/s

A.4. SMALL STOCHASTIC MODEL

All initial conditions have been reduced by a scaling factor of $1/580$, as given below, except for the activated rhodopsin ($R0(0)$ or the precoupled $R0_Gt(0)$).

Table A.16: Nonzero initial conditions in the small stochastic frontend model.

Species	Molecules
$R0(0)$	0 or 1
$R0_Gt(0)$	0 or 1
$R(0)$	169228
$Gt(0)$	14056
$R_Gt(0)$	3185
$PDE(0)$	3448
$Arr(0)$	2174
$RK(0)$	1
$RGS(0)$	172

Bibliography

- P. Ala-Laurila and F. Rieke. Coincidence Detection of Single-Photon Responses in the Inner Retina at the Sensitivity Limit of Vision. *Curr. Biol.*, **24**:2888–2898, 2014.
- J.B. Ames, R. Ishima, T. Tanaka, J.I. Gordon, L. Stryer, and M. Ikura. Molecular mechanics of calcium–myristoyl switches. *Nature*, **389**:198–202, 1997.
- A. Andrés, P. Garriga, and J. Manyosa. Altered functionality in rhodopsin point mutants associated with retinitis pigmentosa. *Biochem. Biophys. Res. Commun.*, **303**:294–301, 2003.
- D. Athanasiou, M. Aguila, J. Bellingham, W. Li, C. McCulley, P.J. Reeves, and M.E. Cheetham. The molecular and cellular basis of rhodopsin retinitis pigmentosa reveals potential strategies for therapy. *Prog. Retin. Eye Res.*, **62**:1–23, 2018.
- D.A. Baylor, T.D. Lamb, and K.W. Yau. Responses of retinal rods to single photons. *J. Physiol.*, **288**:613–634, 1979.
- P. Bisegna, G. Caruso, D. Andreucci, L. Shen, V.V. Gurevich, H.E. Hamm, and E. DiBenedetto. Diffusion of the Second Messengers in the Cytoplasm Acts as a Variability Suppressor of the Single Photon Response in Vertebrate Phototransduction. *Biophys. J.*, **94**:3363–3383, 2008.
- E. Budzynski, A.K. Gross, S.D. McAlear, N.S. Peachey, M. Shukla, F. He, M. Edwards, J. Won, W.L. Hicks, T.G. Wensel, J.K. Naggert, and P.M. Nishina. Mutations of the Opsin Gene (Y102H and I307N) Lead to Light-induced Degeneration of Photoreceptors and Constitutive Activation of Phototransduction in Mice. *J. Biol. Chem.*, **285**(19):14521–14533, 2010.
- M.E. Burns, A. Mendez, J. Chen, and D.A. Baylor. Dynamics of Cyclic GMP Synthesis in Retinal Rods. *Neuron*, **36**:81–91, 2002.
- L. Cangiano and D. Dell’Orco. Detecting single photons: A supramolecular matter? *Febs Lett.*, **587**:1–4, 2012.
- L. Cangiano, C. Gargina, L. Della Santina, G.C. Demontis, and L. Cervetto. High-Pass Filtering of Input Signals by the Ih Current in a Non-Spiking Neuron, the Retinal Rod Bipolar Cell. *PLoS ONE*, **2**:e1327, 2007.

BIBLIOGRAPHY

- L. Cangiano, S. Asteriti, L. Cervetto, and C. Gargina. The photovoltage of rods and cones in the dark-adapted mouse retina. *J. Physiol.*, **590**:3841–3855, 2012.
- C. Cepko. Intrinsically different retinal progenitor cells produce specific types of progeny. *Nat. Rev. Neurosci.*, **15**:615–627, 2014.
- M. Chabre and M. le Maire. Monomeric G-Protein-Coupled Receptor as a Functional Unit. *Biochemistry*, **44**(27):9395–9403, 2005.
- M. Chabre, R. Cone, and H. Saibil. Is rhodopsin dimeric in native retinal rods? *Nature*, **426**:30–31, 2003.
- C.-K. Chen, J. Inglese, R.J. Lefkowitz, and J.B. Hurley. Ca²⁺-dependent Interaction of Recoverin with Rhodopsin Kinase. *J. Biol. Chem.*, **270**(30):18060–18066, 1995.
- C.-K. Chen, M.E. Burns, M. Spencer, G.A. Niemi, J. Chen, J.B. Hurley, D.A. Baylor, and M.I. Simon. Abnormal photoresponses and light-induced apoptosis in rods lacking rhodopsin kinase. *Proc. Natl. Acad. Sci. USA*, **96**:3718–3722, 1999.
- C.-K. Chen, M.L. Woodruff, F.S. Chen, Y. Chen, M.C. Cilluffo, D. Tranchina, and G.L. Fain. Modulation of Mouse Rod Response Decay by Rhodopsin Kinase and Recoverin. *J. Neurosci.*, **32**:15998–16006, 2012.
- C.-K. Chen, M.L. Woodruff, and G.L. Fain. Rhodopsin kinase and recoverin modulate phosphodiesterase during mouse photoreceptor light adaptation. *J. Gen. Physiol.*, **145**(3):213–224, 2015.
- J. Chen and A.P. Sampath. Structure and Function of Rod and Cone Photoreceptors. In Stephen J. Ryan, Srinivas R. Sadda, David R. Hinton, Andrew P. Schachar, C.P. Wilkinson, and Peter Wiedemann, editors, *Retina (Fifth Edition)*, volume 1, chapter 14, pages 342–359. Elsevier Inc., Amsterdam, 2013.
- D. Dell’Orco. A physiological role for the supramolecular organization of rhodopsin and transducin in rod photoreceptors. *Febs Lett.*, **587**:2060–2066, 2013.
- D. Dell’Orco and G. Dal Cortivo. Normal GCAPs partly compensate for altered cGMP signaling in retinal dystrophies associated with mutations in GUCA1A. *Sci. Rep.*, **9**:20105, 2019.
- D. Dell’Orco and K.-W. Koch. Systems biochemistry approaches to vertebrate phototransduction: towards a molecular understanding of disease. *Biochem. Soc. Trans.*, **38**:1275–1280, 2010.
- D. Dell’Orco and K.-W. Koch. A dynamic scaffolding mechanism for rhodopsin and transducin interaction in vertebrate vision. *Biochem. J.*, **440**:263–271, 2011.

- D. Dell’Orco and H. Schmidt. Mesoscopic Monte Carlo Simulations of Stochastic Encounters Between Photoactivated Rhodopsin and Transducin in Disc Membranes. *J. Phys. Chem. B.*, **112**(14):4419–4426, 2008.
- D. Dell’Orco, H. Schmidt, S. Mariani, and F. Fanelli. Network-level analysis of light adaptation in rod cells under normal and altered conditions. *Mol. BioSyst.*, **5**:1232–1246, 2009.
- Daniele Dell’Orco. Rhodopsin Transient Complexes Investigated by Systems Biology Approaches. In B. Jastrzebska, editor, *Rhodopsin: Methods and Protocols*, volume 1271, chapter 17, pages 251–263. Springer Science+Business Media, New York, 2015.
- X. Deupi, P. Edwards, A. Singhal, B. Nickle, D. Oprian, G. Schertler, and J. Standfuss. Stabilized G protein binding site in the structure of constitutively active metarhodopsin-II. *Proc. Natl. Acad. Sci. USA*, **109**(1):119–124, 2012.
- T. Doan, A. Mendez, P.B. Detwiler, J. Chen, and F. Rieke. Multiple Phosphorylation Sites Confer Reproducibility of the Rod’s Single-Photon Responses. *Science*, **313**:530–533, 2006.
- Dreamstime. [Dreamstime.com](https://www.dreamstime.com/), ©Designua, Identification 27214192, 2000-2020.
- S. Felber, H.P. Breuer, F. Petruccione, J. Honerkamp, and K.P. Hofmann. Stochastic simulation of the transducin GTPase cycle. *Biophys. J.*, **71**(6):3051 – 3063, 1996.
- G.D. Field and F. Rieke. Nonlinear signal transfer from mouse rods to bipolar cells and implications for visual sensitivity. *Neuron*, **34**:773–785, 2002.
- D. Fotiadis, Y. Liang, S. Filipek, D.A. Saperstein, A. Engel, and K. Palczewski. Rhodopsin dimers in native disc membranes. *Nature*, **421**:127–128, 2003.
- D. Fotiadis, Y. Liang, S. Filipek, D.A. Saperstein, A. Engel, and K. Palczewski. The G protein-coupled receptor rhodopsin in the native membrane. *Febs Lett.*, **564**:281–288, 2004.
- O. Fritze, S. Filipek, V. Kuksa, K. Palczewski, K.P. Hofmann, and O.P. Ernst. Role of the conserved NPxxY(x)_{5,6}F motif in the rhodopsin ground state and during activation. *Proc. Natl. Acad. Sci. USA*, **100**(5):2290–2295, 2003.
- P. Garriga, X. Liu, and H.G. Khorana. Structure and function in rhodopsin: Correct folding and misfolding in point mutants at and in proximity to the site of the retinitis pigmentosa mutation Leu-125 → Arg in the transmembrane helix C. *Biochemistry*, **93**:4560–4564, 1996.

BIBLIOGRAPHY

- S.K. Gibson, J.H. Parkes, and P.A. Liebman. Phosphorylation Modulates the Affinity of Light-Activated Rhodopsin for G Protein and Arrestin. *Biochemistry*, **39**:5738–5749, 2000.
- D.T. Gillespie. Exact stochastic simulation of coupled chemical reactions. *J. Phys. Chem.*, **81**:2340–2361, 1977.
- A.K. Gross, V.R. Rao, and D.D. Oprian. Characterization of Rhodopsin Congenital Night Blindness Mutant T94I. *Biochemistry*, **42**:2009–2015, 2003.
- M. Gunkel, J. Schöneberg, W. Alkhalidi, S. Irsen, F. Noé, U.B. Kaupp, and A. Al-Amoudi. Higher-Order Architecture of Rhodopsin in Intact Photoreceptors and Its Implication for Phototransduction Kinetics. *Structure*, **23**:628–638, 2015.
- R.D. Hamer, S.C. Nicholas, D. Tranchina, P.A. Liebman, and T.D. Lamb. Multiple steps of phosphorylation of activated rhodopsin can account for the reproducibility of vertebrate rod single-photon responses. *J. Gen. Physiol.*, **122**(4):419–444, 2003.
- R.D. Hamer, S.C. Nicholas, D. Tranchina, T.D. Lamb, and J.L.P. Jarvinen. Toward a unified model of vertebrate rod phototransduction. *Visual Neurosci.*, **22**:417–436, 2005.
- F. Hayashi, N. Saito, Y. Tanimoto, K. Okada, K. Morigaki, K. Seno, and S. Maekawa. Raftophilic rhodopsin-clusters offer stochastic platforms for G protein signalling in retinal discs. *Commun. Biol.*, **2**(209), 2019.
- S. Hecht, S. Shlaer, and M.H. Pirenne. Energy, quanta, and vision. *J. Gen. Physiol.*, **25**:819–840, 1942.
- M. Heck, K.P. Hofmann, T.W. Kraft, and T.D. Lamb. Phototransduction gain at the G-protein, transducin, and effector protein, phosphodiesterase-6, stages in retinal rods. *Proc. Natl. Acad. Sci. USA*, **116**(18):8653–8654, 2019.
- A.V. Hill. The possible effects of the aggregation of the molecules of hæmoglobin on its dissociation curves. *J. Physiol.*, **40**:4–7, 1910.
- B. Ingalls. *Mathematical Modelling in Systems Biology: An Introduction*. The MIT Press, 2012.
- B.M. Invergo, D. Dell’Orco, L. Montanucci, K.-W. Koch, and J. Bertranpetit. A comprehensive model of the phototransduction cascade in mouse rod cells. *Mol. Biosyst.*, **10**:1481–1489, 2014.
- IQMtoolbox Website. <https://iqmtools.intiquan.com>, 2020.

- M. Kahlert and K.P. Hofmann. Reaction rate and collisional efficiency of the rhodopsin-transducin system in intact retinal rods. *Biophys. J.*, **59**:375–386, 1991.
- Y. Kamiyama, S.M. Wu, and S. Usui. Simulation analysis of bandpass filtering properties of a rod photoreceptor network. *Vision Res.*, **49**:970–978, 2009.
- V.A. Klenchin, P.D. Calvert, and M.D. Bownds. Inhibition of Rhodopsin Kinase by Recoverin: Further evidence for a negative feedback system in phototransduction. *J. Biol. Chem.*, **270**(27):16147–16152, 1995.
- K.-W. Koch and D. Dell’Orco. Protein and Signaling Networks in Vertebrate Photoreceptor Cells. *Front. Mol. Neurosci.*, **8**(67), 2015.
- K.-W. Koch and L. Stryer. Highly cooperative feedback control of retinal rod guanylate cyclase by calcium ions. *Nature*, **334**:64–66, 1988.
- M.W. Kutta. Beitrag zur näherungsweise Integration totaler Differentialgleichungen. *Z. Math. Phys.*, **46**:435–453, 1901.
- T.D. Lamb. Stochastic Simulation of Activation in the G-Protein Cascade of Phototransduction. *Biophys. J.*, **67**:1439–1454, 1994.
- T.D. Lamb and T.W. Kraft. A quantitative account of mammalian rod phototransduction with PDE6 dimeric activation: responses to bright flashes. *Open Biol.*, **10**:190241, 2020.
- T.D. Lamb and E.N. Pugh Jr. A quantitative account of the activation steps involved in phototransduction in amphibian photoreceptors. *J. Physiol.*, **449**:719–758, 1992.
- T.D. Lamb, M. Heck, and T.W. Kraft. Implications of dimeric activation of PDE6 for rod phototransduction. *Open Biol.*, **8**:180076, 2018.
- Y. Liang, D. Fotiadis, S. Filipek, D.A. Saperstein, K. Palczewski, and A. Engel. Organization of the G Protein-coupled Receptors Rhodopsin and Opsin in Native Membranes. *J. Biol. Chem.*, **278**(24):21655–21662, 2003.
- A. Mendez, M.E. Burns, A. Roca, J. Lem, L.-W. Wu, M.L. Simon, D.A. Baylor, and J. Chen. Rapid and Reproducible Deactivation of Rhodopsin Requires Multiple Phosphorylation Sites. *Neuron*, **28**:153–164, 2000.
- A. Morshedien, M.L. Woodruff, and G.L. Fain. Role of recoverin in rod photoreceptor light adaptation. *J. Physiol.*, **596**(8):1513–1526, 2018.
- E.V. Olshevskaya, R.E. Hughes, J.B. Hurley, and A.M. Dizhoor. Calcium binding, but not a calcium-myristoyl switch, controls the ability of guanylyl cyclase-activating protein GCAP-2 to regulate photoreceptor guanylyl cyclase. *J. Biol. Chem.*, **272**:14327–14333, 1997.

BIBLIOGRAPHY

- K. Palczewski, I. Subbaraya, W.A. Gorczyca, B.S. Helekar, C.C. Ruiz, H. Ohguro, J. Huang, X. Zhao, J.W. Crabb, R.S. Johnson, K.A. Walsh, M.P. Gray-Keller, P.B. Detwiler, and W. Baehr. Molecular cloning and characterization of retinal photoreceptor guanylyl cyclase-activating protein. *Neuron*, **13**:395–404, 1994.
- W.H. Press, S.A. Teukolsky, W.T. Vetterling, and Flannery B.P. *NUMERICAL RECIPES. The Art of Scientific Computing*. Cambridge University Press, 3 edition, 2007.
- E.N. Pugh Jr and T.D. Lamb. Phototransduction in Vertebrate Rods and Cones: Molecular Mechanisms of Amplification, Recovery and Light Adaptation. In D.G. Stavenga, W.J. de Grip, and E.N. Pugh Jr, editors, *Handbook of Biological Physics Volume 3, Molecular Mechanisms of Visual Transduction*, chapter 5, pages 183–255. Elsevier Science, Amsterdam, 2000.
- A. Pulvermüller, D. Maretzki, M. Rudnicka-Nawrot, W.C. Smith, K. Palczewski, and K.P. Hofmann. Functional differences in the interaction of arrestin and its splice variant, p44, with rhodopsin. *Biochemistry*, **36**:9253–9260, 1997.
- B.M. Qureshi, E. Behrmann, J. Schöneberg, J. Loerke, J. Bürger, T. Mielke, J. Giesebrecht, F. Noé, T.D. Lamb, K.P. Hofmann, C.M.T. Spahn, and M. Heck. It takes two transducins to activate the cGMP-phosphodiesterase 6 in retinal rods. *Open Biol.*, **8**:180075, 2018.
- J. Reingruber and D. Holcman. The Dynamics of Phosphodiesterase Activation in Rods and Cones. *Biophys. J.*, **94**:1954–1970, 2008.
- J. Reingruber, J. Pahlberg, M.L. Woodruff, A.P. Sampath, G.L. Fain, and D. Holcman. Detection of single photons by toad and mouse rods. *Proc. Natl. Acad. Sci. USA*, **110**(48):319378–19383, 2013.
- F. Rieke and D.A. Baylor. Origin of Reproducibility in the Responses of Retinal Rods to Single Photons. *Biophys. J.*, **75**:1836–1857, 1998.
- C.D.T. Runge. Über die numerische Auflösung von Differentialgleichungen. *Math. Ann.*, **46**:167–178, 1895.
- B. Sakitt. Counting every quantum. *J. Physiol.*, **223**:131–150, 1972.
- H. Schmidt and M. Jirstrand. Systems Biology Toolbox for MATLAB: a computational platform for research in systems biology. *Bioinformatics*, **22**(4):514–515, 2005.
- J. Schöneberg, M. Heck, K.P. Hofmann, and F. Noé. Explicit Spatiotemporal Simulation of Receptor-G Protein Coupling in Rod Cell Disk Membranes. *Biophys. J.*, **107**:1042–1053, 2014.

- I.I. Senin, L. Bosch, E. Ramon, E.Y. Zernii, J. Manyosa, P.P. Philippov, and P. Garriga. Ca^{2+} /recoverin dependent regulation of phosphorylation of the rhodopsin mutant R135L associated with retinitis pigmentosa. *Biochem. Biophys. Res. Commun.*, **349**: 345–352, 2006.
- A. Tikidji-Hamburyan, K. Reinhard, R. Storchi, J. Dietter, H. Seitter, K.E. Davis, S. Idrees, M. Mutter, L. Walmsley, R.A. Bedford, M. Ueffing, P. Ala-Laurila, T.M. Brown, R.J. Lucas, and T.A. Münch. Rods progressively escape saturation to drive visual responses in daylight conditions. *Nat. Commun.*, **8**:1813, 2017.
- D. Toledo, E. Ramon, M. Aguilà, A. Cordoní, J.J. Pérez, H.F. Mendes, M.E. Cheetham, and P. Garriga. Molecular Mechanisms of Disease for Mutations at Gly-90 in Rhodopsin. *J. Biol. Chem.*, **286**(46):39993–40001, 2011.
- S.H. Tsang, M.L. Woodruff, K.M. Janisch, M.C. Cilluffo, D.B. Farber, and G.L. Fain. Removal of phosphorylation sites of γ subunit of phosphodiesterase6 alters rod light response. *J. Physiol.*, **579**:303–312, 2007.
- H. Wässle. Parallel processing in the mammalian retina. *Nat. Rev. Neurosci.*, **5**:747–757, 2004.
- M.L. Woodruff, K.M. Janisch, I.V. Peshenko, A.M. Dizhoor, S.H. Tsang, and G.L. Fain. Modulation of Phosphodiesterase6 Turnoff during Background Illumination in Mouse Rod Photoreceptors. *J. Neurosci.*, **28**:2064–2074, 2008.
- J. Xu, R.L. Dodd, C.L. Makino, M.L. Simon, D.A. Baylor, and J. Chen. Prolonged photoresponses in transgenic mouse rods lacking arrestin. *Nature*, **389**:505–509, 1997.
- K.-W. Yau, W.W.S. Yue, and D. Silverman. Reply to Heck et al: Signal amplification at the rhodopsin-to-transducin-phosphodiesterase step in rod phototransduction. *Proc. Natl. Acad. Sci. USA*, **116**(18):8655–8656, 2019.
- W.W.S. Yue, D. Silverman, X. Ren, R. Frederiksen, K. Sakai, T. Yamashita, Y. Shichida, M.C. Cornwall, J. Chen, and K.-W. Yau. Elementary response triggered by transducin in retinal rods. *Proc. Natl. Acad. Sci. USA*, **116**:5144–5153, 2019.

BIBLIOGRAPHY

Eigenständigkeitserklärung

Hiermit erkläre ich, dass ich die vorliegende Dissertation selbst verfasst und nur die angegebenen Quellen und Hilfsmittel verwendet habe. Außerdem versichere ich, dass ich die allgemeinen Prinzipien wissenschaftlicher Arbeit und Veröffentlichung, wie sie in den Leitlinien guter wissenschaftlicher Praxis der Carl von Ossietzky Universität Oldenburg festgelegt sind, befolgt habe.

Datum

Charlotte Johanna Beelen